MODELLING CONSIDERATIONS FOR A TRANSONIC FAN

by

Yu Ning Dai

A Thesis

Submitted to the Faculty of Purdue University

In Partial Fulfillment of the Requirements for the degree of

Master of Science in Aeronautics and Astronautics

School of Aeronautics and Astronautics

West Lafayette, Indiana

May 2022

THE PURDUE UNIVERSITY GRADUATE SCHOOL

STATEMENT OF COMMITTEE APPROVAL

Dr. Nicole Key, Chair

School of Mechanical Engineering

Dr. Guillermo Paniagua

School of Mechanical Engineering

Dr. Jonathan Poggie

School of Aeronautics and Astronautics

Approved by:

Dr. Gregory Blaisdell

“To ask the right question is harder than to answer it.”

- *Georg Cantor*

ACKNOWLEDGMENTS

I would like to first thank my advisor, Professor Nicole Key, for giving me this great opportunity and for her continuous guidance and encouragement. I am thankful for her insight and support in my research endeavors, and for helping me learn and improve in my research these past few years. I am grateful to my advisory committee members, Professor Guillermo Paniagua and Professor Jonathan Poggie, for their patience and feedback on my work.

I would like to thank the Office of Naval Research for their financial support of this project. I am also very thankful for technical support from Honeywell Aerospace on this project – to Darrell James, Nick Nolcheff, Bruce Reynolds, and Mahmoud Mansour for their valuable advice.

I am fortunate to have the best teammates and friends, Andrew and Will, who have been the most reliable and positive through all our endeavors. I would like to thank all of my lab members and friends, for making this a pleasant and welcoming environment to work, and for their great sense of humor. Additionally, I am grateful to Will, Doug, and Matt for many helpful discussions on CFD, and to Andy Schmid for his engineering support on our project.

Thank you to my friends back at home, especially Thy and Nancy, for your support and many distractions that brighten my day.

Finally, thank you to my parents, grandparents, and little sister for supporting me and encouraging me to pursue my goals. I really look forward to seeing you again.

TABLE OF CONTENTS

LIST OF TABLES

LIST OF FIGURES

NOMENCLATURE

Symbol	Definition
A	Geometric area
A_r	Roughness coefficient
B	Blockage
BPR	Bypass ratio
BSL	Menter Baseline turbulence model
CCF	Cross-correlation coefficient
CFD	Computational fluid dynamics
EARSM	Explicit Algebraic Reynolds Stress Model
f_A	Fuzzy convergence of amplitude
f_c	Overall level of fuzzy convergence
f_M	Fuzzy convergence of mean level
f_P	Fuzzy convergence of PSD
f_s	Fuzzy convergence of CCL at 0 lag
f_ϕ	Fuzzy convergence of phase
GCI	Grid convergence index
h	Representative grid size
H_n	Normalized helicity
K_s	Sand-grain roughness
N	Total number of elements in mesh
NSVI	Normal shock-vortex interaction
OSVI	Oblique shock-vortex interaction
P	Pressure (static unless indicated otherwise)
PSD	Power spectral density
r	Radial direction
r_f	Grid refinement factor
RANS	Reynolds-Averaged Navier-Stokes
RSM	Reynolds Stress Model

Symbol	**Definition**
SST	Shear Stress Transport turbulence model
T	Temperature (static unless indicated otherwise)
TLF	Tip leakage flow
TLV	Tip leakage vortex
TPR	Total pressure ratio
TTR	Total temperature ratio
u_τ	Friction velocity
U	Wheel speed
V	Absolute velocity
w	Vector of relative flow velocity
W	Work done per unit mass flow
y	Wall distance
y_+	Non-dimensional wall distance
β	Relative flow angle
δ^*	Integral of velocity-density deficit
ξ	Vector of absolute vorticity
η	Adiabatic efficiency
θ	Circumferential direction
υ	Local kinematic viscosity

Subscripts	**Definition**
θ	Circumferential component
x	Axial component
0	Stagnation property
1	Rotor inlet
2	Rotor exit
$bypass$	Flow through bypass
$coarse$	Coarse mesh
$core$	Flow through core
$corr$	Corrected
$fine$	Fine mesh
$mean$	Mean over period
rms	Root mean square

ABSTRACT

The objective of this work is to provide a computational baseline for modelling the flow physics in the tip region of a transonic fan. A transonic fan was donated by Honeywell Aerospace to the Purdue University High-Speed Compressor Research Laboratory for the purposes of studying casing treatments and inlet distortion under the Office of Naval Research Power and Propulsion Program. The purpose of casing treatment is to extend the stall margin of the fan without being detrimental to fan efficiency. Hence, before an effective casing treatment can be designed, understanding the instabilities that lead to stall or surge and understanding the flow field near the rotor tip at different operating conditions is necessary.

The behavior of the flow field was studied at design speed using steady simulations for near stall, peak efficiency, and choke operating conditions. The details of the passage shock, tip leakage vortex, and the shock-vortex interaction were investigated. The passage shock moves forward in the rotor passage as the loading increases, until eventually becoming unstarted near stall. The tip leakage vortex convects from the rotor tip leading edge to the pressure side of the adjacent blade, and its trajectory becomes parallel to the rotor inlet plane as the loading increases. The shock-vortex interaction does not cause the tip leakage vortex to breakdown, although distortion of the shock front and diffusion of the tip leakage vortex is significant near stall.

To validate this computational model, steady simulations were used to conduct a grid convergence study. A single passage mesh of 8 million elements is sufficient to capture the flow qualitatively, but a mesh of at least 22 million elements is recommended to lower discretization error if quantitative details are important. A brief comparison of turbulence models is made, and the SST model was found to predict stronger radial flows than the BSL-EARSM and BSL-RSM models. However, the SST model still captures the flow features qualitatively, and the more complex models would be too costly for iterative design simulations.

The importance of unsteady effects was also considered for a point near peak efficiency. Near peak efficiency, the effect of shock oscillations near the rotor shroud are small. Compared to steady simulations, the unsteady simulation predicts a slightly stronger horseshoe vortex at the hub and a passage shock closer to the rotor leading edge. The tip leakage vortex trajectory appears to be the same between the steady and unsteady simulations.

The modelling decisions made in this research are currently only based on comparison between simulations. This model will be calibrated with experimental data in the future to provide a more accurate view of the flow physics inside this transonic fan.

1. INTRODUCTION

1.1 Motivation

Advancements in gas turbine engines to reduce size and weight has led to increased use of transonic fans and compressors. Transonic fans can ingest larger airflows per unit of engine frontal area and have increased pressure ratios compared to the subsonic fan. The increase in rotational speed allows the compressor to achieve higher loading, thus reducing the number of stages needed to reach a desired pressure ratio. However, high-speed compressor operation can lead to tradeoffs in efficiency and operation range.

The performance of a compressor can be assessed by its ability to do work on a fluid efficiently, and its stable operating range. For axial compressors and fans, the Euler turbomachinery equation can be written to omit the radius change:

$$W = U(V_{\theta 2} - V_{\theta 1}) \tag{1.1}$$

The work done per unit mass flow W can be increased through the wheel speed U and amount of flow turning across the rotor $(V_{\theta 2} - V_{\theta 1})$. The wheel speed U can be raised through increasing the rotational speed of the rotor or increasing the rotor radius. However, increases in wheel speed and rotor span are limited by structural loading, and the higher relative Mach number of the blade may lead to decreased efficiency from increased shock losses. The degree of flow turning permissible is also limited, due to the amount of diffusion possible before flow separation and blockage occurs. [1]

The stable operating range of a compressor is limited by instabilities at low flow rates. Generally, at a given operation speed, the pressure rise across the compressor increases as the mass flow rate is decreased [2]. When the mass flow rate is reduced beyond a certain point, the compressor is no longer able to support the previous pressure rise across the compressor – instabilities in the flow occur, and there is an abrupt drop in compressor pressure rise. This sudden change in flow behavior is referred to as stall or surge, and may be very catastrophic for the gas turbine engine.

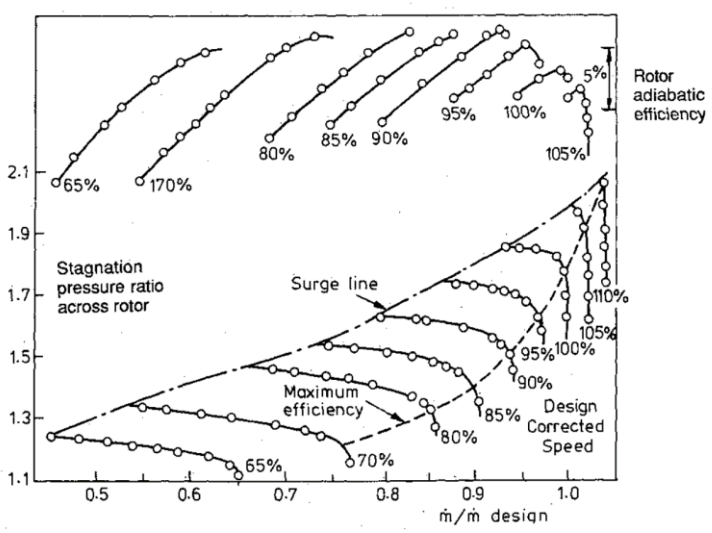

Figure 1.1 Stagnation pressure ratio and adiabatic efficiency characteristics for the rotor of a modern and efficient single-stage civil aircraft engine fan. From Freeman and Cumpsty [2].

The performance limitations of a high-speed compressor may be observed through a compressor characteristic map. Figure 1.1 is representative of a high-speed fan that is transonic or supersonic at design speed. Several observations can be made [3]: Firstly, the pressure rise characteristic becomes steeper with increasing speed, and the mass flow range between stall and choke becomes much narrower. Secondly, peak efficiency is very close to the stall limit at high speeds. To ensure an adequate stall margin, the point of operation at high speeds must be close to choke or in choke, which leads to low efficiency operation; and there may not even be enough stall margin to allow operation at higher speeds. Hence, the need for operation range is particularly important for high-speed compressors, and methods to extend the operation range such as casing treatments are under study. However, before trying to apply methods to extend the stability limit, understanding the instabilities that lead to stall and the flow field at high loading is necessary.

Experimental measurements can provide valuable insight into the flow field; however, it is difficult to obtain a complete view of the flow field. Computational models can provide a complete flow field, but sources of error and uncertainty need to be considered, and results should be compared to experiment before the numerical solution can be trusted. The goal of this work is to create a computational fluid dynamics model that would provide details of the flow features in a transonic fan.

1.2 Flow Through a Transonic Rotor

The transonic operation of the fan can be defined as having partially supersonic and partially subsonic relative Mach numbers at the rotor inlet. Note that the axial component of the flow is completely subsonic, such that disturbances from the compressor can propagate upstream and influence the incoming flow [2]. At design speed, the relative inlet flow is supersonic near the rotor shroud, and subsonic hear the rotor hub, divided along the sonic radius.

This chapter will give a general overview of some of the flow features in a transonic fan.

1.2.1 Shock System

Shocks can account for a significant part of the diffusion in the rotor. A shock occurs when the supersonic relative inflow is not able to adjust to its boundary conditions isentropically. A shock may be required to reach the high back pressure at the rotor exit, or a shock may be required to turn the flow around the blunt rotor leading edge. The supersonic section of the rotor blading makes use of the high rotational speeds, with only a relatively small change in absolute whirl velocity needed to input work into the flow. As illustrated in Figure 1.2, the compressibility of the flow is used to reduce the axial velocity to achieve this change in absolute whirl velocity; a change in relative flow angle is not required [2]. Hence, for the supersonic section of the rotor, the shock system is both a source of loss and an important mechanism to achieve diffusion.

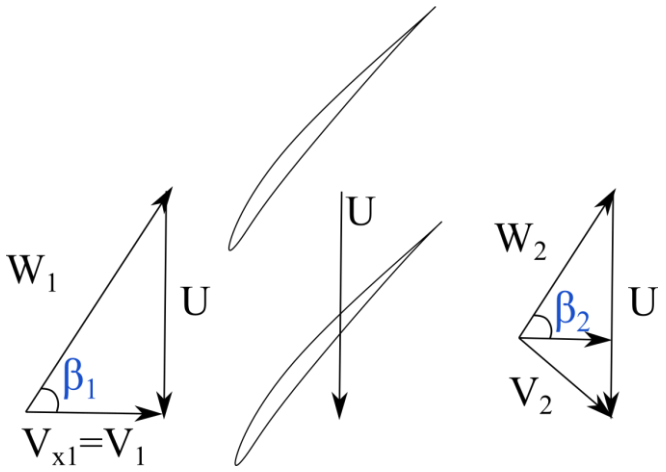

Figure 1.2 Velocity triangles for a supersonic with no turning in the relative frame.

$$\beta_1 = \beta_2,\ V_{x2} < V_{x1}.$$

Shock Structure and Location

For transonic fans near design operating conditions, a weak bow shock will precede the rotor leading edge and extend upstream of the rotor, and a passage shock will span from near the leading edge from the rotor pressure surface and impinge on the suction surface of the adjacent blade. The bow shock is created due to leading edge thickness and generates some loss; most of the shock loss is from the passage shock [2]. While some transonic rotor designs may have several oblique passage shocks, the current discussion is for a transonic rotor with only one passage shock.

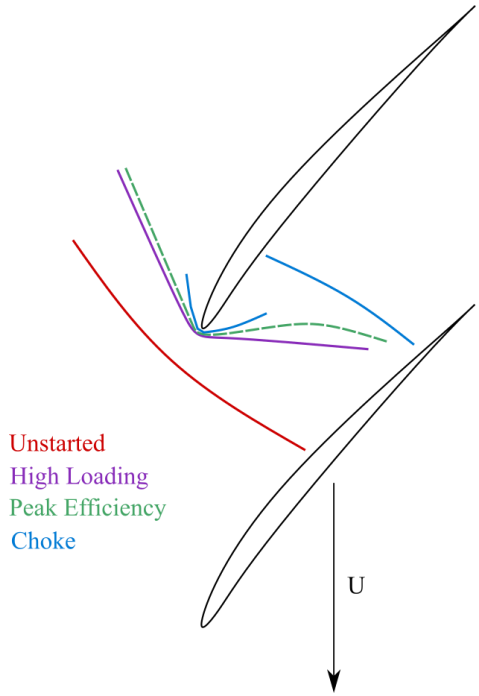

Figure 1.3 Shock structures at different loading conditions for a supersonic blade tip.

The position and stability of the shock system varies along the speedline. The passage shock may be in a started position inside the passage, or an unstarted position in-front of the rotor leading edge [4]. At design condition, the passage shock may start near the leading edge of the rotor pressure side, with a lambda foot on the pressure surface. Ideally at design point, the passage shock would be stable in a started configuration, and the shock surface would be oblique. As the operation point moves from design point towards choke, the passage shock moves further into the rotor passage; now the passage shock and the bow shock are distinct features. In choke, the passage

shock may have moved so far into the passage that the suction surface boundary layer separation created by the shock does not reattach before reaching the trailing edge of the blade. This increases loss and deviation. As the operation moves from design point towards stall, the strength of the bow shock increases as it moves upstream [5]; the passage shock also moves forward towards the inlet of the rotor and may merge with the shock front of the bow shock. As the passage shock moves towards the rotor inlet interface, the shock becomes closer to being unstarted, leading to an unstable configuration where the oscillation in shock location may increase.

Shock Losses

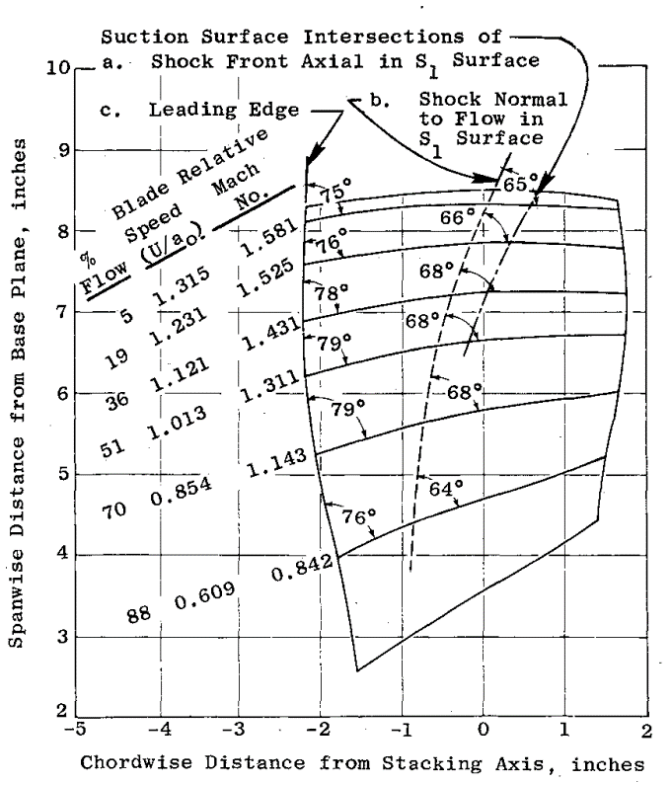

Figure 1.4 Airfoil plan view showing shock intersection with suction surface – USAF/APL HTF supersonic compressor stage, from Prince [7].

A notable portion of the loss in the rotor is due to the passage shock. A simple estimate of this loss was proposed by Miller, Lewis, and Hartmann [6]: assuming that the passage shock is a normal shock, the Mach number upstream of the shock can be found as an average of the relative inlet Mach number and the Mach number on the suction surface where the shock is expected to

impinge. This 2D approximation tends to overestimate the shock loss [1], especially if the aspect ratio of the rotor is below 2.0. This is because the shape of the passage shock along the rotor span is highly three dimensional – Prince [7] observed that the sweep of the shock along the span is responsible for much of the difference from 2D approximations. Figure 1.4 shows the backward inclination of the spanwise shock sweep. The obliquity of the shock increases the complexity of estimating the shock losses. Strasizar [8] found that near stall, bow shock and passage shock surfaces are near planar, while near peak efficiency, the shock surfaces were more complex and curved.

The spanwise extent of the shock terminates near the sonic line [9]. Generally, with decreasing radius, the shock strength also decreases; but near the sonic radius, the shock strength unexpectedly peaks. Epstein et al. [9] suggested that the losses incurred near the sonic radius may be greater than expected by considering the disruption in radial equilibrium behind the passage shock at the sonic radius; the result is that the incoming flow at the sonic radius will first accelerate through expansion waves before being compressed and coalescing into the shock. Behind the shock termination near the sonic radius, the boundary layer is subjected to a large radial pressure gradient as well as a large adverse streamwise pressure gradient. These gradients create strong spanwise secondary flows.

Many of the loss estimation methods separate shock losses from profile losses, and Cumpsty [2] noted that this separation is not physical - the approximation of shock strength is also important when considering the interaction of the shock with the suction surface and casing boundary layers. The large adverse pressure gradient across the shock may cause the boundary layer to transition, thicken, or separate. Both interactions would increase blockage and may be factors in initiating stall. These interactions are later discussed in later sections.

Shock Unsteadiness and Non-Periodicity

The three-dimensional structure of the passage shock fluctuates with time. The oscillation of the shock creates an increase in loss compared to a stationary shock at the same mean position, due to upstream motion of the shock increasing the loss more than the downstream motion of the shock decreases the loss [8]. Estimating the loss from shock unsteadiness by considering the oscillation a harmonic motion in the direction normal to the shock surface, Strasizar [8] found that accounting for unsteady oscillation of the shock in the rotor reference frame increased loss by as

much as 11%, where the shock location fluctuated by 3.5% of the chord. This unsteadiness is 3-4 times the blade passing frequency and was related to the frequency of rotor blade vortex shedding by Hathaway et al. [10]. Lee [11] proposed a mechanism for the oscillation of a shock about a mean position on the suction surface of a transonic airfoil with fully separated flow. The oscillation may be self-sustained – the movement of the shock causes a pressure wave to propagate downstream, where disturbances that propagate back upstream are generated upon the initial pressure wave reaching the wake at the trailing edge. These disturbances energize the shock wave to form a loop, sustaining the oscillation of the shock. Thus, an estimation of the shock motion frequency may be found by approximating the time it takes for a pressure wave to travel from the mean shock location on the suction surface to the trailing edge and back to the shock. This method was used by Copenhaver et al. [12] to ascertain the timestep size chosen for unsteady simulation of a transonic fan to capture shock motion.

Copenhaver et al. [12] also observed shock unsteadiness both in experiment and in CFD. They found shock unsteadiness at five times the blade passing frequency, which corresponded to the frequency of a pressure wave travelling from the shock position to the trailing edge of the blade and back, inferring that this oscillation may indeed be driven by shock-boundary layer interaction. Applying the method for calculating unsteady shock loss proposed by Strazisar [8], Copenhaver et al. [12] found that the shock oscillation in their case only increased shock loss by 1%, a small amount compared to the steady shock loss. They also noted that the while shock losses were small when the shock was inside the rotor passage, shock unsteadiness and loss would increase significantly if the shock becomes detached and stood outside the blade passage.

Harvey et al. [13] observed in experiment that shock patterns from passage to passage may not be entirely periodic, with some rotor passages exhibiting very weak shocks while others had normal shock characteristics. This non-periodicity was pronounced, especially near peak efficiency (as compared to near stall), and Harvey et al. considered that this may have been a result of geometric variations [13]; Strasizar [8] also observed an increase in non-periodicity in experiment near peak efficiency. Strasizar [8] proposed that the increased non-periodicity was due to peak efficiency being close to the transition point of the passage shock system structure from oblique shock to near normal shock in choke, and hence, at this operating point, the effects of geometrical variations were amplified.

1.2.2 Tip Leakage Flows

For transonic and supersonic rotors, the outer region of the blade is important since it is a location of both high work and high loss, and flow at the tip may be a dominant factor in determination of compressor stability [3]. In particular, the tip leakage flow (TLF) is a major contributor to loss and blockage in unshrouded rotors. The tip leakage flow is a result of the pressure difference between the pressure side and suction side of the rotor; flow near the rotor tip will attempt to move from the higher pressure side to the lower pressure side of the blade, and the shortest path tends to be through the tip clearance.

Large tip clearances are generally detrimental for both supersonic [14] and subsonic rotor tips [2], as they decrease both efficiency and stall margin. Schmucker and Schaffler [15] conducted an investigation on the effect of blade defects in high speed axial compressors and found that a 1% increase in tip clearance (ratio of tip clearance to span) resulted in a 2% loss in efficiency and mass flow. For transonic rotors, Adamczyk et al. [14] simulated the effect of tip clearance size on the endwall flow and found that as the clearance was increased, there was an increase in mass flow rate at which stall occurs. This trend for transonic rotors was also found by Copenhaver et al. [16], who observed that an increase in tip clearance from 0.27 to 1.87 % (ratio of tip clearance to chord) decreased efficiency by 6 points and decreased flow range by 30%. However, studies of shrouded subsonic rotors without a tip clearance show that having no tip clearance may also be detrimental, as there is a new mechanism of blockage through corner separation between the casing and the suction side trailing edge [17] [18]. A mechanism of optimum tip clearance was proposed by Hewkin-Smith et al. [18] for subsonic axial machines. A large tip clearance leads to a strong tip leakage vortex, which creates greater blockage and will lead to leading edge spillage of the tip leakage jet to trigger stall. Yet without tip clearance, a casing-suction corner separation will create blockage to again trigger leading edge separation and stall. Hence, there is an optimal tip clearance which is big enough to suppress the corner separation but small enough to not create significant blockage [18]. The mechanism for blockage in a transonic rotor tip near stall is not quite the same, as the unsteady interaction of the tip leakage vortex with the passage shock and casing boundary layer is a major contributor. The structure of the tip leakage flow is described in the following sections.

Supersonic Tip Leakage Flow Structure

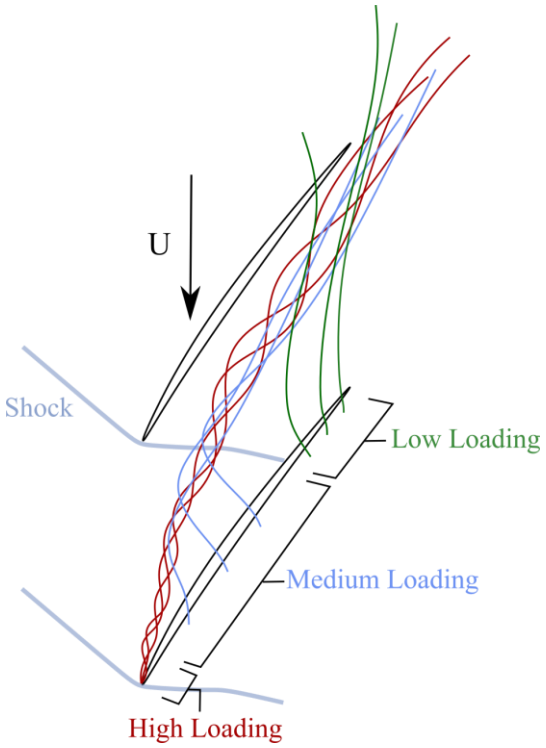

Figure 1.5 Supersonic tip leakage flow at a single operating point, categorized by loading along blade surface.

Chima [19] divided the tip leakage flow in a transonic compressor rotor into three regions based on the blade loading at the rotor tip. The first region is the strong tip leakage vortex (TLV), corresponding to the high loading at the tip leading edge and the greatest pressure gradient across the tip. Due to the high incidence induced by the casing boundary layer at the tip leading edge, the pressure gradient from the pressure side to the suction side is the greatest here, and the shear between the leakage and primary flow generates a strong tip leakage vortex. This vortex convects downstream and across the rotor passage, usually impinging on the pressure side of the adjacent blade. The angle between the tip leakage vortex and the primary flow is well predicted by Chen's model [20], which is primarily based on the pressure difference across the tip gap. This vortex will also intersect with the passage shock and cause the shock to change in shape slightly. The interaction between the shock and the tip leakage vortex is further discussed in a later section. The second region is one of moderate blade loading at the tip, behind the high loading region and in front of where the passage shock impinges on the suction surface. In this region, a highly skewed jet exits the tip gap and creates a shear layer to the primary flow. The trajectory of this jet is at a

greater angle to the primary flow than the tip leakage vortex. This thin jet meets the TLV and wraps around it to drop radially into the primary flow. The last region is a lightly loaded region behind where the passage shock impinges on the suction surface; in this region, the leakage flow lightly perturbs the casing boundary layer. The flow ingested from the pressure side in this region may also include the low momentum fluid from the TLV from the adjacent blade. The radial influence of this tip leakage flow may be 20 times greater than the tip clearance size [21].

Note that since the TLF is driven by the pressure gradient across the rotor tip, the TLF ends up primarily normal to the tip chord, with a small component in the through-flow direction in the relative frame [5]. Due to the high stagger at the tip, the TLF can have a component of negative axial velocity. This negative axial velocity will cause some displacement in the casing boundary layer, creating blockage. The reversed flow region extends across most of the suction side tip [5].

An interesting change to the tip leakage flow may occur near choke. Recall that the strong tip leakage vortex occurs at the greatest pressure gradient across the tip gap; in choke, the passage shock may no longer start at the pressure side leading edge, and the pressure gradient across the tip gap is the greatest where there is a shock to increase the gradient [5]. Hence, the formation of the strong vortex may instead start behind the shock on the pressure side.

Part Speed Tip Leakage Flow Structure

At part speed operation, the rotor Mach number may be low enough such that there is no longer a passage shock in the rotor passage. The flow may still have a small supersonic region near the leading edge; or the blade may be entirely subsonic. In this case, the features of the tip clearance flow may be very different to those of the supersonic case despite having the same inviscid driving mechanism. This difference between design speed operation and part speed operation is worth noting – if a casing treatment is to be designed for design speed, its effect on the flow field at part speed should be understood such that any modifications to the flow is not detrimental to the part speed operational range.

In a subsonic rotor, the roll-up of the tip leakage vortex may correspond to the lowest pressure contour on the suction side blade tip [17] [22]. The position of the vortex varies with tip clearance; it will move downstream of the leading edge with increasing clearance. Additionally, as the tip clearance increases, the vortex increases in size and strength. When the clearance was smaller than 1% of chord, a tip leakage vortex could not be observed [17]. Most of the loss from

the tip leakage flow does not happen within the tip gap but rather after the leakage flow exits, and a shear layer is created between the highspeed primary flow and leakage flows [17]. A simple model proposed by Rains can be used to describe subsonic flow through the tip gap [23]. Flow from the pressure side into the tip gap will separate from the corner of the blade tip, and the separation will create a vena-contracta effect. The contraction in flow area in the tip could then be modelled with a discharge coefficient and Bernoulli's equation, by assuming that the leakage flow follows a trajectory such that streamwise momentum is conserved across the gap.

From part speed experimental and computational studies of a transonic axial compressor rotor, Suder and Celestina [21] found that when the passage shock is absent, a second low momentum area may form near the trailing edge of the suction side tip. This can happen when there is a small supersonic region on the suction side leading edge tip due to positive blade incidence. An adverse pressure gradient will form at the downstream edge of the supersonic region, causing a radial migration of the flow. This radial flow will roll into a secondary vortex after meeting the tip leakage flow. The strength of the secondary vortex is dependent on the strength of the radial flow. Suder and Celestina [21] also found that the radial extent of the tip clearance flow for part-speed operation without a passage shock was significantly less than that with a passage shock.

Tip Leakage Vortex

Of the different regions of tip leakage flow, the strong tip leakage vortex is a dominant feature in determining flow stability due to its interaction with the passage shock and the subsequent blockage created.

Chen et al. [20] proposed a similarity model for the tip leakage vortex based on an inviscid slender body approach. The model essentially changed the tip leakage vortex from a 3-D steady flow to a 2-D unsteady flow in the crossflow plane. This approach was created by considering that the chordwise pressure gradients are much smaller than crossflow pressure gradients in the tip region. The resulting trajectory of the vortex core from Chen's model matched quite well with experimental values for both subsonic [20] and transonic rotors [19], indicating that the roll-up process of this vortex is dominated by inviscid effects [17] [20] [23]. With this model, only the mean blade flow angles and the camber line are needed to calculate the tip vortex trajectory.

The trajectory of the vortex core varies with operating point. As loading increases and mass flow decreases, the tip leakage vortex moves away from the suction side of the blade and towards the rotor inlet plane due to the increase in convection time (i.e. decreased axial velocity) [18] [19] [23], and the strength of the vortex increases. Chen et al. [20] found that the path of the vortex core is not sensitive to tip clearance size, although tip clearance size does affect the pattern of the crossflow and the spanwise influence of the tip leakage vortex increases as the tip clearance increases. Chen et al. also noted that the path of the vortex bends sharply as it exits the rotor passages, and the kinematic constraints of the blades on the vortex disappear [20].

Although the size of the tip clearance gap did not seem to affect vortex trajectory, it certainly affects the blockage generated by the TLV and the strength of the TLV. An increase in tip clearance increases the volume of the tip leakage flow, which increases the strength and the blockage generated by the TLV. At very small tip clearances, there may not be a detectable strong vortex portion of the tip leakage flow. Inoue and Kuroumaru [22] found that for a subsonic rotor at very small clearances, the tip leakage vortex decays as it moves downstream and could not be clearly observed in pressure contours, and a small scraping vortex existed at the corner between the pressure surface and shroud. The scraping vortex is generally a result of relative inlet skew in the casing boundary layer causing the casing boundary layer to pile up onto the pressure surface [2]. Inoue and Kuroumaru [22] also found that as tip clearance increases, the location of the greatest pressure gradient moves downstream and the leakage jet becomes stronger at this location.

1.2.3 Shock-Vortex Interaction

The interaction between the passage shock and the tip leakage vortex is a major contributor to endwall blockage [21] [19]. When the tip leakage vortex intersects the passage shock, a large low momentum region forms downstream, creating an area of blockage with near zero axial velocity. The blockage drives the tip incidence to increase [21]. At the intersection, the shape of the passage shock near the casing is distorted, and a lambda shock impinging on the casing boundary layer is formed at the shock vortex interaction [19]. The tip leakage vortex may remain continuous through the shock; however, the vortex and leakage flow may be diffused by the pressure gradient from the shock [21]. After passing through the shock, the tip leakage vortex carries the low momentum fluid to the pressure side of the adjacent blade [5]. As loading is increased, the shock moves forward, and the tip leakage vortex becomes more tangential to the

primary flow – hence, the interaction region moves forward towards the rotor inlet plane [14]. The interaction between the passage shock and the tip leakage vortex becomes stronger, and the low momentum interaction region increases in both circumferential and radial influence [21]. When the shock becomes fully detached near or at stall, the blockage from the shock-vortex interaction may reach the leading edge, causing the tip leakage flow to spill forward from the leading edge [14] [24]. This spillage will drive the shock further forward, causing the upstream flow field to adjust and decrease the mass flow rate, which will increase the blade incidence [14]. This increase in incidence will increase blade loading, and thus increase tip leakage flow and spillage [14]. This continuous buildup of blockage may eventually lead to stall.

It is also possible for the passage shock and vortex interaction to cause the vortex to breakdown and, thus, greatly increase blockage, leading to stall [25]. Vortex breakdown is an abrupt change in vortex core structure. Thomer et al. [26] categorized shock-vortex interaction into weak, moderate, and strong interactions, and differentiated oblique shock-vortex interactions (OSVI) from normal shock-vortex interactions (NSVI). The passage shock usually falls under the category of an oblique shock. In a weak oblique shock-vortex interaction, the vortex does not noticeably change in shape when it passes through the shock, and the flow field remains supersonic. In a moderate OSVI, the shock shape bends in an s-shape in the region of interaction with a small subsonic region behind the shock, and there is a small influence on vortex structure. In a strong OSVI, the vortex breaks down behind the shock to form a bubble-like structure, creating a large subsonic region; for a strong OSVI, the deformation of the shock is similar to that for a moderate interaction. Thomer et al. [26] found that a large pressure rise across the shock, as well as a small axial velocity or a large swirl velocity of the vortex, would make the vortex more susceptible to breakdown.

The change in the strength of the shock-vortex interaction may be observed across a speedline. Near peak efficiency, Hoeger et al. [5] did not observe a change in the strong tip leakage vortex due to the shock-vortex interaction, but there was a distortion in shock structure; similar observations near peak efficiency were made by Chima [19]. Near stall, Adamczyk et al. [14] and Hoeger et al. [5] observed a notable increase in the size of the cross-section of the strong tip leakage vortex as it passed through the shock, as in a moderate shock-vortex interaction. Since the vortex at high loading is both stronger and at a greater angle to the primary flow (the swirl velocity of the

vortex is high and the convective velocity of the vortex is low) and the shock at high loading is stronger, it is possible for the shock-vortex interaction to lead to a vortex breakdown.

An interesting note about the unsteady shock-vortex interaction is that the oscillation of the shock causes the blade loading to oscillate, and thus the tip leakage vortex will also oscillate [24]. Hence, the low momentum region formed from the shock-vortex interaction will oscillate in axial position.

1.2.4 Boundary Layers

The behavior of the boundary layer is important to compressor blade loading, and the amount of loss and blockage generated. The compressor flow field is dominated by a large adverse pressure gradient; this adverse pressure gradient makes boundary layers prone to separation. The separation of the boundary layer decreases the effective flow area and increases profile losses and viscous losses. The problem of boundary layer separation is exacerbated by the existence of the passage shock; the passage shock usually causes both the blade boundary layer and the casing boundary layer to separate. Separation of the suction surface boundary layer in a compressor occurs the when pre-shock Mach number is greater than approximately 1.3 [27]. The blade is usually designed to allow the boundary layer to reattach before reaching the trailing edge, but this places limits on the attainable diffusion through the rotor [27]. The shroud may be contoured to improve casing boundary layer stability, but separation may happen anyway; Chima [19] observed that the casing boundary layer separated along the entire length of the passage shock. It is also likely that the casing boundary layer encases the tip clearance. Hence, different inlet casing boundary layer thicknesses and velocity profiles will have a large influence on endwall loss [28]. Unfortunately, it is difficult to apply conventional boundary layer methods to study flow inside a compressor – the non-uniform stagnation pressure and temperature gradients in the freestream makes defining the edge of a boundary layer difficult [2].

Blade Boundary Layer

Despite the high freestream turbulence, axial rotor blade boundary layers contain both laminar and turbulent sections. The laminar portion may be small but will almost always exist due to low Reynolds number at the leading edge of the blade [2] . This laminar boundary layer at the

leading edge may transition to a turbulent boundary layer, or it may first separate and then reattach as a turbulent boundary layer; or it may separate and not reattach. Which phenomenon occurs is dependent upon free-stream turbulence and the Reynolds number based on boundary layer thickness – separation transition will likely occur with lower free-stream turbulence and Reynolds number [2]. Note that the concern with boundary layer separation on the rotor blade is primarily for the suction surface. Since it is easier for the laminar boundary layer to separate compared to a turbulent boundary layer, transition to a turbulent boundary layer is desired before reaching the passage shock. Transition without separation may occur through natural transition or bypass transition. Natural transition is triggered when the laminar boundary layer grows unstable through the amplification of Tollmien-Schlichting waves [29]. If there is high free-stream turbulence, the initial stages of a growing instability in natural transition is skipped and bypass transition occurs with the appearance of turbulent spots [29]. Due to the high level of turbulence and unsteadiness in the compressor flow field, natural transition can usually be neglected and bypass transition can be assumed to occur when the Reynolds number based on momentum thickness is greater than 160 [2].

1.2.5 Blockage

Blockage is a reduction in effective flow area due to regions of low momentum in the flow, and can be defined as:

$$B = 1 - \frac{effective\ area}{geometric\ area} \tag{1.2}$$

Suder [30] proposed a methodology to systematically quantify the blockage for an axial compressor rotor:

$$B = 1 - \frac{A - \int \delta^* dr}{A} \tag{1.3}$$

Where A is the geometric area, and δ^* is the integral of the velocity-density deficit across the blade passage, evaluated at each radius. From a computational model of NASA Rotor 37, Suder [30] found that including the effect of the velocity variation alone was sufficient to evaluate the general trends of blockage across the rotor passage. Hence, $\delta^*$was redefined as the integral of just the velocity deficit across the blade passage. The velocity deficit region is defined by examining the gradient of the axial velocity in the crossflow directions, and specifying a cutoff value; note

the resulting blockage found is not significantly influenced by the specific value of the cutoff, due to the drastic increase in velocity gradients inside the defect region [30]:

$$\textbf{Defect region is where } \left|\frac{\partial u}{\partial r}\right| + \left|\frac{\partial u}{\partial (r\theta)}\right| \geq cutoff \tag{1.4}$$

Blockage can be an important indicator of the compressor loss, pressure rise, and flow range. In the core flow, blockage results in an acceleration of the flow through the blade passage; less blockage corresponds to more work input into the flow [30]. The choke mass flow rate is also dependent upon blockage. Due to high loading and small flow range, the performance of high-speed compressors is particularly sensitive to changes in blockage.

1.3 Computational Fluid Dynamics

Computational fluid dynamics (CFD) has been used extensively as a design tool for compressors. CFD simulations can provide general flow features and sources of loss but may not precisely reproduce the flow due to error and uncertainty. The sources of error include numerical errors from the discretization scheme, modelling errors from inaccurate representation of physics, uncertainties in boundary conditions and geometry, and additionally for steady simulations, the assumption of steady flow [28].

An extensive comparison of turbomachinery CFD was conducted through the 1998 AGARD blind study on NASA Rotor 37 (a supersonic axial rotor) and the DLR turbine stator [31]. Researchers were invited to compute the test cases with 3D Reynolds-Averaged Navier-Stokes codes, and the results were compared to experimental data. For Rotor 37, the simulations improved understanding of the flow field by capturing flow features such as the shock, tip leakage flow, and suction surface boundary layer separation due to the shock. However, the test cases generally underpredicted adiabatic efficiency and overpredicted pressure ratio. The discrepancy in efficiency was suggested to be a result of overpredicting loss in the tip region. It was also observed that the predicted shock was slightly more upstream than found in measurement, suggesting that the shock strength was overpredicted. Furthermore, most of the test cases found the choke mass flow rate to be slightly lower than measurement. The test case results also varied widely from each other depending on choice of turbulence model and grid construction. The summary report recommends that mixing length turbulence models should be avoided, and that 500,000 or more grid points are needed to model a single blade domain, depending on the turbulence model.

There is also an interesting example of discrepancy caused by modelling unknowns in this Rotor 37 blind study. A small axial gap in the hub just upstream of the rotor leading edge was not initially included in the test cases. This small gap was an important contributor to hub corner stall. The gap led to a blind cavity and the importance of this gap was unknown at the time of the blind case; thus, the existence of hub corner stall as suggested by experiment was not captured by most test cases. The discrepancy between CFD and experiment led to the discovery that mass flow was coming in and out of this gap with the rotation of the rotor. When the effect of this inflow and outflow was added to CFD, the hub corner stall was captured.

Hence, while CFD is a very valuable tool for understanding the compressor flow field, its limitations should be considered, and calibration with experiment with inclusion of all important geometry is important to setting up a robust model.

1.4 Research Objectives

A transonic fan has been donated by Honeywell Aerospace to the Purdue University High-Speed Compressor Research Laboratory for the purposes of studying casing treatments and inlet distortion under the Office of Naval Research Power and Propulsion Program. The purpose of this work is to provide a computational baseline for modelling the flow physics in the tip region of this transonic fan before casing treatment is applied.

To achieve this goal, the impact of various modelling decisions and uncertainties on flow features near the rotor tip was considered using steady CFD. Firstly, a grid convergence study was conducted to verify the quality of spatial discretization. Secondly, a speedline was completed for 100% aerodynamic design corrected speed, to compare between different loading conditions, and the effect of exit condition on solution stability is considered. Finally, a preliminary turbulence study was made for comparing the effect of turbulence on boundary layer separation and shock-vortex interaction. An unsteady simulation was also run near peak efficiency to provide some idea of the unsteady characteristics of the flow.

2. COMPUTATIONAL MODEL

A computational model is developed to study the flow field, and to plan for future experimental research in inlet distortion and casing treatments. The purpose of this chapter is to describe the setup of the computational model for the steady and unsteady simulations. First, the problem scope is defined, and then the solution method is described. GridPro and Turbogrid were used to mesh the model, and ANSYS CFX 19.1 was used as the solver.

2.1 Domain Description

The control volume of the model is defined from the experimental fan rig set up, as shown in Figure 2.1.

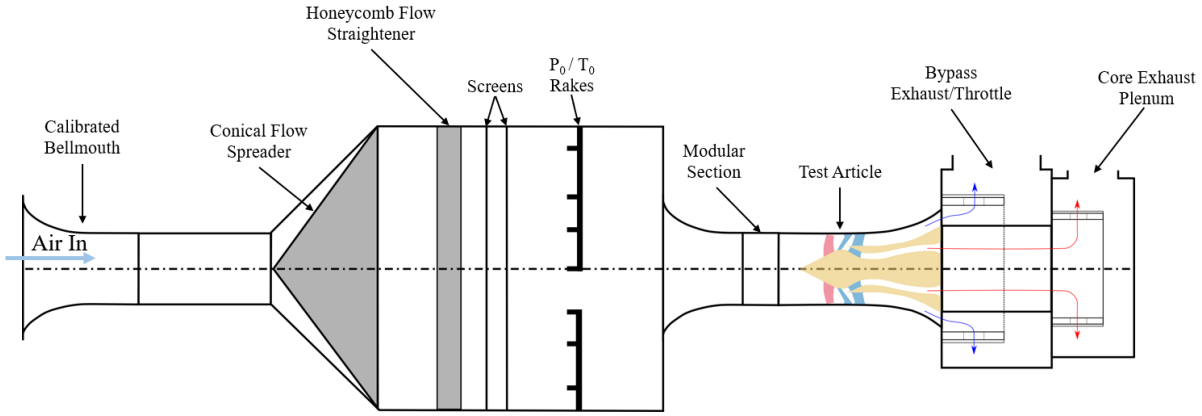

Figure 2.1 Flow path description of experimental set up.

The computational domain is defined to be as small as possible, while still including enough space upstream and downstream of the test article to assume uniform inflow and mixed-out wakes in the outflow.

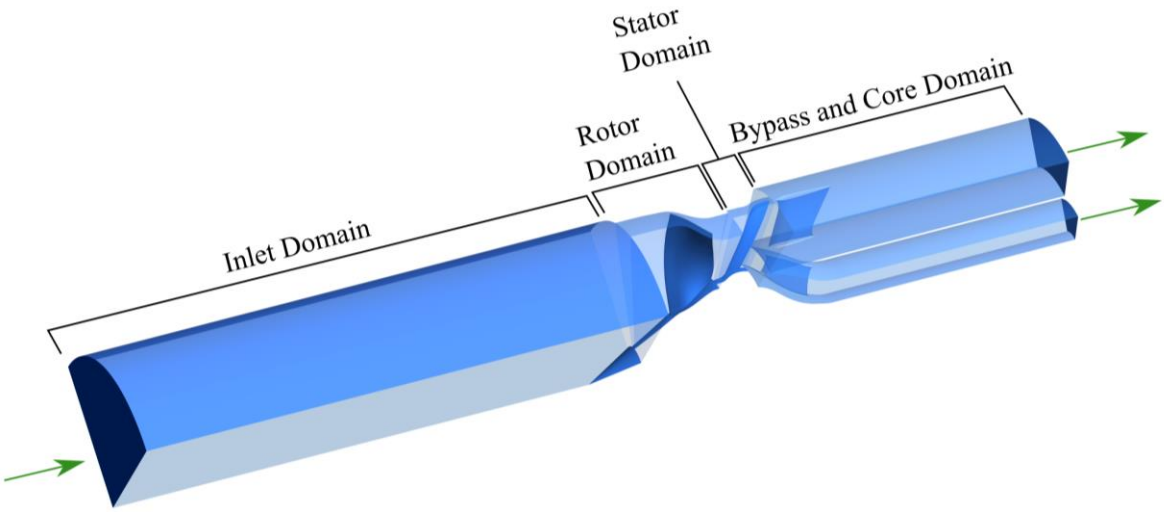

Figure 2.2 Example of single passage computational domain.

To conserve computational cost, a single passage model that can be patterned into a full annulus model is used for many of the steady state CFD cases. An example of this single passage model is shown in Figure 2.2, which has been distorted to hide any proprietary design features. Due to having both rotating and stationary components, as well as different numbers of vanes and struts, the flow path of this single passage model is divided into several domains, consisting of an inlet domain, a rotor domain, a stator domain, and an outlet domain containing the bypass outflow and the core. Each domain has a different pitch, and the flow domains are connected by interfaces. To accommodate for different pitches between the domains, as well as different frames of reference between rotating and stationary domains, the mixing plane method is applied across interfaces for steady simulations. Generally, walls in each domain are modelled as adiabatic rough walls with a no-slip boundary condition. Due to the model not being a full annulus, rotational periodic boundaries were placed for each domain.

The inlet domain consists of ducting upstream of the fan and a part of the spinner. This domain is stationary, with the spinner set to be a rotating wall. The domain ends one tip chord upstream of the rotor, where the aerodynamic interface of the fan would be. The extension of this section far upstream is to allow distance for mesh inflation, as a method of damping reflections from the inlet. Due to the extended inlet, the boundary layer would become thicker than is representative of experimental conditions. To achieve a more realistic boundary layer thickness,

part of the shroud of the inlet has been modelled as a smooth free-slip wall, and the boundary layer only starts to build when it reaches the rough no-slip wall. The length of the free-slip wall will be adjusted until computational boundary layer profiles at the AIP matches the experimental results.

GridPro was used to create the structured hexahedral inlet domain, and a periodicity of 90 degrees was maintained to ensure adequate mesh quality around the spinner.

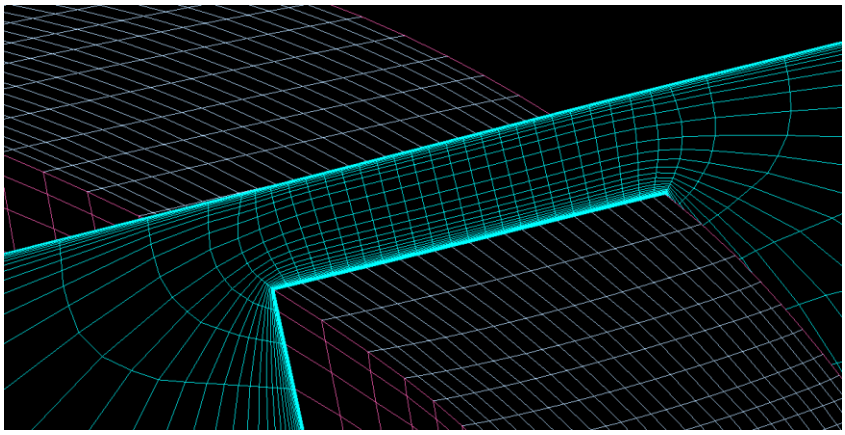

(a) GridPro mesh across the rotor tip. Blue cross-section of the mesh displays the O-grid mesh topology used to mesh the clearance region.

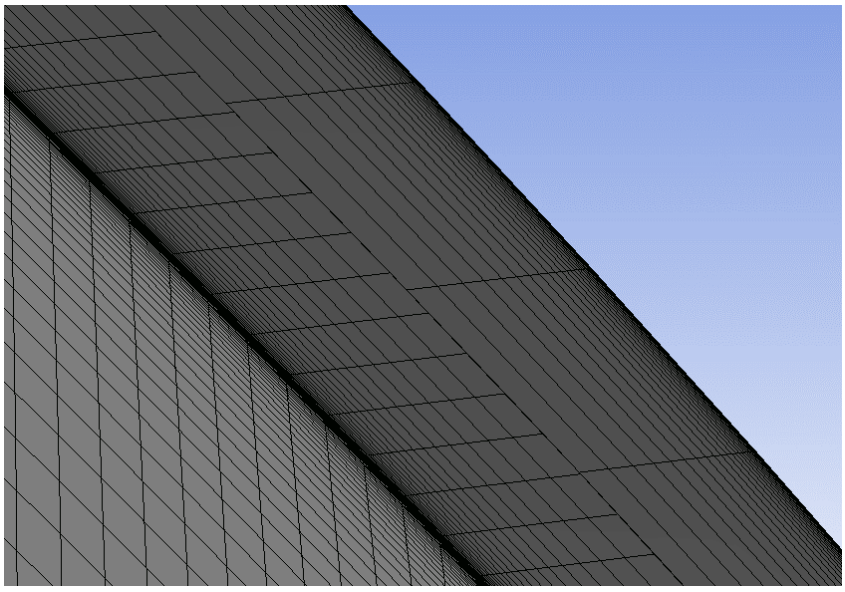

(b) TurboGrid mesh across the rotor tip.

Figure 2.3 Mesh across the rotor tip. There is a large difference between the cell size between the pressure and suction surfaces due to the large twist of the blade, and an interface is needed to transfer information between these cells.

The rotor domain consists of one rotor blade and is 1/22nd of the full annulus. This is a rotating domain, with the circumferentially uniform shroud set to be a counter-rotating wall. The large amount of twist in the blade and the existence of a tip clearance present challenges to creating a good quality structured mesh. Both meshes made in Turbogrid and GridPro were considered, as illustrated in Figure 2.3. The main discrepancy between the two is how the tip clearance is meshed. Turbogrid provides a high-quality mesh that preserves high orthogonality from hub to tip; however, Turbogrid has non-conformal meshing at the blade tip, with an interface used for transferring information across the gap through interpolation. Observing the differences in cell sizes between the sides of the tip gap in Turbogrid that necessitated this interface, information and gradients will be smeared and lost when interpolating across the interface. Considering the importance of the tip region to both tip clearance flows and future incorporation of casing treatments, GridPro is used to create a conformal mesh around the blade using an O-grid topology. Since the location of the tip leakage vortex is strongly dependent upon the greatest pressure gradient across the tip – if the tip is not conformally gridded, the smearing of pressure gradients across interpolation may add error to both the location and strength of the TLV.

The stator domain consists of one stator vane and is 1/53rd of the full annulus. This is a stationary domain, with the stator vane extending the full span from hub to shroud. The mesh was created in Turbogrid.

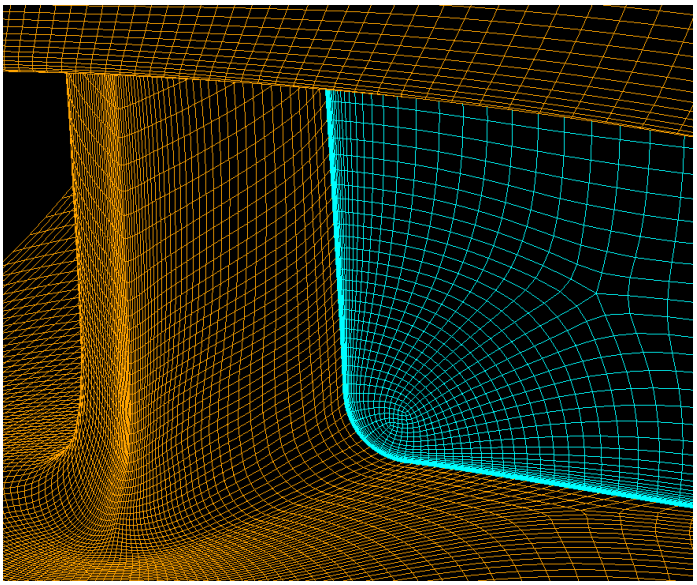

Figure 2.4 GridPro mesh for the bypass and core domain; core strut. Blue cross-section of the mesh displays the topology used to mesh the fillet region.

The outlet domain with the bypass and core outflows contains 1 strut in each domain and is $1/8^{th}$ of the full annulus. GridPro was used to create this stationary domain, and the topology used to create the fillets can be observed in Figure 2.4. Here the outlets were extended to allow the wakes behind the struts to mix a bit before reaching the exit and to reduce artificial reflections from the outlet boundary conditions by using mesh inflation. Near stall, the increasingly unstable flow is likely to create more reflections, and different treatments are later discussed.

2.1.1 Hot and Cold Geometry

Since the fan blades are thin and have relatively high aspect ratio, the aerodynamic, thermal, and centrifugal loading will cause the running rotor geometry to deviate from the stationary geometry. This deformation is emphasized in the tip region where the rotor is highly loaded and the thinnest. Generally, the aerodynamic and centrifugal loading on the blade will cause it to untwist [32]. Untwist is defined as the difference between the static tip stagger and the running tip stagger of the fan.

This untwist can reduce the tip stagger by as much as 5 degrees [32]. The untwist of the blade can be divided into untwist due to the centrifugal load and untwist due to the pressures from the aerodynamic load. Typically, untwist is positive and causes the blade passage to open; since opening the blade passage increases the throat area, the untwist can shift the constant speed characteristic to higher mass flow rates [32]. This untwist increases the flow capacity in supersonic sections by making the leading edge more axial. On a constant speed characteristic, where the centrifugal load is constant, the aerodynamic load increases as the operation point moves from choke towards stall, increasing untwist. For a transonic fan that has an aspect ratio of 2.3 and tip stagger in the range of 63 to 68 degrees, Wilson et al. [32] found that the change in untwist along a constant speed characteristic could be as high as 1.8 degrees; hence, evaluating aerodynamic performance in CFD using a constant hot geometry can produce noticeable differences compared to experimental values.

There are many variations in blade hot geometry that may occur due to operation point, manufacturing tolerances, etc. Currently, only one hot geometry is being used - the running (hot) geometry was provided to us by Honeywell, and variation with speed and aerodynamic loading has not been considered.

2.2 Solver Set Up

ANSYS CFX (19.1) is the commercial CFD solver used for all simulations. This solver is an implicit 3D Navier-Stokes solver that uses the finite-volume method [33]. A second order advection scheme is used.

2.2.1 Boundary Conditions

For the computational model to converge and give reliable solutions, boundary conditions should be carefully specified such that the problem is well-posed. Using the definition of Hadamard, a problem is well-posed if (1) the solution exists, (2) is unique, and (3) depends continuously upon the initial and boundary data.

Inlet and Outlet Boundary Conditions

While there are a variety of inlet and outlet condition pairs that may give stable solutions, additional considerations need to be made to attenuate reflections. Due to the finite volume method being employed (vs. finite elements with natural boundary conditions), and due to the solution having to depend continuously on the boundary data, there is an unfortunate problem of artificial reflections from inlet and outlet boundaries. This problem originates from having a truncated domain and not having exact details of the flow at the inlet and exit boundaries. The lack of extremely precise details at these boundaries imply that the flow solution solved by the model will never exactly match the prescribed boundaries; the end solution will include artifacts of this numerical error. Thus, boundary conditions that are more rigid, such as constant static pressure at the exit, should be avoided since they exacerbate the problem. Reflections may be avoided by extending the computational domain enough such that far-field assumptions may be made, e.g. uniform atmospheric conditions, such that the flow has mixed out enough and there are no specific details where discrepancies could happen. However, the size of the computational domain required to allow valid far-field conditions is very large and would be computationally expensive. The truncation of the computational domain must then also be carefully considered – this truncation should be sufficiently far away from flow features such as re-circulation zones to avoid the necessity of additional boundary details to be matched.

Table 2.1 provides some configurations of inlet and outlet boundary conditions that may give stable solutions for problems with one inlet and one outlet, as recommended by CFX Modeling Guide [34]. Note that total pressure at the outlet cannot be specified as it is unconditionally unstable. In addition to listed inlet conditions, total temperature and flow direction are specified at the inlet.

Table 2.1 CFX recommendations on boundary condition configurations [34].

Configuration number	Inlet	Outlet	Robustness in CFX
1	Mass flow or velocity	Static pressure	Most robust, and inlet total pressure is part of the implicit solution
2	Total pressure, total temperature, flow direction	Mass flow	Robust, static pressure at outlet and velocity at the inlet is part of the implicit solution
3	Total pressure, total temperature, flow direction	Static pressure	Sensitive to initial guess and mass flow through entire domain is part of the implicit solution
4	Static pressure	Static pressure	Unreliable, and inlet total pressure and mass flow is part of implicit solution

From a study by Mueller et al. [35] on reflective behaviors of different boundary conditions in CFX for turbomachinery, the more rigid boundary conditions (such as constant static pressure outlet and velocity outlet) were much more reflective than less rigid conditions (such as average static pressure outlet and mass flow outlet). Through calculating the reflection coefficients, Mueller et al. [35] found that for inlet boundary conditions, a velocity inlet condition created the largest reflections, followed by a mass flow inlet condition; a constant total pressure inlet condition created the least reflections. For outlet boundary conditions, a velocity outlet condition and a constant pressure outlet condition created the largest reflections, followed by an average static pressure outlet condition; a mass flow outlet condition created the least reflections.

The quality of the boundary conditions chosen also depends on the operation point. Figure 1.1 showed that the constant speed characteristic is nearly vertical during choke. Conversely (not shown on figure), the static pressure rise from peak efficiency to stall is nearly horizontal. This presents some challenges in finding a unique solution: near stall, the static pressure rise does not

change much with changing mass flow, and hence a static pressure outlet condition may not give a unique solution; in choke, the mass flow rate does not change with the varying pressure rise, and hence mass flow inlet or outlet may not give a unique solution. This implies that configuration 2, as shown in Table 2.1, may be an acceptable boundary condition for near stall operation, and configuration 3 would be acceptable for near choke simulations, but neither could be used for the entire speedline. Configuration 1 with mass flow inlet and static pressure outlet would be an exception to the aforementioned uniqueness problem, since for a given mass flow rate and a given pressure rise, there is only one solution on the constant speed characteristic. However, configuration 1 is very inconvenient to use. Since the inlet-corrected mass flow rate is corrected with inlet total pressure and total temperature, having the inlet total pressure as part of the implicit solution does not allow the operation point of the simulation to be set *a priori*. Furthermore, configuration 1 is not as decent as 2 and 3 at attenuating reflections.

Note that the mass flow exit may be replaced with an exit-corrected mass flow exit for less rigid boundary conditions. The exit-corrected mass flow is defined as [34]:

$$\boldsymbol{m_{exit\ corr} = m_{exit} \frac{\sqrt{T_{o\ exit}/T_{ref}}}{P_{o\ exit}/P_{ref}}} \tag{2.1}$$

This variable is meaningful at the core flow exit of the fan, where exit-corrected mass flow rate may be the inlet-corrected mass flow rate to the compressor behind the fan. This is a less rigid boundary condition compared to mass flow exit, as the mass flow rate is specified in this condition but has room to deviate through the slight flexibility of implicit exit total pressure and exit total temperature solutions.

Another layer of flexibility is added for this fan with both bypass and core outflows. The mass flow between the bypass and core is related by a bypass ratio, kept near constant across a speedline. This bypass ratio may be set explicitly by specifying mass flow rate at both the bypass and core exits, or boundary conditions may be chosen such that bypass ratio is an implicit part of the solution. In an experiment, the bypass ratio is set by adjusting the throttles of the bypass and core exhaust flows, and the mass flow rate is a result of the adjustment to the back pressure. Thus, it would be closer to experiment to allow the bypass ratio of the model to be reached naturally. Honeywell [] suggested using average static pressure bypass outlet with mass flow core outlet, with a total pressure inlet condition. This configuration would allow the simulation to traverse the

entire speedline. Another method to traverse the speedline is to use exit-corrected mass flow at both exits with a total pressure inlet and exit, since the exit-corrected mass flow is a representation of the compressor loading and is unique at each operation point long the speedline.

In keeping boundary conditions as close to experimental conditions as possible, the combination of implicit and explicit solutions is more likely to give a solution representative of the flow physics.

Note that time invariant boundary conditions are inaccurate in the presence of unsteadiness in the flow, such as near stall. When boundary conditions don't match the physical solution of the flow field, the solution may diverge, or reflections may occur. To mitigate this problem, the method employed is to gradually coarsen the mesh towards the flow inlet and outlet. This is a simple method that uses increasingly insufficient spatial discretization to dissipate flow fluctuations [35].

Near-Wall Treatment

No-slip boundaries are enforced at solid walls. The near wall requirements of the mesh depend greatly on the turbulence model. The non-dimensional wall distance $\boldsymbol{y_+}$ is an important parameter for evaluating discretization near the wall:

$$\boldsymbol{y_+ = \frac{y u_\tau}{v}}, \tag{2.2}$$

Where y is the wall distance, u_τ is the friction velocity, and v is the local kinematic viscosity. Turbulence models that integrate to the wall, such as k-omega, require grid points in the laminar (viscous) sublayer of the boundary layer; ideally, y_+ should be 1 or less for these models. Turbulence models that make use of a wall function, such as k-epsilon, require the first point of the boundary layer to be in the fully turbulent (log-law) region of the boundary layer, where y_+ is on the order of 50 [36]. CFX uses scalable wall functions to allow the use of grids for that are too fine for models that require a wall function. Unfortunately, the value of y_+ is dependent upon the flow solution and not known *a priori*; thus, the y_+ of the boundary layer had to be adjusted iteratively. These iterations were done for one operating point at mid-range, and the resulting boundary layer thicknesses were applied to all operating points on the same speedline; it is assumed that the changes in y_+ are small. Before applying roughness to the wall, the boundary layer y_+ was between 1 and 2.

Surface roughness was included in most simulations. In CFD, surface roughness can be modelled as small spheres lined on a smooth surface. The diameter of these spheres is defined as equivalent sand-grain roughness. The wall effectively shifts into the flow field by the radius of these spheres to simulate the correct displacement caused by the sand-grain roughness [33]. The sand-grain roughness K_s needs to be converted from the measured arithmetic roughness R_A through a correlation:

$$K_s = AR_A, \tag{2.3}$$

Where A is a constant. Using revised results from Koch and Smith [37], [38], a factor of 8.9 is used for A.

Interfaces for Steady Simulation.

The mixing plane uses circumferential averaging of fluxes to transfer information between domains with different pitches or different frames of reference. The mixing plane is helpful for steady simulation of the compressor. In the mixing plane approach, the flow is divided into circumferential bands, and the mass, momentum, and energy is conserved in each circumferential band [39]. Although the flux through each circumferential band is conserved, the fluxes are not taken to be circumferentially uniform [39]. This interface creates mixing loss [33].

Interfaces for Unsteady Simulation

The time-transformation interface may be used in unsteady CFD for modelling the interface between a rotating and stationary domain, e.g. the rotor domain and the stator domain. The two domains need to be close in pitch; at the rotor-stator interface, the flow profile is scaled to match across the interface (as in a profile transformation). The computational domain is inclined in time – the periodic boundaries of each domain is phase shifted in time, e.g. the rotor and stator domains are marching forward in time with different timesteps. This transformation in time allows the correct physical time to be preserved on both sides of the rotor-stator interface, such that there is no frequency error [33].

2.2.2 Turbulence Modelling

Turbulence plays an important role in the transport, mixing, and dissipation of momentum and energy. Pertaining to compressors, the choice of turbulence modelling affects entropy generation in tip regions and boundary layer separation. A preliminary study on the choice of turbulence model was conducted, and the results are presented in Chapter 3.

Due to computational cost, only Reynolds-Averaged Navier-Stokes (RANS) simulations have been considered in this study. For RANS, the Navier-Stokes equations are decomposed into mean component and fluctuating components. The four equations now have more than four unknowns – the unknowns of the flow field are now the three components of mean velocity, mean pressure, and the Reynolds stresses which are the velocity covariances. To close the problem, additional equations that describe the Reynolds stresses are needed; the choice of this description is the turbulence closure. The turbulence closures considered in this study fall into three categories: eddy-viscosity models, Explicit Algebraic Reynolds Stress Model (EARSM), and Reynolds Stress Models (RSM).

Eddy-viscosity models are based on the turbulent-viscosity hypothesis. The turbulent-viscosity hypothesis assumes that the deviatoric Reynolds stress is proportional to the mean rate of strain, analogous to a Newtonian fluid's stress and rate of strain relation, except viscosity of the fluid is replaced with the concept of eddy-viscosity [36]. This assumption may be poor when turbulence does not behave like a viscous fluid, but in general for simple shear flows this is a reasonable assumption [36]. The two equation models considered are k-omega, k-epsilon, Shear Stress Transport (SST), and Baseline k-omega (BSL). Each of these models has its strengths and shortcomings. The k-epsilon model performs poorly for boundary layers with strong pressure gradients; the k-omega model is robust near the wall, but results depend heavily on the freestream [36]. The BSL model and SST models both try to combine the best parts of k-epsilon and k-omega; the BSL model is not sensitive to the freestream and performs well in mild adverse pressure gradients [40]. However, the BSL model fails to predict flows with strong pressure gradients and separation [40]. The SST model is an improvement to the BSL model to account for the transport of the principal turbulent shear stress [40]. Unfortunately, eddy-viscosity models do not include the effects of system rotation and streamline curvature; an empirical curvature alteration to eddy-viscosity models to include these effects, proposed by Spalart and Shur [41], is included in our simulations.

The closure of EARSM is between that of the eddy-viscosity models and RSM models. EARSM is not limited to Reynolds stress isotropy like eddy-viscosity models but contains more approximations than RSM models. The Explicit Algebraic Reynolds Stress Model considered in this study is BSL-EARSM.

The most complex closure considered here is RSM. These models do not use the turbulent-viscosity hypothesis, but instead solve transport equations for individual Reynolds stresses and the dissipation rate [36]. RSM models are shown to be better at complex flows than eddy-viscosity models, especially for flows with mean streamline curvature, flows with strong swirl or rotation, secondary flows, and flows with sharp gradients in the mean flow [36]. The Reynolds Stress Model considered in this study is BSL-RSM.

3. STEADY SIMULATION DEVELOPMENT AND RESULTS

The CFD model needs to be verified and validated to build confidence in numerical results. The definitions of verification and validation as given by Roache [42]: Verification is "solving the equations right", and validation is "solving the right equations". In the case of validation, the implementation of Navier-Stokes equations in ANSYS CFX has been validated against many benchmark cases; the task here is to make sure that the assumptions in the computational model are suitable for the flow inside a compressor. These considerations are present in the choice of inlet and outlet boundary conditions, interfaces between domains, near-wall treatment, and turbulence modelling. To complete validation, CFD results need to be compared with experimental results. In the case of verification, the spatial discretization and temporal convergence of the models is examined. Quality of the spatial discretization is assessed with a grid convergence study based on the Richardson extrapolation, applying the procedure from Celik [43]. Quality of the temporal convergence is considered in Chapter 4 where the periodic unsteady flow field is assessed with methods from Clark and Grover [44].

3.1 Steady Convergence Criteria

For steady simulations, three criteria are used to assess iterative convergence. Firstly, several overall performance parameters are monitored as the solution iterates. These parameters are the bypass and core total pressure ratios (TPR), the bypass and core total temperature ratios (TTR), the bypass and core flow adiabatic efficiencies ($\eta_{adiabatic,}$), and the bypass ratio (BPR), and they are defined as follows:

$$TPR_{bypass} = \frac{P_{O,bypass}}{P_{O,inlet}} \tag{3.1}$$

$$TPR_{core} = \frac{P_{O,core}}{P_{O,inlet}} \tag{3.2}$$

$$TTR_{bypass} = \frac{T_{O,bypass}}{T_{O,inlet}} \tag{3.3}$$

$$TTR_{core} = \frac{T_{O,core}}{T_{O,inlet}} \tag{3.4}$$

$$\eta_{adiabatic,bypass} = \frac{TPR_{bypass}^{(\gamma-1)/\gamma} - 1}{TTR_{bypass} - 1} \times 100\% \tag{3.5}$$

$$\eta_{adiabatic,core} = \frac{TPR_{core}^{(\gamma-1)/\gamma} - 1}{TTR_{core} - 1} \times 100\% \tag{3.6}$$

$$BPR = \frac{m_{dot,bypass}}{m_{dot,core}}. \tag{3.7}$$

The bypass parameters are evaluated in front of the bypass struts, and the core parameters are evaluated in front of the core struts, both where rakes are located in the experimental set up. Since the flow is non-uniform, these overall performance parameters are acquired through averaging stagnation temperature and pressure. The choice of the type of average affects both the value and meaning of the results. Here, stagnation variables are calculated as mass-averages at each location. If the non-uniform flow is to be equated to a uniform flow with equivalent enthalpy flux and entropy flux, the mass-average should be used for the stagnation temperature and the availability-average should be used for the stagnation pressure [45]. However, although it is difficult to physically justify the mass-average of stagnation pressure, the mass-average and availability-average will give very similar results if the variation in stagnation pressure is small compared to the absolute pressure [45]; this is true for the locations inside this fan where stagnation properties are averaged. The first criterion for iterative convergence is that the overall performance parameters have not changed (to three decimal places) in the last several hundred iterations.

Secondly, convergence is observed through monitoring the RMS of the normalized residuals. The residuals are representative of the how close the solution is to satisfying the approximation of the Navier-Stokes equations at any point in space; if the computational model is satisfied exactly, the residuals will be zero [33]. These residuals are normalized in each domain by the solution range. As the solution iterates, the RMS of the normalized residuals are reduced until eventually the reductions level off. The second criterion for iterative convergence is that the RMS of the normalized residuals are no longer observably reducing, and are in the order of 1e-4 or smaller.

Lastly, the global domain imbalance is monitored. In CFX, domain imbalances of the transport equations check the flux of the conserved variables through each domain; small values of imbalance indicate conservation is close to being achieved. The third criterion for iterative convergence is that the global domain imbalances are less than 0.005%.

Some leniency is given for the more complex turbulence models such as RSM and EARSM. The flow field inside a compressor is highly unsteady, and it is suspected that the solutions of more complex turbulence models may be more unstable due to capturing more features of turbulence. Convergence is harder to define in this case; but, an unstable solution may still be a valid solution if the flow is known to be unstable experimentally, and thus, the unsteadiness of the solution may be attributed to a physical phenomenon [42].

3.2 Grid Convergence Study

The optimal refinement of the mesh depends on a trade-off between the computational cost and the quality of the numerical solution. A finer mesh usually means flow features are better resolved and there is less smearing of gradients; however, it may be more time consuming and difficult to reach convergence. A coarser mesh may converge faster, yet the error in the numerical solution must be considered. A grid convergence study was conducted for coarse, medium, and fine meshes. The fine mesh was created first, and then coarsened uniformly in all directions by 0.7 times to create the medium mesh, and by 0.5 times to create the coarse mesh; the element counts are displayed below in Table 3.1.

Table 3.1 Mesh elements for grid convergence study; single passage model.

	Coarse mesh	Medium mesh	Fine mesh
Inlet domain	2,755,200	6,679,680	17,548,800
Rotor domain	2,296,008	6,523,344	14,484,672
Stator domain	754,664	2,119,002	4,068,000
Bypass and core domain	2,242,880	7,123,116	13,758,848
Total	**8,048,752**	**22,445,142**	**49,860,320**

The first layer thickness of all three meshes were increased accordingly from the fine mesh to the coarse mesh, and the growth rate of the boundary layer was kept the same across all meshes at 1.2. The target y+ is 1 for the fine mesh, 1.4 for the medium mesh, and 2 for the coarse mesh; the resulting average y+ for each wall is displayed in Table 3.2. Since the y+ could only be found *posteriori*, a coarse mesh was iterated upon to reach an approximate average y+ of 2 with maximum y+ of less than 6.

Table 3.2 Average y+ for walls of each domain, found posteriori. The target first layer y+ is 1 for the fine mesh, 1.4 for the medium mesh, and 2 for the coarse mesh.

Domain	Wall	Coarse mesh	Medium mesh	Fine mesh
Inlet domain	Casing	1.94	1.39	0.98
	Spinner	1.94	1.39	0.98
Rotor domain	Rotor shroud	2.02	1.45	1.00
	Rotor hub	1.86	1.34	0.94
	Rotor blade	1.87	1.35	0.94
	Rotor blade tip	0.22	0.16	0.11
Stator domain	Stator shroud	1.88	1.33	0.93
	Stator hub	1.85	1.34	0.94
	Stator vane	1.29	0.95	0.67
Bypass and core domain	Bypass shroud	2.08	1.47	1.03
	Dividing wall	1.78	1.30	0.91
	Core hub	1.87	1.33	0.93
	Bypass strut	1.92	1.39	0.99
	Core strut	1.90	1.37	0.96

The Richardson Extrapolation combines the solver solution from multiple systematically refined grids to extrapolate a higher order approximation of the solution. For example, since the CFX solver gives a second-order accurate approximation to the Navier-Stokes equations, the Richardson Extrapolation will give a third-order accurate approximation. As the grids are refined, the spatial discretization error will decrease and the solver solution will approach this higher-order approximation asymptotically. Unfortunately, this higher-order estimate cannot be used as an improved solution – it does not maintain conservation properties [42], hence, it does not actually satisfy the equations being solved. However, the difference between this higher-order estimate and the solver solution is a very helpful measure of discretization error. Let the representative grid size h be defined as [43]:

$$h = \left[\frac{1}{N}\sum_{i=1}^{N}\Delta V_i\right]^{1/3} \tag{3.1}$$

Where N is the total number of elements and ΔV_i is the volume of each element. Let the grid refinement factor be defined as:

$$r = \frac{h_{coarse}}{h_{fine}}. \tag{3.2}$$

The grid refinement factor should be above 1.3 [43], to better isolate the effects of grid refinement. Following procedure from Celik et al. [43], the Grid Convergence Index (GCI) is the error estimator for each grid found with the Richardson Extrapolation with a factor of safety applied, where GCI^{21} is the percent error for the fine mesh found with the fine and medium mesh solutions, and GCI^{32} is the percent error for the medium mesh found with the medium and coarse mesh solutions. An observed rate of convergence for the solution with increasing refinement to the mesh can be found with this procedure; this should be close to the formal order of accuracy of the solver.

Note that this grid convergence study was conducted using a single operating point near the top of choke on the 100% speedline; the same inlet and outlet boundary conditions are used. The turbulence model used is SST with curvature correction, and smooth no-slip walls are used. Although flow features will shift with operation point, turbulence model, and rough vs. smooth walls, this grid convergence study should be sufficient to point out any major short-comings in spatial resolution.

3.2.1 Comparison of Overall Performance

An advantage of the Richardson Extrapolation is that it applies to both point-by-point solutions and solution functionals [42]. The convergence of the overall performance parameters total pressure and efficiency is evaluated in Figure 3.1 and Figure 3.2, and the grid convergence index for the fine and medium meshes are listed in Table 3.3. Note that the results are organized by normalized grid size h, where h has been previously defined in eqn. (3.1), and the normalization is simply dividing by h_{fine}.

Table 3.3 Grid Convergence Index (GCI) and apparent order of convergence for total performance parameters, total pressure ratio and adiabatic efficiency.

Performance parameter	Fine mesh, GCI_{21}	Medium mesh, GCI_{32}	Order of convergence
Bypass TPR	0.15%	0.21%	1.44
Core TPR	0.41%	0.76%	2.29
Bypass η	0.04%	0.17%	5.29
Bypass η	0.14%	0.36%	3.53

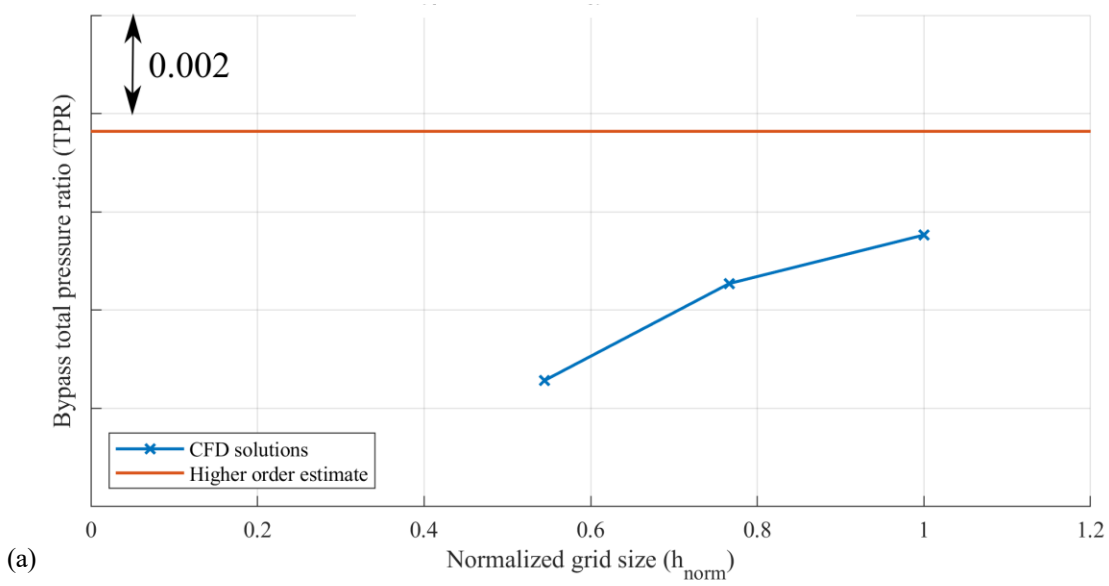

(a)

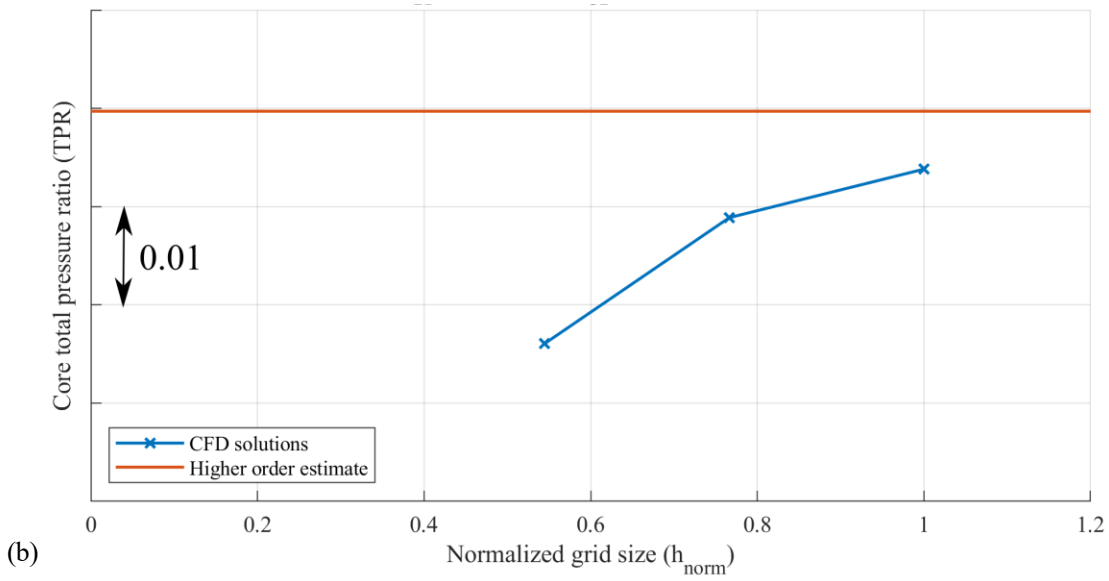

(b)

Figure 3.1 Total pressure ratio of (a) bypass flow and (b) core flow, with different levels of grid refinement.

Each increment on the y-axis of each plot in Figure 3.1 indicates a 0.002 increment of total pressure ratio for the bypass and a 0.01 increment for the core. The values of the total pressure ratios are on the order of 2, hence, the variations between values obtained between the different meshes are very small. From Table 3.3, the error estimate for total pressure ratio is under 0.5% for

the fine mesh and under 1% for the medium mesh, and the solutions appear to be monotonically converging with increased grid refinement. The apparent order of convergence for TPR of the bypass is under two, and for TPR of the core is over two, where two is the formal order of the solver. The apparent order may be under two, due to additional error from boundary conditions, etc.; or it may be over two, due to partial cancellation of spatial truncation errors.

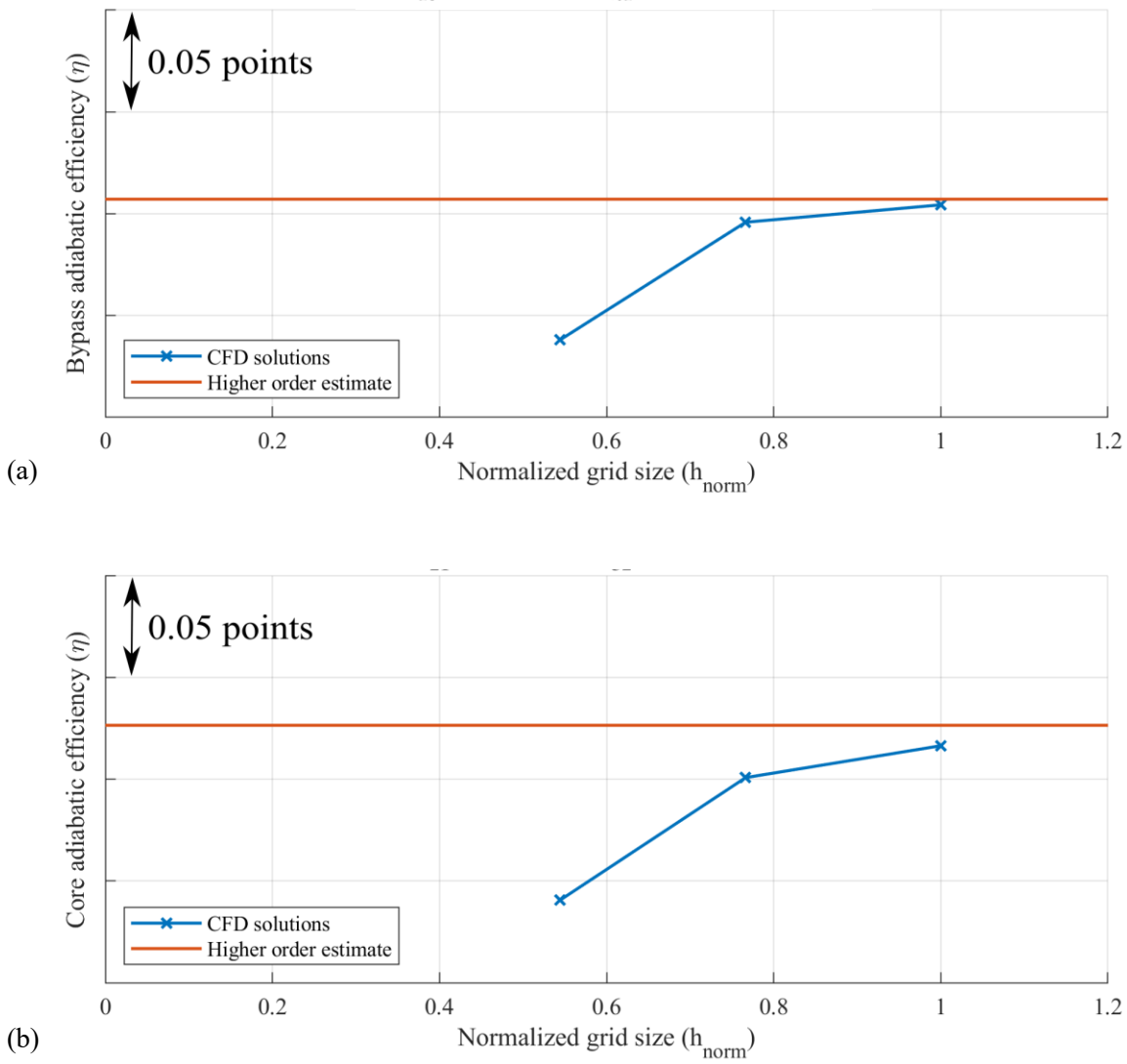

Figure 3.2 Adiabatic efficiency of (a) bypass flow and (b) core flow, with different levels of grid refinement.

Each increment on the y-axis of both plots in Figure 3.2 indicate 0.05-point increments of adiabatic efficiency. The discretization error estimates of adiabatic efficiency for both the fine and medium meshes are small – less than 0.2% for the fine mesh, and less than 0.5% for the medium mesh. Note that for both total pressure ratio and adiabatic efficiency, the core flow has greater discretization error than the bypass flow. This is likely due to increased spanwise spatial resolution near the rotor tip, applied to better resolve flow physics near the tip region.

Despite the low discretization error estimates obtained for the total pressure ratio and adiabatic efficiency, experimental values may not actually fall within the discretization error range. The total pressure ratio is heavily dependent upon prediction of the deviation angle at the trailing edge and, thus, may be difficult to predict [46]. The efficiency may also be offset as the loss of the tip flow is difficult to predict. In the AGARD blind study, the total pressure ratio was usually overpredicted for rotor 37 and the efficiency underpredicted [31].

3.2.2 Comparison of Flow Details

Although the overall performance parameters show small discretization error, it is important to check that the spatial discretization is adequate to qualitatively resolve flow details. The Grid Convergence Index method is applied locally to total pressure and total temperature ratios at the stator leading edge, using experimental rake locations. However, the local convergence may not be monotonic and thus meaning could be difficult to assign to the calculated discretization error; hence, other flow features are discussed qualitatively.

Stator Leading Edge Profiles

The total pressure ratio profile in front of the stator leading edge is shown in Figure 3.3 for 8 rake locations. The increase in loss in the tip region is shown in all three mesh solutions, and the shape of the curves match closely. Less tip loss is predicted by the coarser meshes, and more loss in the lower half of the span is predicted by the coarser meshes. Convergence does not appear to be monotonic, and there is also an increase in error around 70% span. The cause of this increase in error is unknown, as the refinement of both the rotor and stator is quite uniform from 40% to 80% span. The influence of the tip leakage vortex does not extend down to 70% span, and flow is completely subsonic with no discontinuities or singularities.

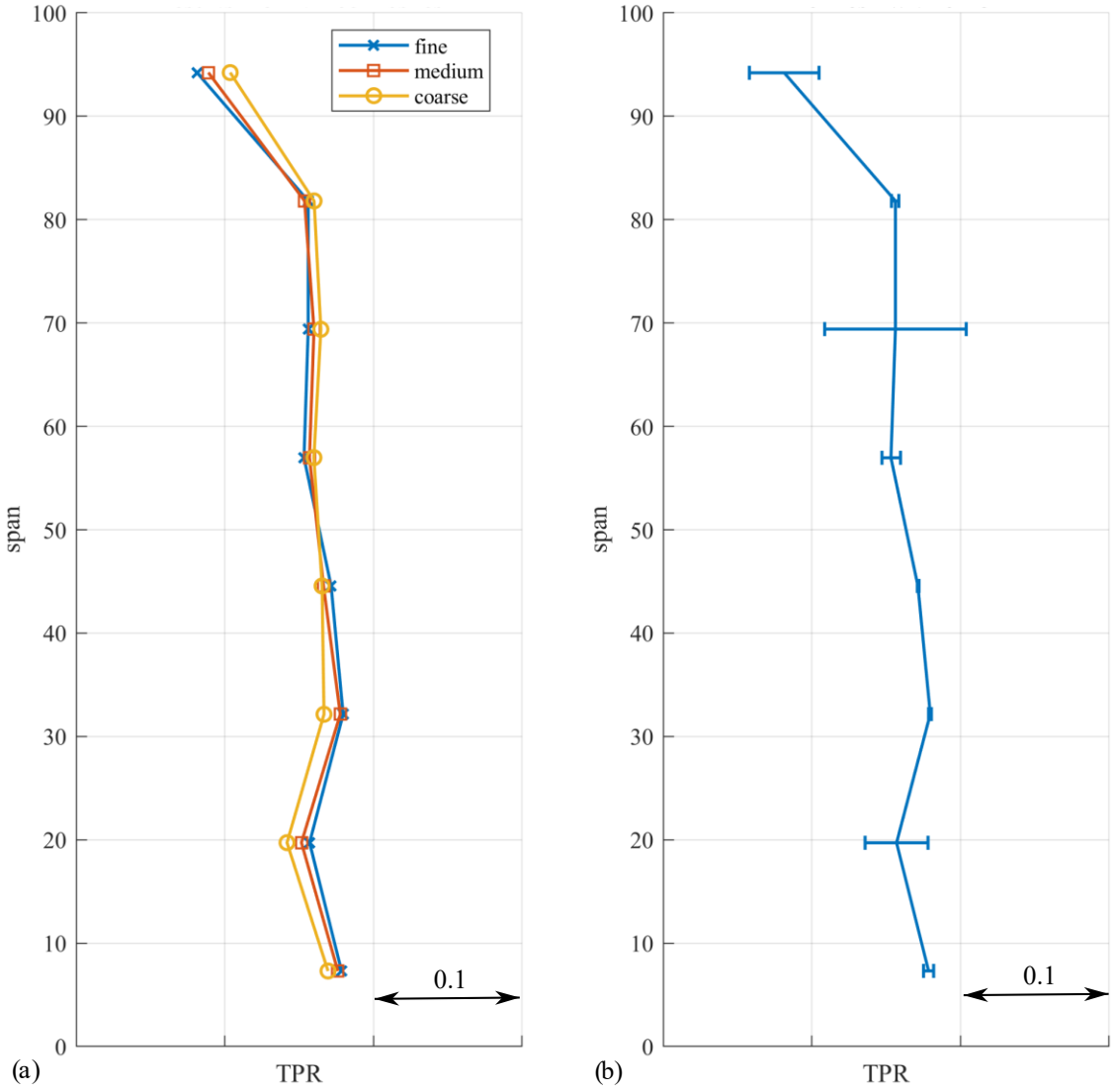

Figure 3.3 Total pressure ratio at leading edge of stator, with different levels of grid refinement; (a) solution from all three meshes, (b) fine mesh solution with error.

The total temperature profile is shown in Figure 3.4. The error for total temperature ratio is much smaller than for the total pressure ratio. More work is done in the tip region, and all three meshes predict the same work distribution, although the coarse mesh predicts slightly less work done at the tip region. This is reflected also in the bypass ratio from the three solutions. Despite having the same inlet and outlet boundary conditions, the bypass ratio is greater by 0.01 in the fine mesh compared to the coarse mesh. Hence, a slightly greater percentage of the flow is directed to the outer portions of the blade, and thus, slightly more work is done in the tip region.

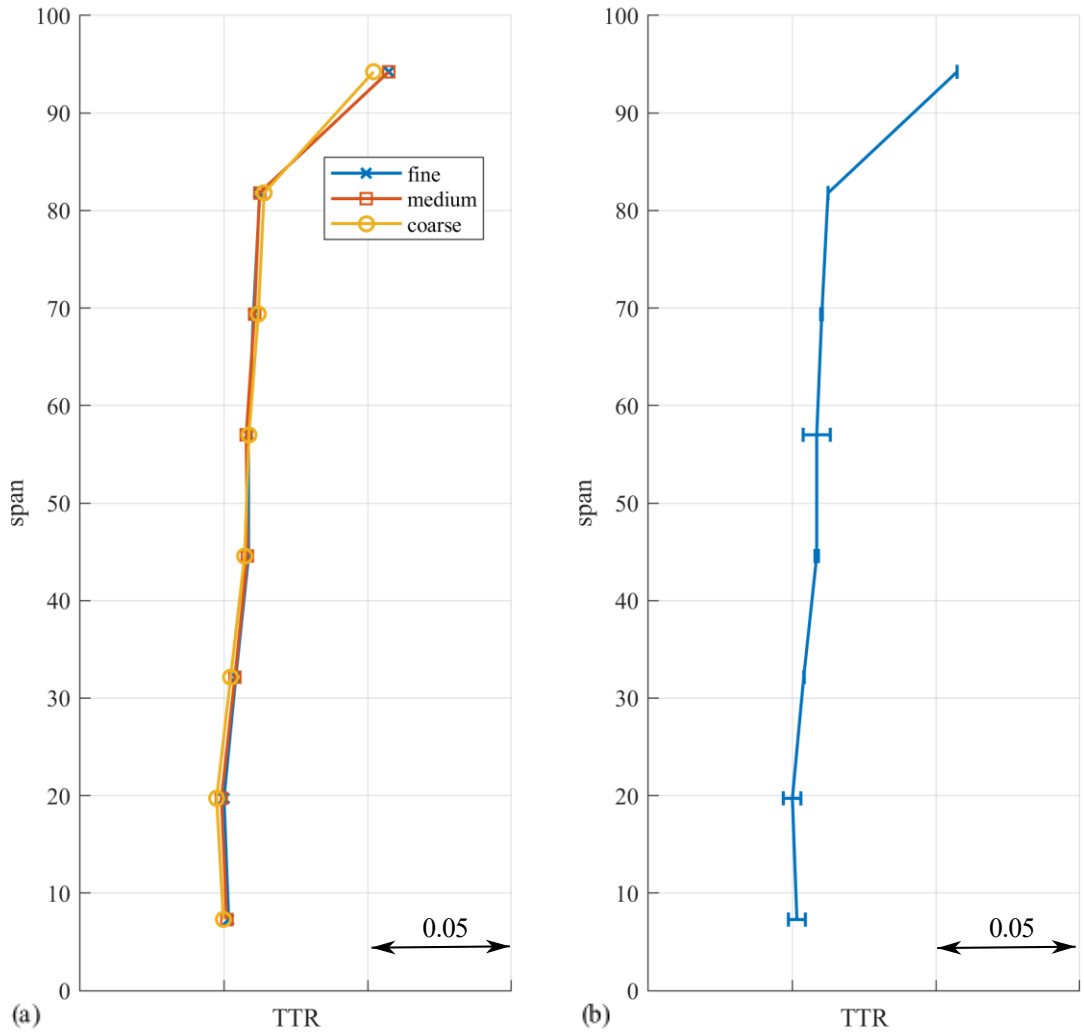

Figure 3.4 Total temperature ratio at leading edge of stator, with different levels of grid refinement; (a) solution from all three meshes, (b) fine mesh solution with error.

Shock Locations

Figure 3.5 shows the relative Mach number contours of the rotor at 90% span. At this operating point near the top of choke, the passage shock is started. The passage shock intersects the weak bow shock that extends from the pressure side leading edge, and ends in a lambda foot on the suction side of the adjacent blade. Behind the shock, the suction surface boundary layer thickens and separates, while the pressure surface boundary layer stays attached. Streamwise plots and circumferential plots of relative Mach number at constant span are shown in Figure 3.6 and Figure 3.7 to compare shock locations and shock strength. The streamwise locations used for

Figure 3.6 are labelled in Figure 3.5 as p20 and p50, indicating a pitchwise location of 20% and 50% from the suction side of the rotor, respectively. The chordwise location used for the circumferential plots in Figure 3.7 is labelled in Figure 3.5 as c20, indicating a chordwise location of 20% rotor chord.

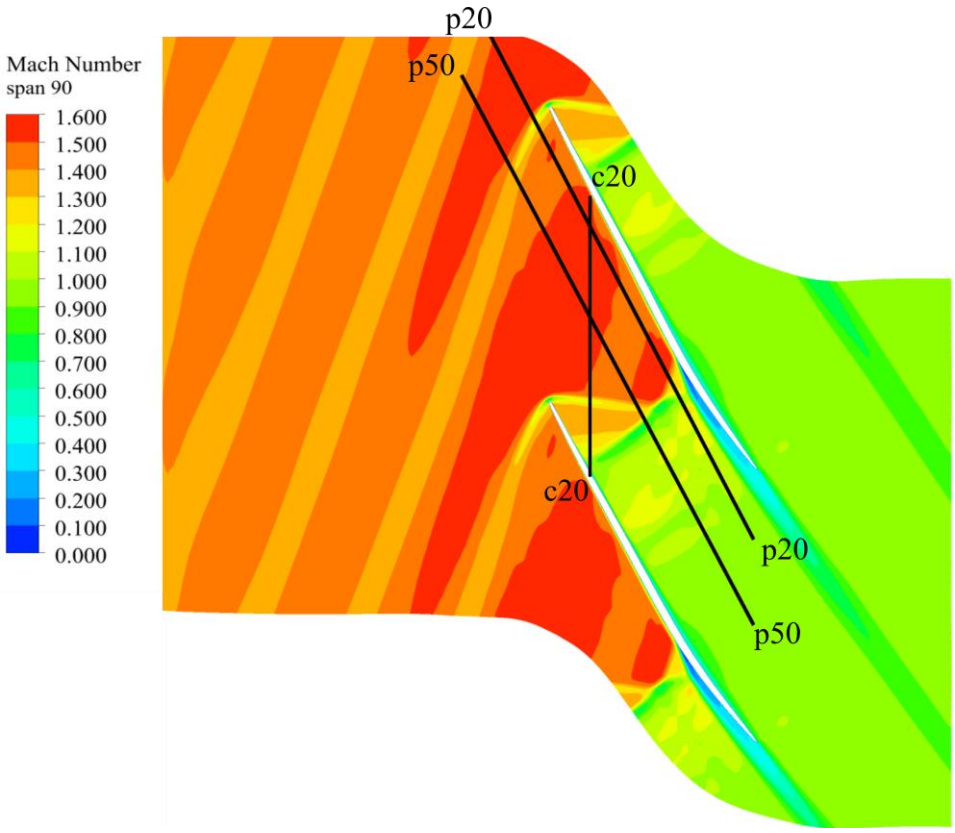

Figure 3.5 Relative Mach number at 90% span, fine mesh solution. (Image skewed)

Let the shock location be defined as where the Mach number first starts to decrease. Observing Figure 3.6, the location of the bow shock is indicated by the first large dip in Mach number right in front of the leading edge. All three meshes agree on the location of the dip, although the coarse mesh seems to smear out the sharp gradient. Prior to the bow shock, there are flow perturbations from the bow shock of adjacent blades extending upstream. Although the inflow matches quite well for 95% span and 60% span, at 90% span this upstream perturbation is more diffused in the coarse mesh case. Behind the bow shock, the flow is accelerated, and all three meshes agree on the Mach number after acceleration. Then, the next large drop in Mach number

occurs, indicating the passage shock. From all three spanwise locations, the coarse mesh appears to predict a slightly earlier start of this shock; additionally, the location of the subsequent small peaks and dips that indicate the lambda foot of the passage shock are more diffuse for the coarse mesh, showing an increase in shock smearing. Note that the coarse mesh also overpredicts the Mach number further downstream of the passage shock at 95% span. This difference in Mach number further downstream is reduced away from the shroud and barely noticeable at 60% span. Despite all these differences, the general trends are the same for all three meshes.

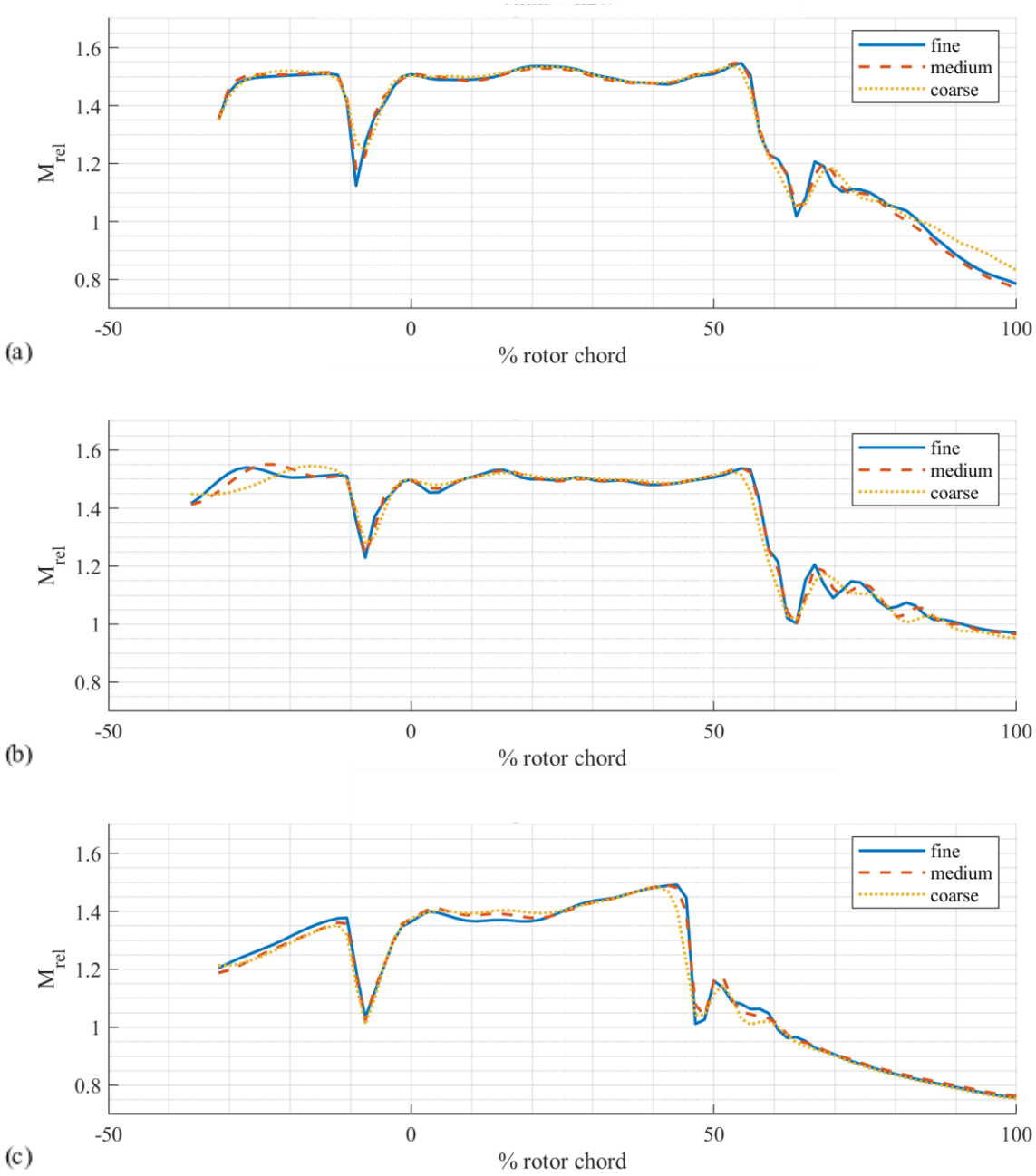

Figure 3.6 Relative Mach number in streamwise direction, at 20% pitch from suction side. Spanwise locations of (a) 95% span, (b) 90% span, and (c) 60% span. Abscissa location 0% rotor chord indicates start of the rotor passage, and 100% indicates the exit.

Figure 3.7 shows the blade-to-blade Mach number at 90% span. Pitch of 0% is the suction side of the blade, and 100% is the pressure side of the adjacent blade. At 20% chord, the sharp drops in Mach number near the suction blade surface give a rough idea of the boundary layer

thickness prior to the passage shock, and all three meshes agree well. However, the Mach number dips at 20% chord near the pressure side (which indicate the partially merged bow shock and the lambda foot of the passage shock) show that the coarse mesh smears the shock. Moving to 90% chord, the Mach number drop near the suction surface shows the blade-to-blade extent of the low momentum radial flow behind the passage shock; all three meshes agree very well.

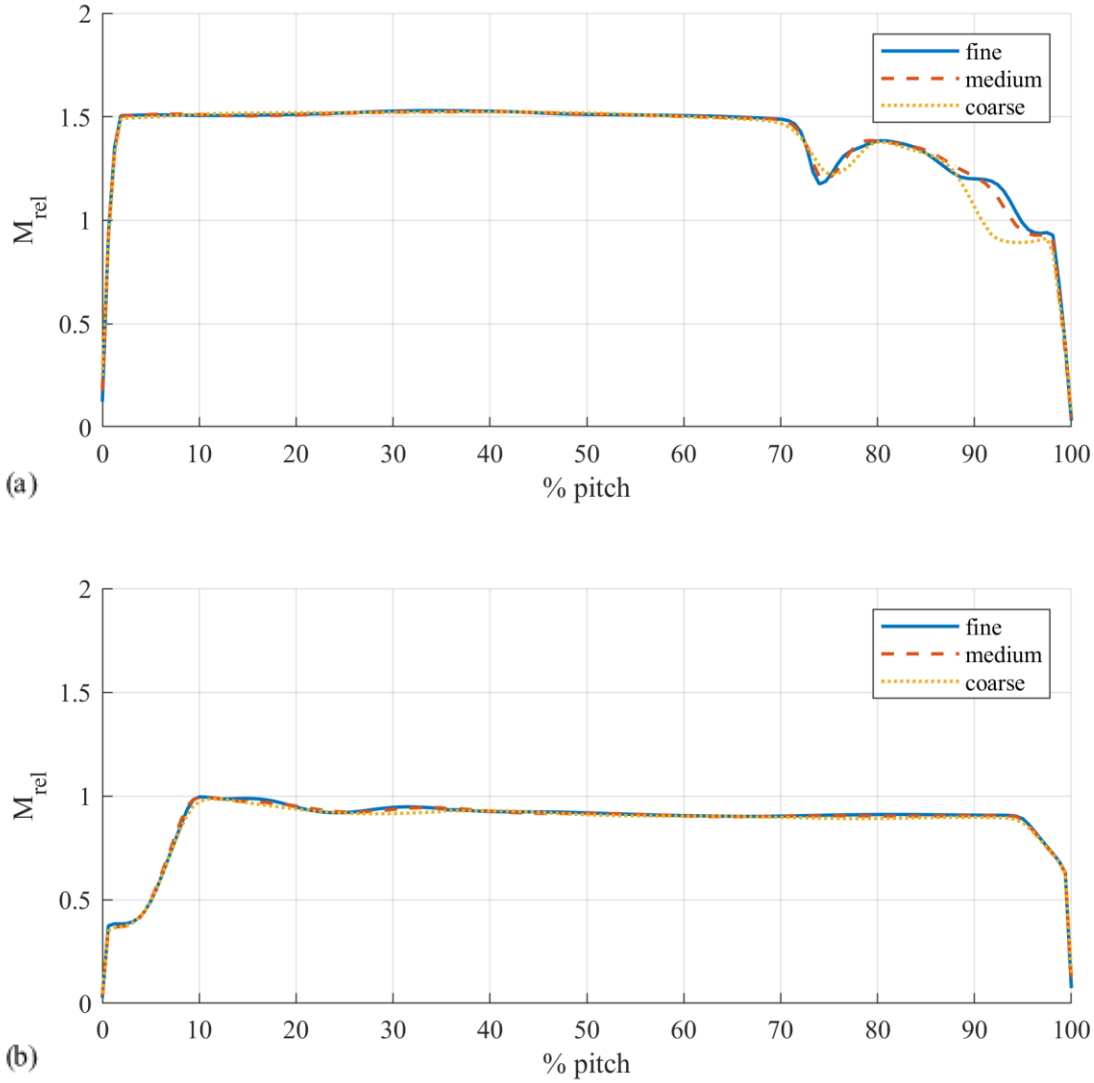

Figure 3.7 Relative Mach number in circumferential direction, at 90% span. Axial locations of (a) 20% rotor chord, and (b) 90% chord. Location 0% pitch indicates suction side, and 100% indicates pressure side of the adjacent blade.

Tip Leakage Flow

A decent approximation of the mass flow rate through the tip gap is sufficient to give a reasonable estimate of the interaction between the tip leakage flow and the primary flow [21]. The mass flow rate through the tip gap, divided into 10% chord increments and normalized by the inlet mass flow, has been graphed in Figure 3.9. The passage shock ends on the pressure surface at around 10% chord; the increase in mass flow rate of the 10% to 20% chord segment reflects the large pressure difference across the rotor tip, increased by the shock. Note that near the leading edge, the coarse mesh tends to overpredict the mass flow rate through the gap while, for the rest of the rotor tip, this flow is underpredicted. This is likely due to a slight difference in pressure distribution at the rotor tip, from a small difference in prediction of Mach number behind the shock.

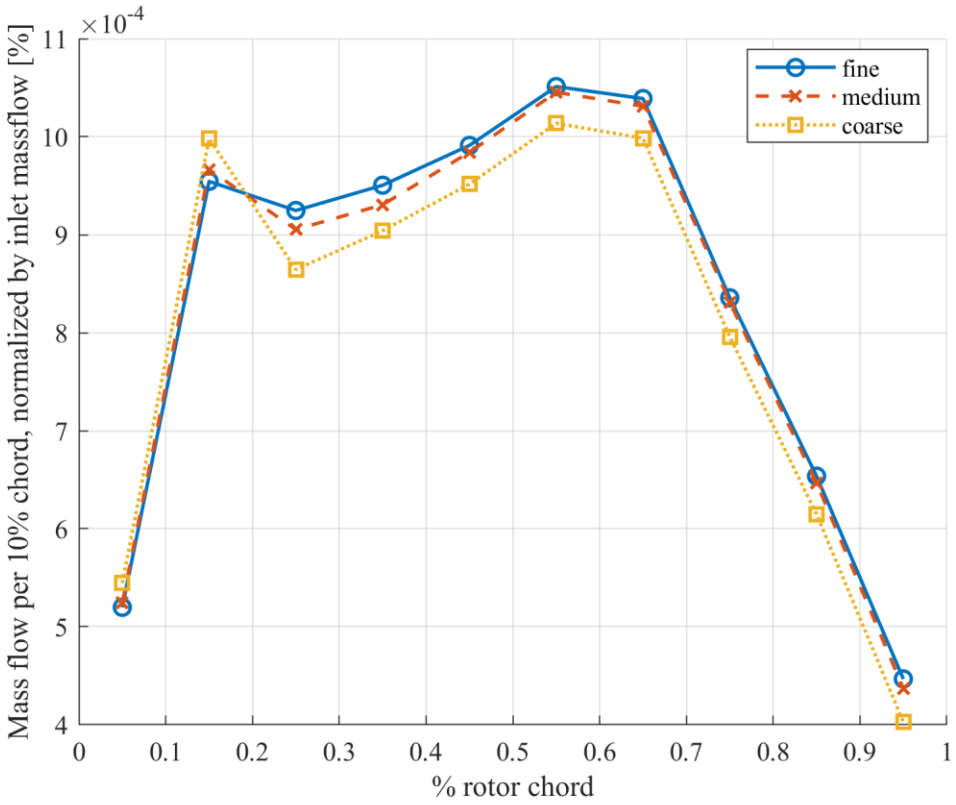

Figure 3.8 Normalized mass flow through the rotor tip, calculated across every 10% chord.

The strong tip leakage vortex starts at the leading edge for all three meshes, and there was no visually distinguishable difference in their trajectories.

Rotor Wake

The width and depth of the rotor wake is an indicator of flow mixing and loss. Grids that are not flow-aligned or are too coarse may smear gradients in the wake. From Figure 3.8, at 0.3 rotor chords downstream of the trailing edge, the deficit of the wake at the rotor tip shows that the tip loss is very large, and the depth of this deficit is underpredicted by the coarse mesh. The width of the wake is slightly larger for the coarse mesh, showing increased mixing. The largest discrepancies between the different mesh discretizations happen near the tip, where secondary flow effects are strong; the radial extent of the tip leakage flow for the solution at this operation point reaches 95% span. Since all three meshes have the same topology, the degree of flow alignment is very similar between the three. Note that the degree of wake mixing depends on both the mesh discretization and turbulence model parameters. Denton [46] observed that flow-aligned grids in the AGARD blind study tended to overpredict the wake depth, possibly because the real wake includes an unsteady vortex sheet, which increases the flow mixing.

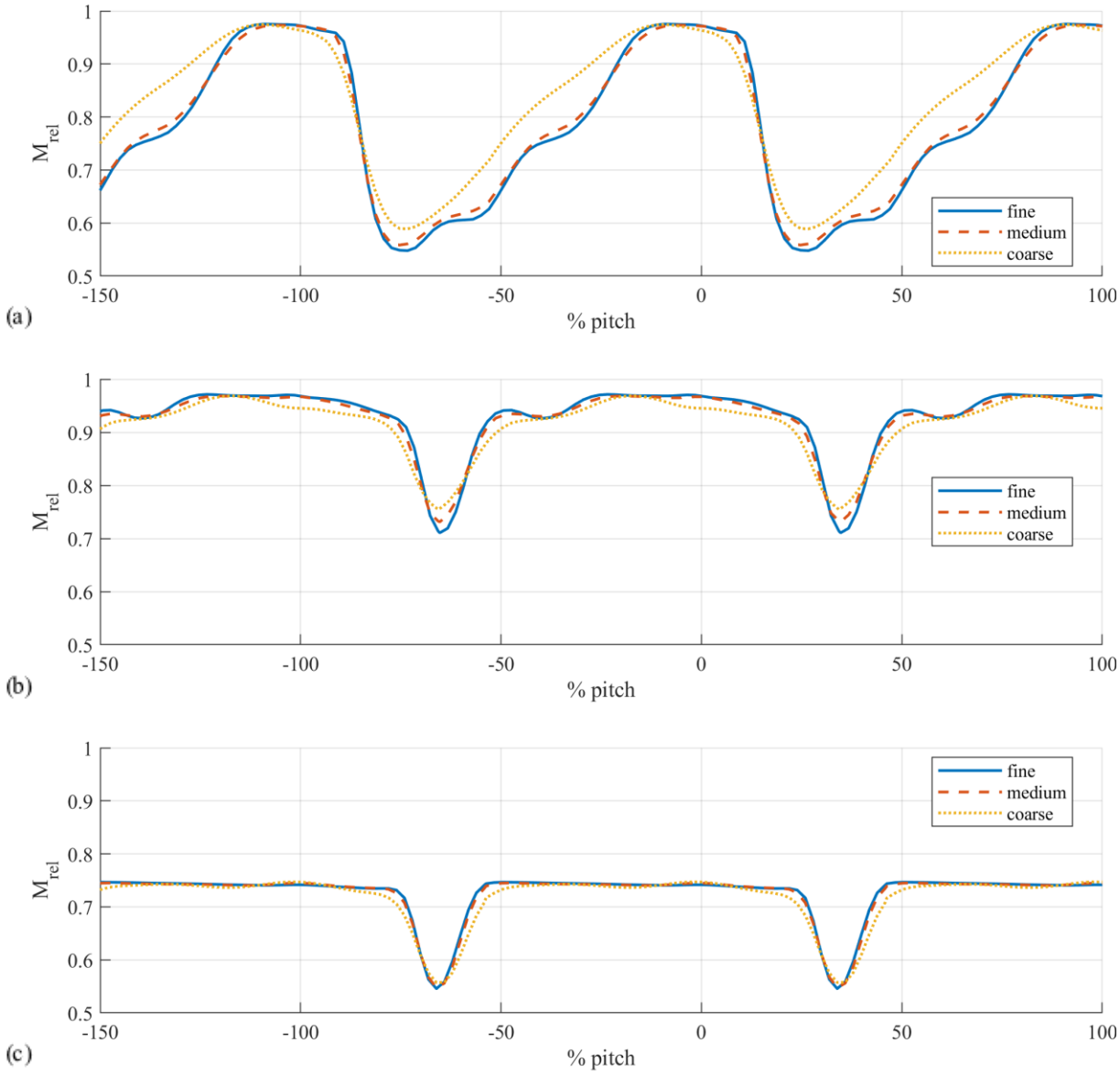

Figure 3.9 Relative Mach number in circumferential direction, 0.3 rotor chords downstream of the rotor trailing edge. Spanwise locations of (a) 95% span, (b) 90% span, and (c) 50% span.

3.2.3 Comparison of Computational Time

Mesh refinement is costly in that each iteration will take longer for a finer mesh, and it will take more iterations for a finer mesh to reach convergence. For the current grid convergence study, the comparison of computational time is listed in Table 3.4. The normalized time per iteration is the average of the last 100 converged iterations, normalized by the time per iteration of the coarse mesh. The approximate number of iterations to convergence is the earliest that the solution looks

converged, using the steady convergence criteria in section 3.1. Note that initial solution used to start each run is the converged lower order solution (with an upwind advection scheme and first order turbulence numerics), using the same operating point and mesh.

Table 3.4 Comparison of computational time between different meshes from GCI study.

	Fine mesh	Medium mesh	Coarse mesh
Normalized time per iteration	6.73	2.83	1
Approximate number of iterations to convergence	5000	3500	2200

From previous comparisons of flow features, the difference between the fine and medium mesh solutions seem to be small, and the error on the medium mesh from the grid convergence study is small. However, the increase in computational cost from medium to fine more than doubles. The coarse mesh also captures the flow qualitatively, but there is some smearing of flow features. Hence, the medium mesh has been used for the following steady simulations.

3.3 Speedline at 100% Speed

The purpose of this section is to compare flow features at different loading conditions for design speed operation to obtain a better understanding of the flow field in this fan.

Points on a 100% speedline were found using the medium mesh, with SST (with curvature correction) as the turbulence model. To traverse the speedline, the mass flow rate was varied at the core exit, while average static pressure was varied at the bypass exit; the bypass ratio was kept constant within ~1% of nominal bypass ratio for all operating points. Due to stability problems, these exit boundary conditions could not be used for the near stall point; this is discussed in a later section. The current configuration has a tip clearance of 0.29% (clearance-to-tip chord ratio). This is a tight clearance and falls within a range representative of modern fans [14].

3.3.1 Overall Performance

The total pressure ratios for the bypass and core flows are shown in Figure 3.10, and the adiabatic efficiencies are given in Figure 3.11. Using these two figures, three operation points are

chosen for the comparison of flow details; they are labelled in Figure 3.11. These three points have distinct flow structures: one point near stall, one point near peak efficiency, and one point in choke.

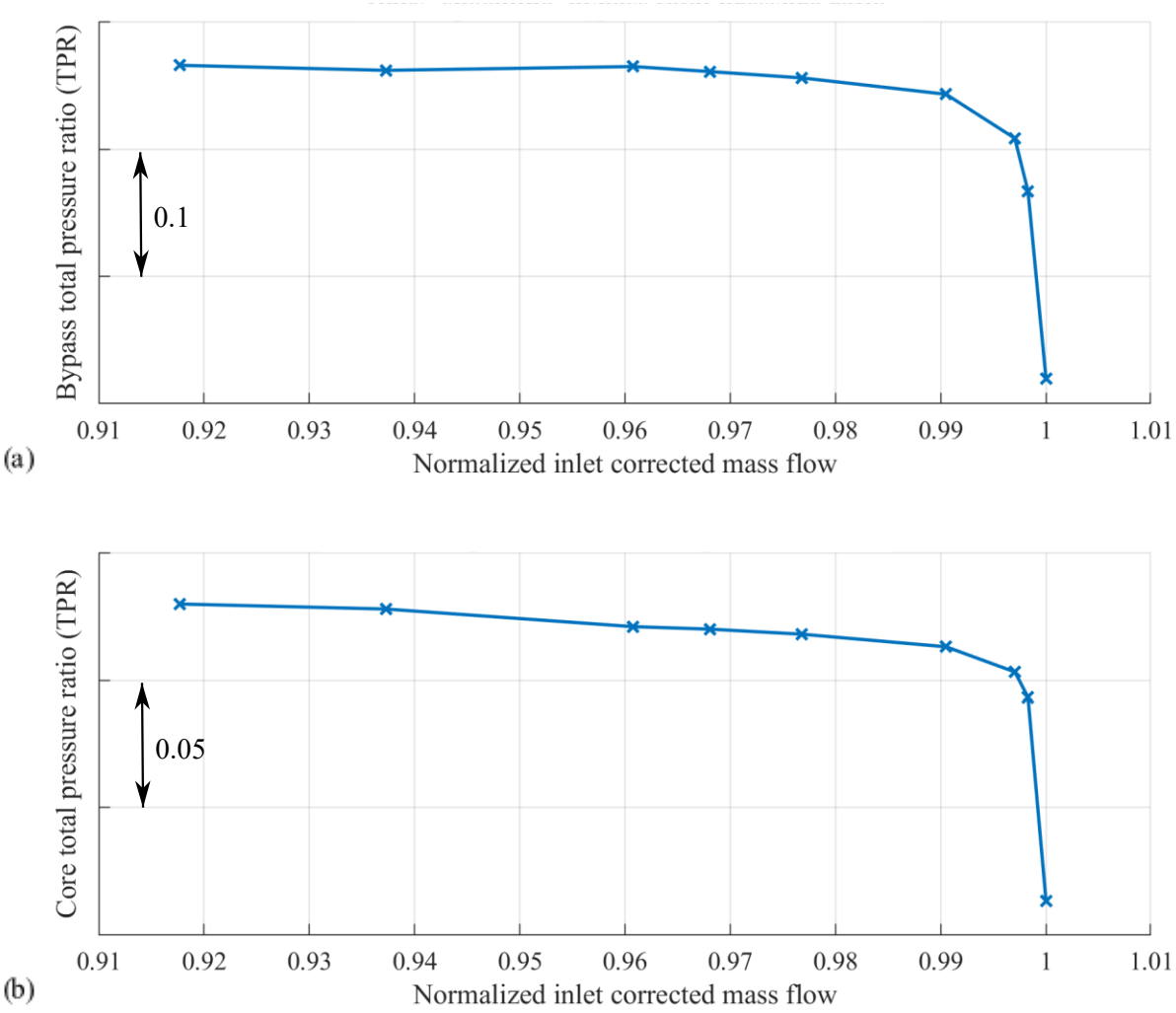

Figure 3.10 Speedline at 100% design speed, total pressure ratios for (a) bypass flow, and (b) core flow. Inlet corrected mass flow normalized by choke mass flow.

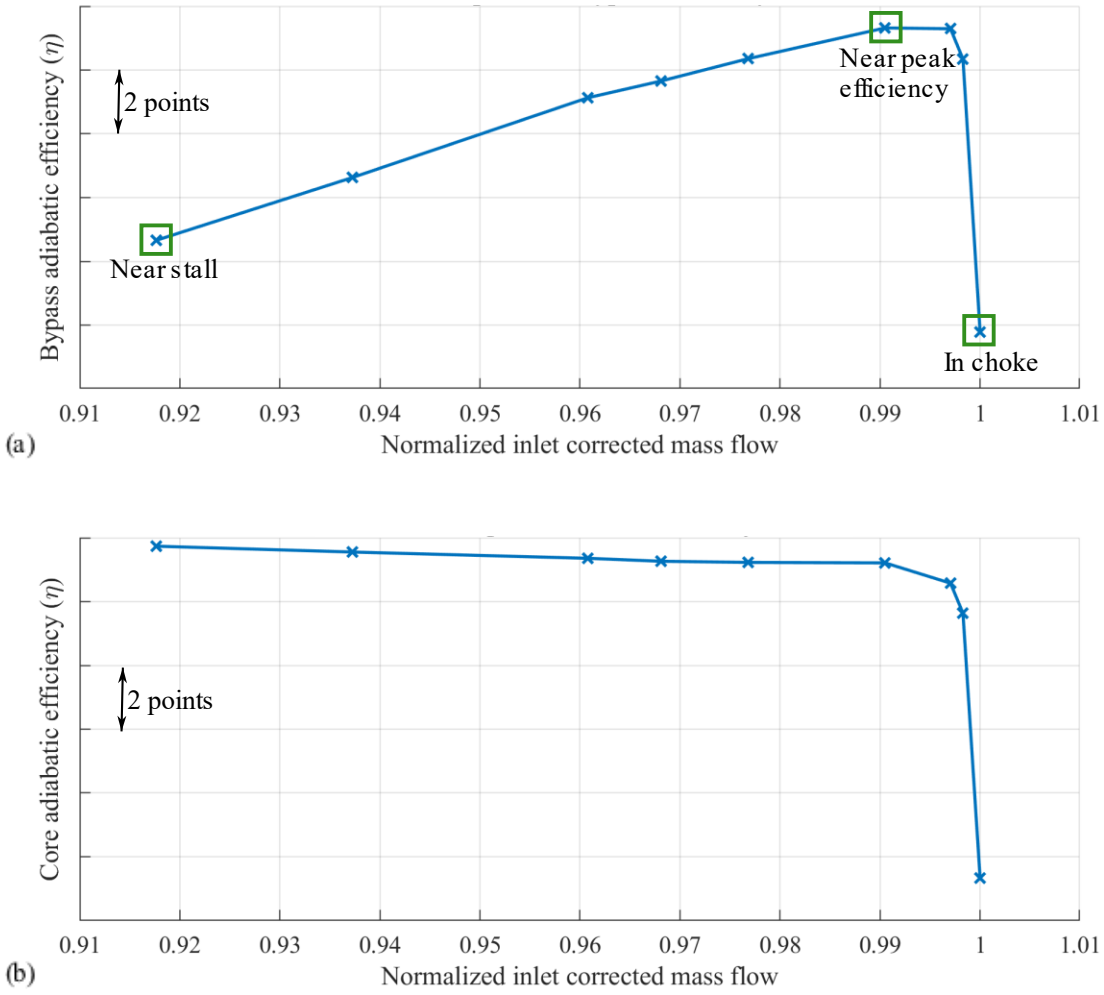

Figure 3.11 Speedline at 100% design speed, adiabatic efficiencies for (a) bypass flow, and (b) core flow. Inlet corrected mass flow normalized by choke mass flow. The three points chosen for comparisons are highlighted.

3.3.2 Comparison of Local Flow Features

The focus of the comparison between the different operation points is to observe how specific flow features such as the shock, the TLF, and their interaction change as the loading changes.

Stator Leading Edge Profiles

In Figure 3.12 and Figure 3.13, the total pressure ratio and total temperature ratio distribution at the stator leading edge rake locations have been graphed, respectively. The resulting trend of high total temperature ratio near stall was expected since the most work is done near stall, but there may also be increased loss from the passage shock forming a stronger oblique shock in-front of the rotor. Indicated by low total pressure ratio, choke may have increased loss from the passage shock, due to the shock being further inside the rotor passage and thus not giving enough time for the separated suction side boundary layer behind the shock to reattach. The spanwise sweep of total pressure ratio and total temperature ratio may suggest the importance of supersonic diffusion at different spans. The strength and configuration of the passage shock is most affected by the change in loading, while in the subsonic region near the hub, the mechanism of diffusion through turning the flow stays the same. This is also reflected in the spanwise efficiency distribution in Figure 3.14, as the efficiency of variation near the shroud is significantly greater than the variation near the hub.

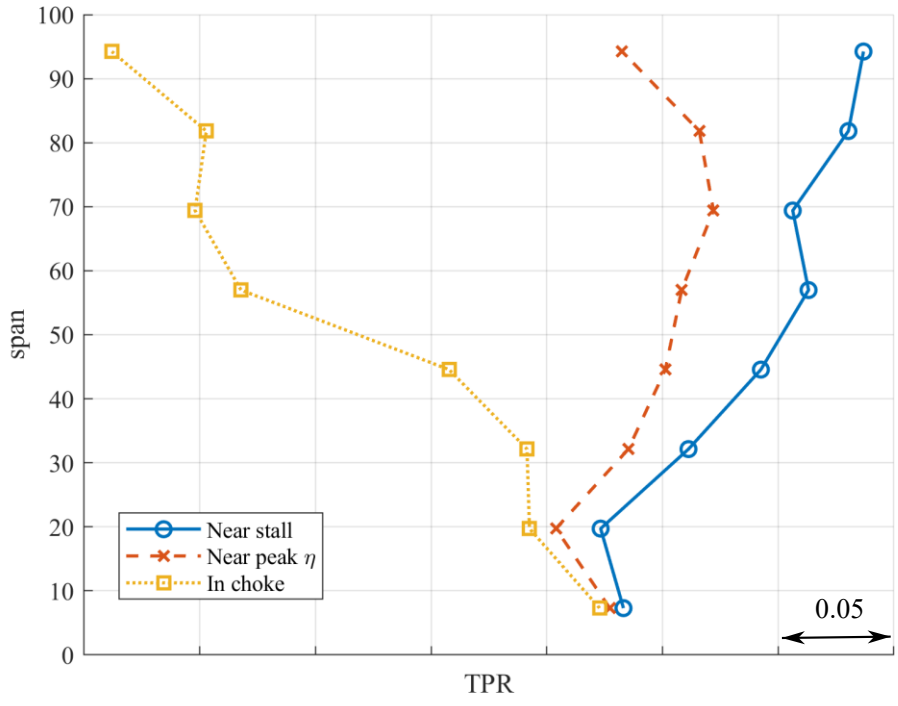

Figure 3.12 Total pressure ratio at leading edge of stator, at different loading conditions.

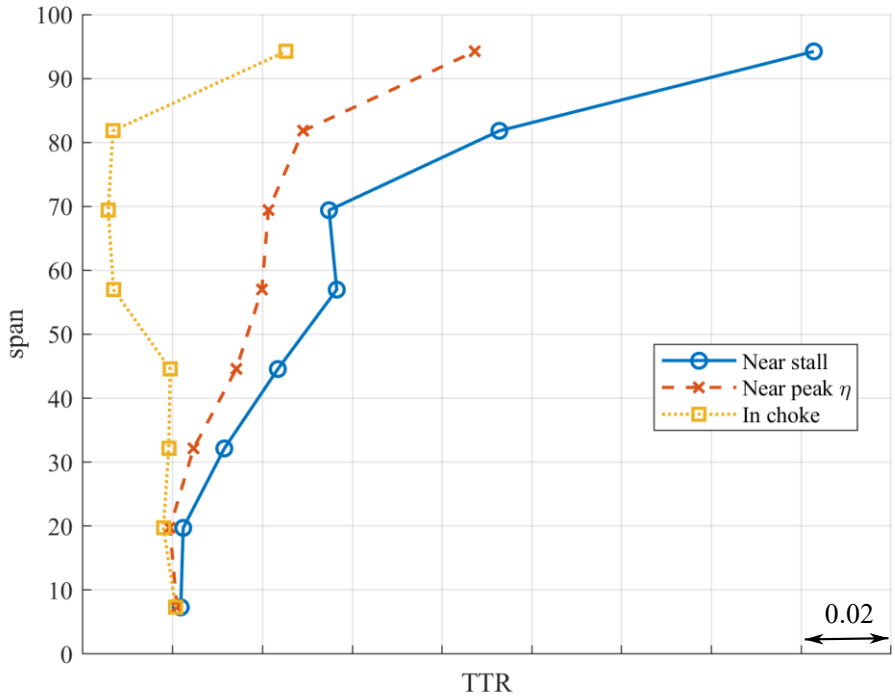

Figure 3.13 Total temperature ratio at leading edge of stator, at different loading conditions.

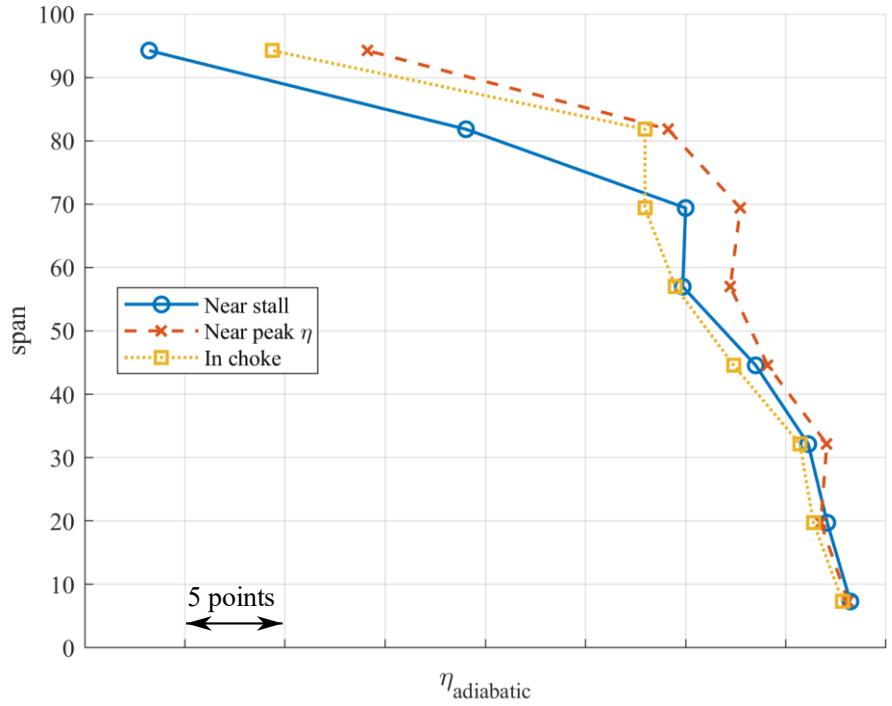

Figure 3.14 Adiabatic efficiency at leading edge of stator, at different loading conditions.

Shock Locations

The differences in shock structure are observed in the relative Mach number contours at 90% span in Figure 3.15. At the near stall operating condition, there is a strong shock that stands outside the rotor passage; this flow is in an unstarted configuration. Near peak efficiency, there is also one shock, however, this shock is in the rotor passage. From the jump in Mach number, the shock at peak efficiency is weaker. Additionally, the blockage created by the suction surface boundary layer separation behind the shock is much smaller, as indicated by the blue low Mach number region. In choke, there is a system of oblique shocks inside the rotor passage, which impinge on the suction surface close to the trailing edge, and does not leave much chord left for the boundary layer to reattach. The details of the flow are further discussed using streamwise plots of the relative Mach numbers in Figure 3.16.

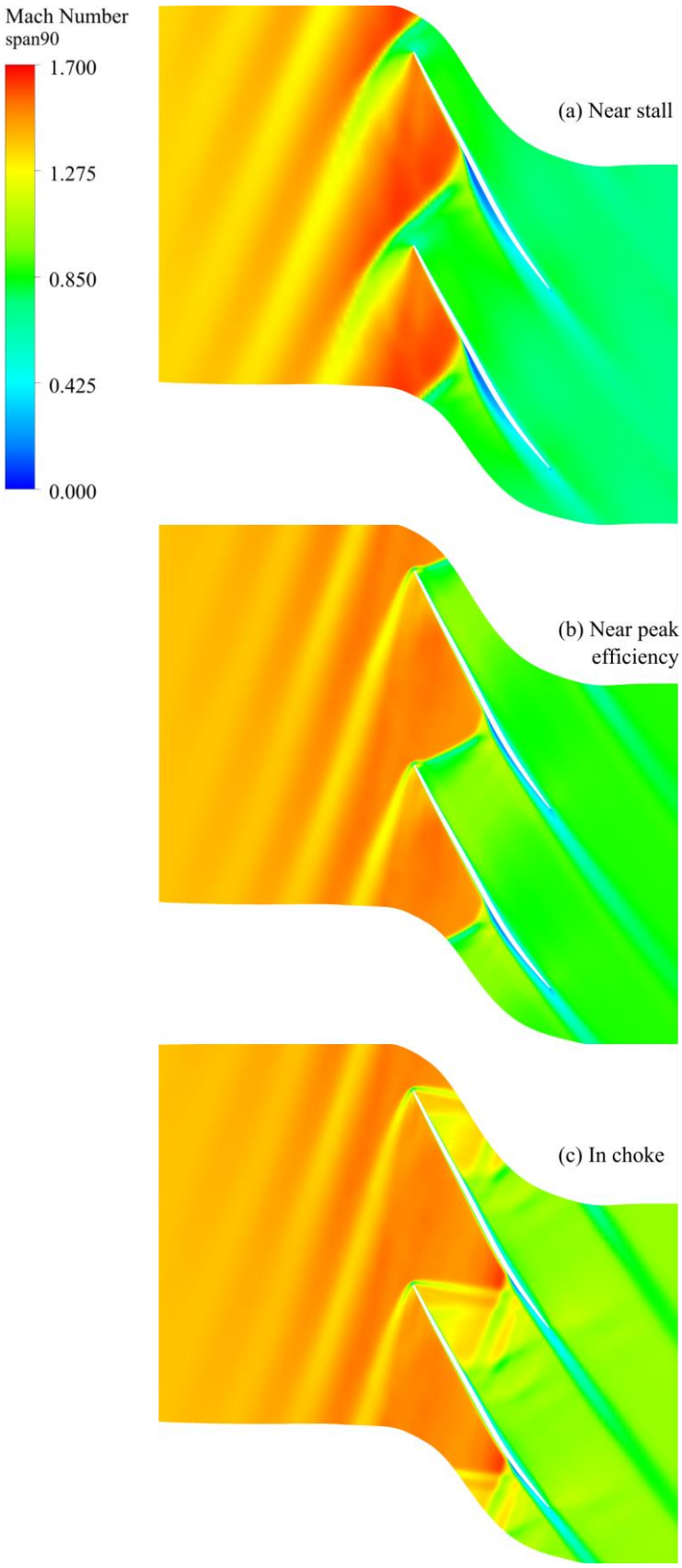

Figure 3.15 Relative Mach number in rotor passage at 90% span.

Figure 3.16 shows a streamwise plot of the relative Mach number 20% of the blade passage away from the suction surface. A chord location of 0% indicates the rotor leading edge inlet plane, and 100% indicates the rotor trailing edge exit plane. Right before 0% chord, the bow shock from the adjacent blade is visible through the dip in Mach number. The change in the bow shock stand-off distance from the rotor leading edge across different loading is not obvious between the choke and peak efficiency operation conditions at lower spans. However, at 95% span, the peak efficiency bow shock is stronger than the choke bow shock. For these two operating points, the flow is in a started configuration, and the bow shock is close to the rotor leading edge. For the near stall condition, the passage shock has moved in-front of the rotor and has merged with the bow shock; this shock is stronger and further from the leading edge.

Observing the Mach number increase between the bow shock of the adjacent blade and passage shock, the flow is sped up again along the suction surface in-between the shocks. The pre-shock Mach number of the passage shock appears quite similar near the suction surface for all three loading conditions, despite a large difference in passage shock location. This can be attributed to the camber of the blade being small or negative near the rotor tip – the flow does not accelerate further when given more distance along the suction surface. Despite the similar pre-shock Mach numbers, the passage shock is stronger with higher loading. Although this plot is only for one pitchwise location, shock losses appear to be the smallest for choke and greatest for near stall. Hence, the large efficiency drops in choke are likely not directly due to shock loss.

The change in spanwise sweep of the passage shock at different loadings is also shown in Figure 3.16. At the near stall condition, the passage shock falls within 25% to 30% chord near the suction surface, indicating little spanwise sweep. For near peak efficiency and choke operation, the obliquity of the shock surface is evident – the shock sweeps backwards from 60% span to 95% span by as much as 25% chords for choke. This matches with the expectation that the shock surface becomes more planar near stall. Note that the passage shock is expected to become stronger with increasing span. This increase in shock strength near the rotor tip is clear for the near stall case, but less so in the peak efficiency and choke cases. Recalling that the shock generally becomes stronger as it moves forward in the passage, this lack of increase in shock strength can be attributed to the sweep of the shock in the peak efficiency and choke cases.

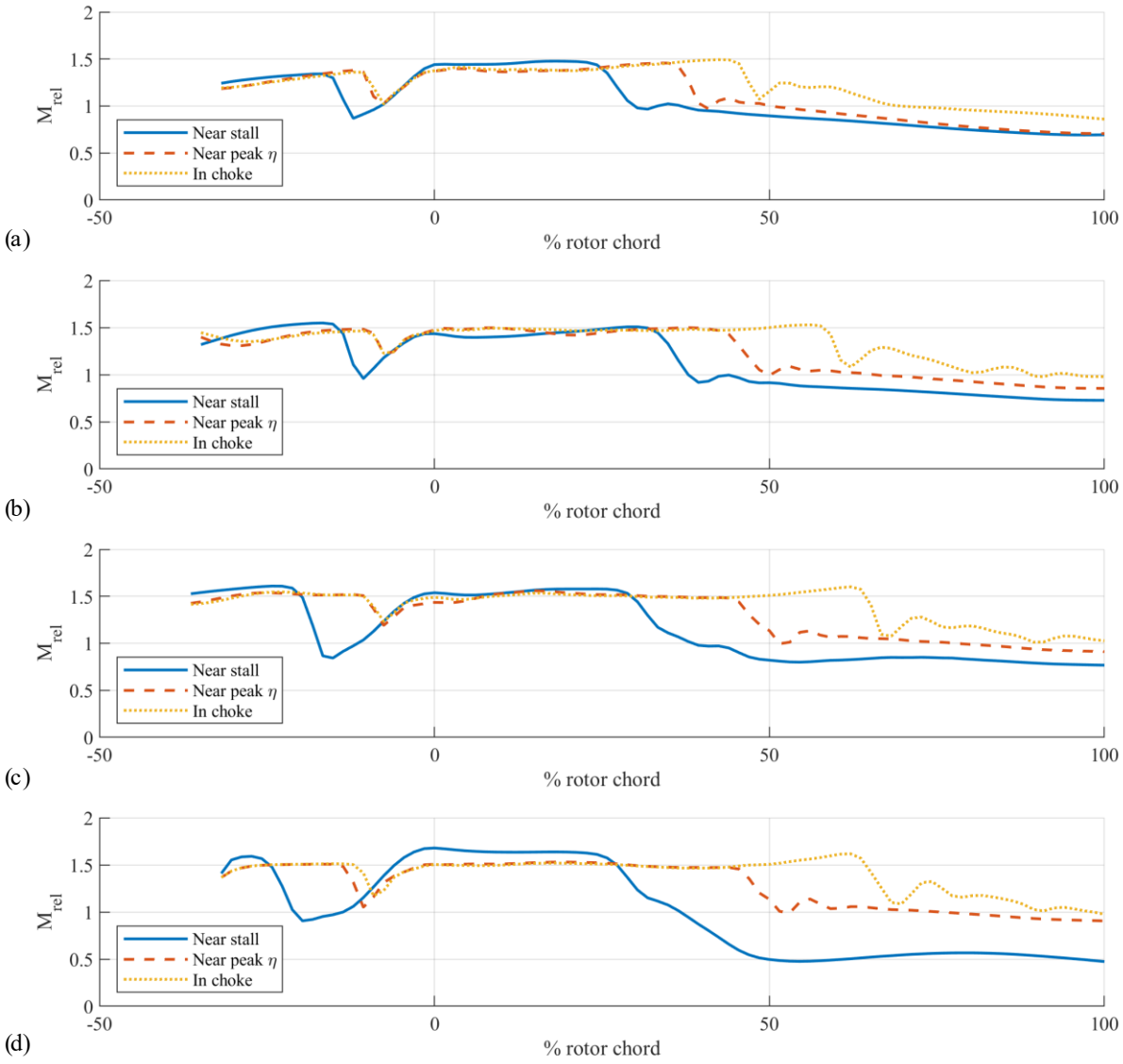

Figure 3.16 Relative Mach number in streamwise direction, at 20% pitch from suction side for (a) 60% span, (b) 80% span, (c) 90% span, and (d) 95% span. At different loading conditions.

In Figure 3.17, the relative Mach numbers at 90% span across the blade passage show the difference in suction surface separation across the different loadings. The suction surface of one blade is at 0% pitch, and the pressure surface of the next blade is at 100% pitch.

At 10% chord, the suction surface boundary layer is not separated as the passage shock has not yet impinged on the surface. A detailed view of the profiles near the suction surface and pressure surface is shown in Figure 3.18. If the sharp decrease of Mach number near the blade

surfaces is taken as an indication of blockage due to the boundary layer, all three loadings have similar boundary layer thicknesses. On the pressure side, the shock starts near the leading edge and the crossing of the shock in the passage can be observed.

At 40% chord, the overall Mach number drop in the near stall condition shows that the flow here is behind the passage shock, and the low Mach number region near the suction surface suggests boundary layer has thickened or separated. Comparing with Figure 3.15, the boundary layer separation will continue to grow for the near stall condition. The shock has not yet reached the suction side for the peak efficiency and choke conditions, but the blockage from the suction surface boundary layer has increased; this is likely due to adverse pressure gradients.

At 60% chord, the flow is behind the passage shock for peak efficiency condition, and the extent of the blockage created by the radial/separated flow behind the shock has increased for the near stall condition. The crossing of oblique shocks can be observed for choke at this axial location, and there appears to be two distinct oblique shocks.

At 90% chord, the flow near the suction surface is behind a shock or shock system for all three operating conditions, and there is a low Mach number region near the suction surface for all three flows. The difference in Mach number between this low Mach region and the freestream is especially high for the choke condition. At this location, the blockage created by the separated/radial flow seems to be the smallest for peak efficiency.

Note that the blockage due to the boundary layer on the pressure side also increases through the rotor passage. Comparing the pressure side blockage and the suction side blockage before the shock impinges on the suction side, the growth of the pressure side boundary layer seems to be more aggressive. This is likely because, in addition to an adverse pressure gradient, the curvature of the blade pressure surface also destabilizes the flow.

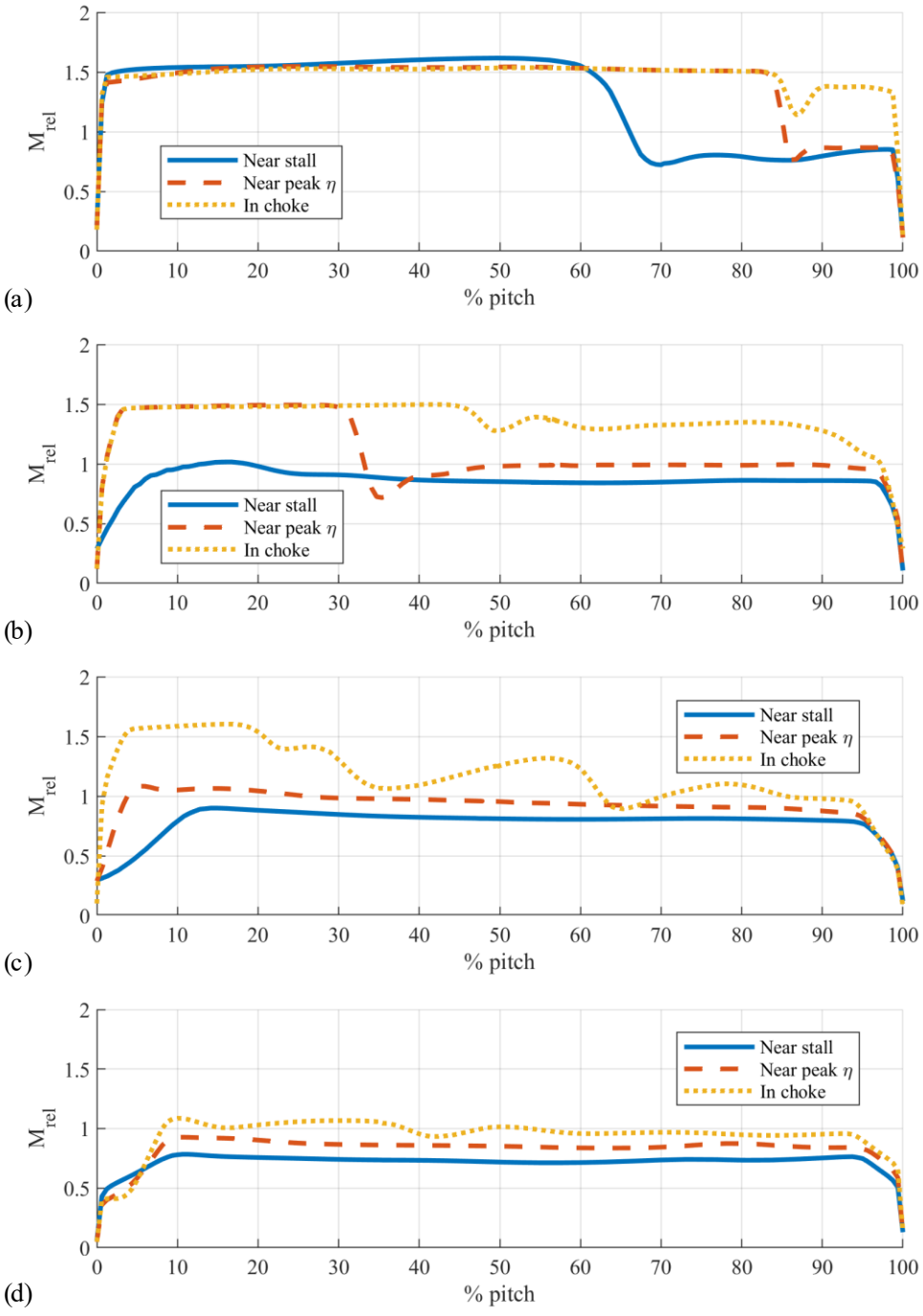

Figure 3.17 Relative Mach number in circumferential direction, at 90% span for (a) 10% chord, (b) 40% chord, (c) 60% chord, and (d) 90% chord. Location 0% pitch indicates suction side, and 100% indicates pressure side of the adjacent blade.

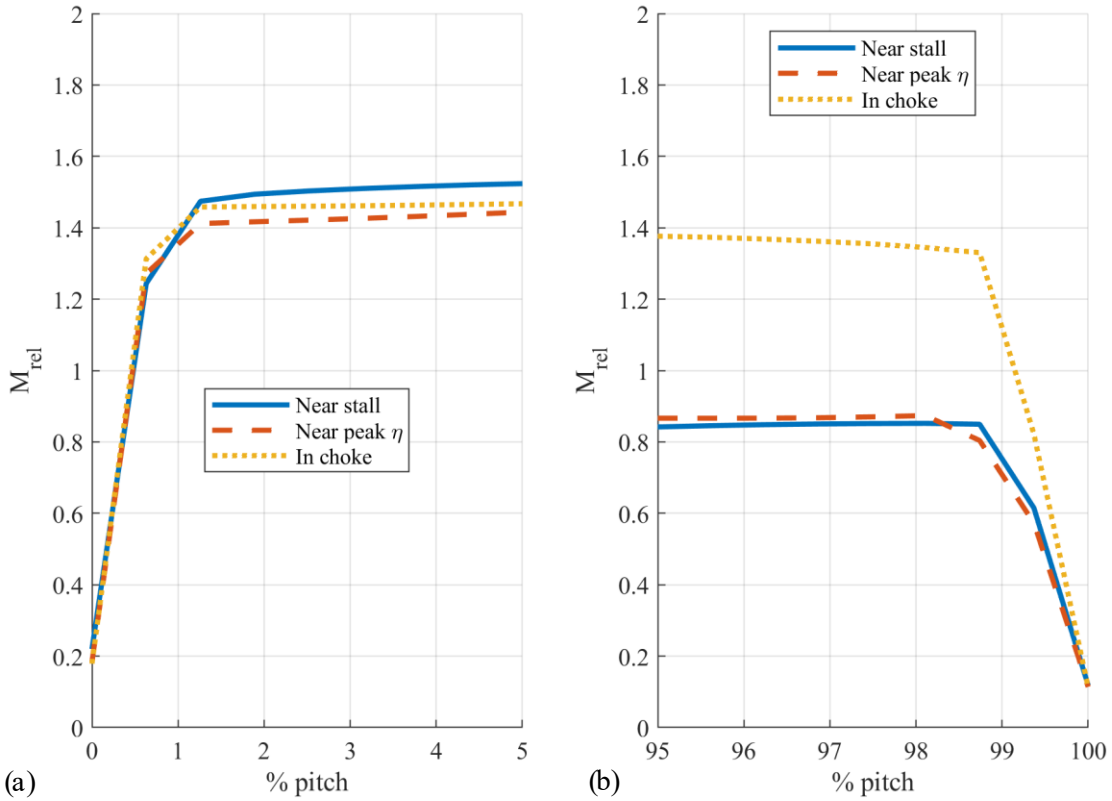

Figure 3.18 Detail of relative Mach number in circumferential direction at 90% span and 10% chord. For (a) near the suction surface, and (b) near the pressure surface.

Tip Leakage Flow and Shock-Vortex Interaction

The mass flow rate through the rotor tip at different operating conditions, normalized by inlet mass flow, is shown in Figure 3.19. The tip flow distribution is influenced by the pressure difference across the rotor tip as shown in Figure 3.20, which is in turn affected by the shock locations. Hence, it is expected that the near stall point has most of the tip leakage flow near the leading edge, and that the peak of the flow distribution moves down the chord with decreased loading. It is interesting to note that there is more leakage flow in the first 10% of the rotor for peak efficiency, compared to near stall, since pressure gradients across the rotor tip increase with loading. This may be because the strong shock in-front of the rotor in the near stall case thickens the casing boundary layer more than the bow shock would in the peak efficiency case. If more of

the rotor tip is encased inside the boundary layer, there may be less momentum for leakage flow to cross the tip gap.

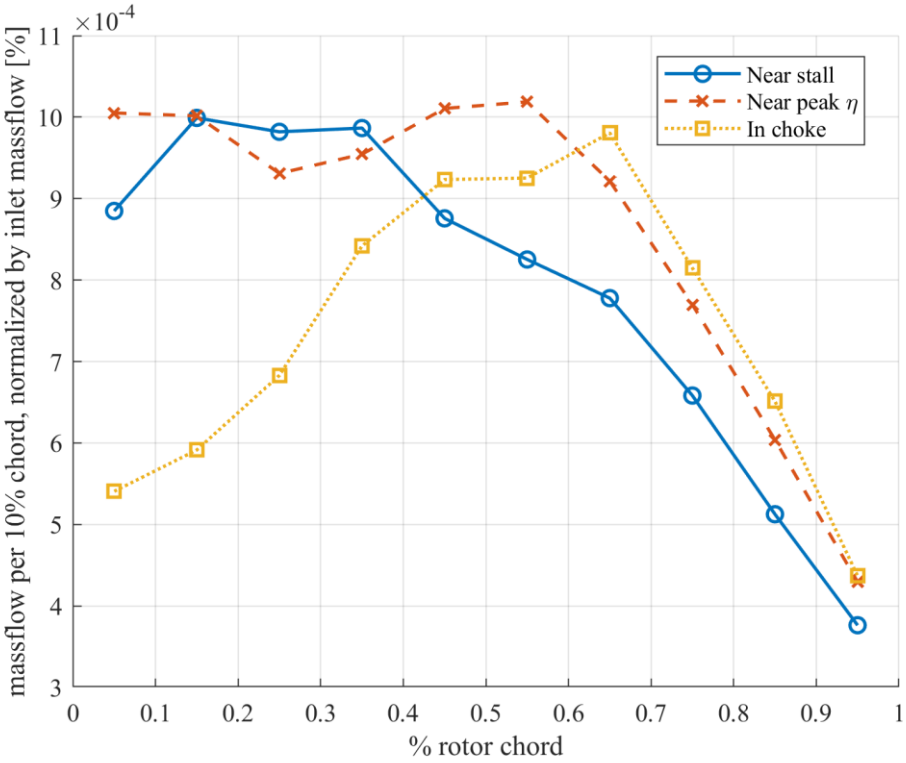

Figure 3.19 Normalized mass flow through the rotor tip, calculated across every 10% chord, for different operating conditions.

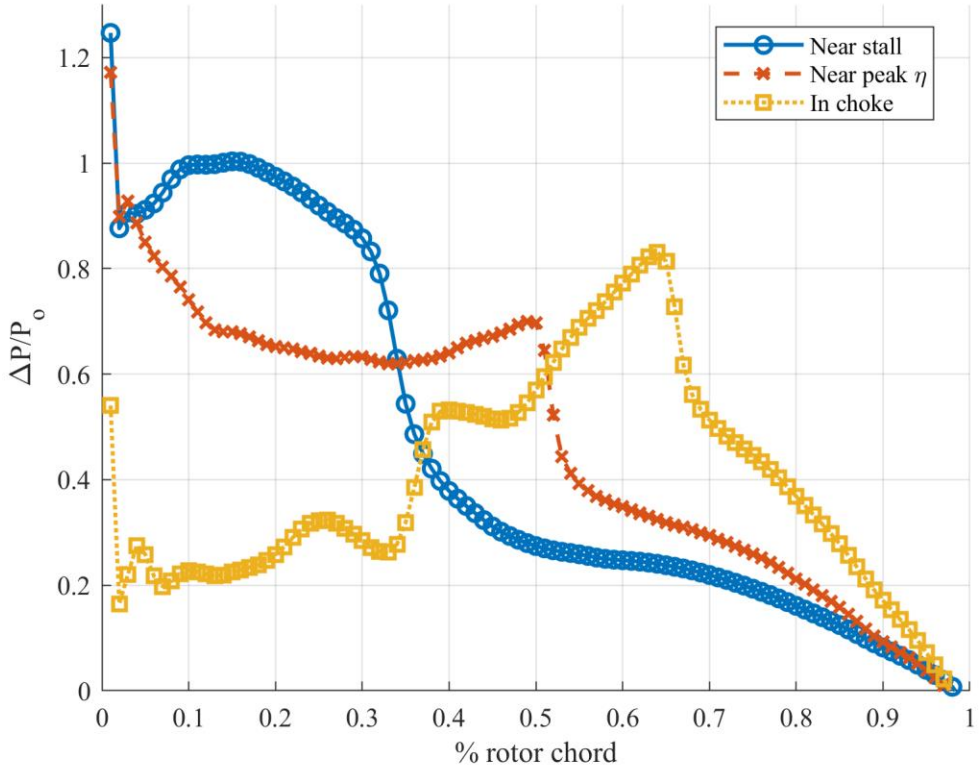

Figure 3.20 Rotor tip static pressure difference from pressure side to suction side, at 98% span. Normalized by total inlet pressure.

The interaction between the tip leakage vortex and the shock is shown in Figure 3.21. The relative Mach number at 98% span shows the location of the shock and the tip leakage flow through the first 10% of the tip gap. The tip leakage vortex core has been colored with normalized helicity to show possible vortex breakdown across the shock. Normalized helicity can be used to observe a drastic change in the tip leakage vortex; if the circulation of the vortex changes directions, normalized helicity will change signs. The definition of normalized helicity is [47]:

$$H_n = \frac{\xi * w}{|\xi||w|} \tag{3.8}$$

Where ξ is the vector of absolute vorticity, and w is the vector of relative flow velocity. The normalized helicity is the cosine of the angle between the absolute vorticity and the relative velocity, because this secondary flow can be considered dominated by the component of absolute

vorticity in the relative flow direction [47]. In Figure 3.21, a change in sign of normalized helicity is indicated by a change in color between black and white.

A moderate shock-vortex interaction is observed for the near stall case. When the tip leakage vortex passes through the shock, the shock front becomes distorted, and the trajectory of the vortex is bent. The cross-sectional area of the strong tip leakage vortex increases across the shock; however, there is no breakdown observed across the shock as indicated by the lack of sign change in normalized helicity of the streamlines. There is a large low momentum region behind the shock-vortex interaction, indicated by the low Mach region in the middle of the rotor passage. Note that there is also spillover of the tip leakage flow into adjacent passages. If the spillover of the flow from one passage into the adjacent one continues to increase, stall will occur.

A weak shock-vortex interaction is observed for the peak efficiency and choke cases. In both bases, the strong vortex core passes through the shock without changing in trajectory or cross section. The shock is slightly distorted by the tip leakage vortex in the peak efficiency case and appears to be unaffected in the choked flow case. Once again, helicity of the strong vortex core does not change across the shock, and there is no vortex breakdown.

From Figure 3.22, the tip leakage vortex trajectory angle changes to move the vortex parallel to the rotor inlet plane as the loading increases. In addition to the movement of the tip leakage vortex, the location of the passage shock also moves forward in the passage with increased loading; hence, the interaction region between the shock and the vortex moves forward. In the near stall case, the interaction region has almost reached the rotor inlet interface plane.

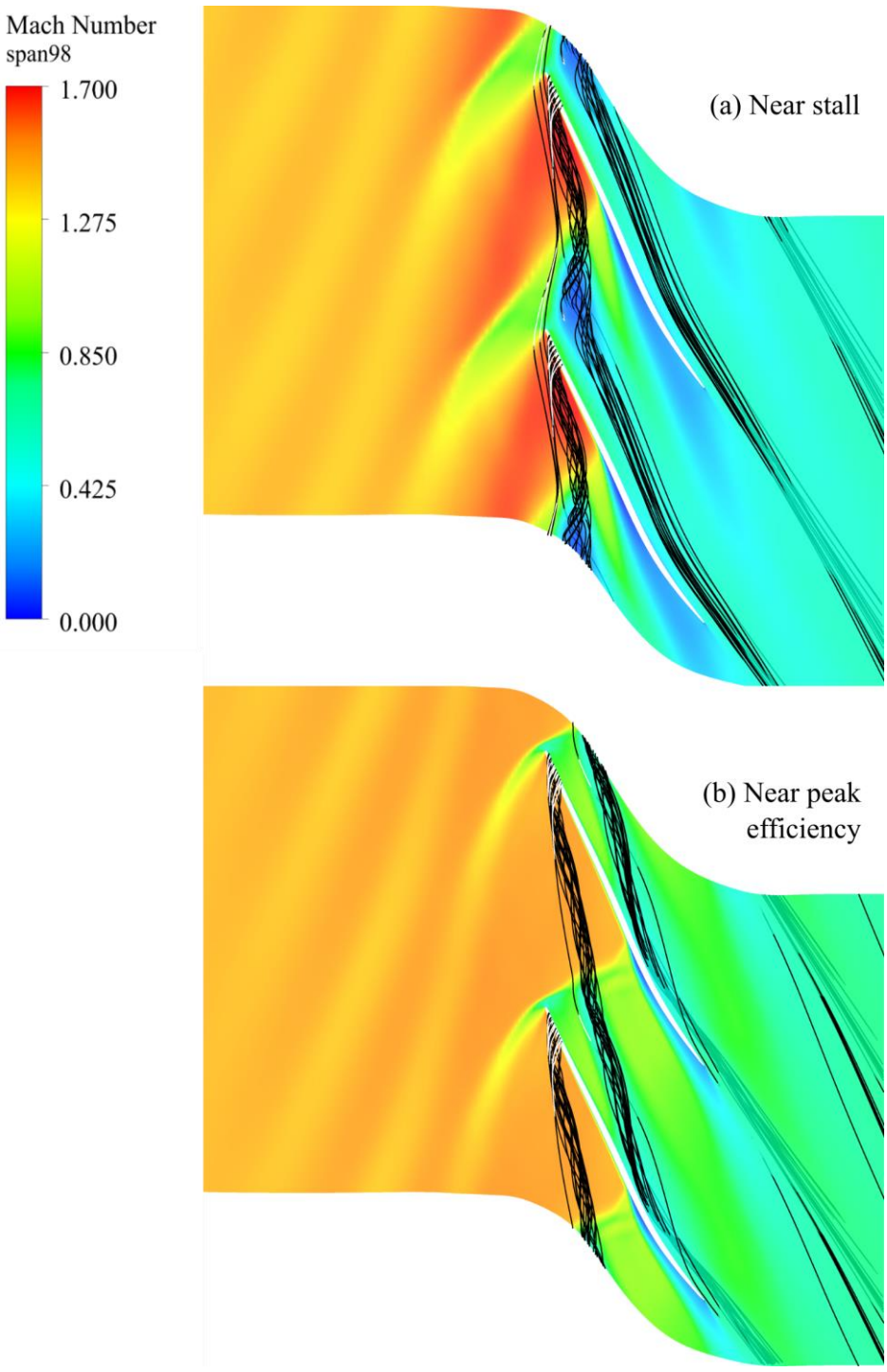

Figure 3.21 Mach number at 98% span with tip leakage flow through first 10% of rotor chord, for loading conditions (a) near stall, (b) near peak efficiency, and (c) in choke. Tip leakage streamlines are colored by normalized helicity.

Figure 3.21 continued.

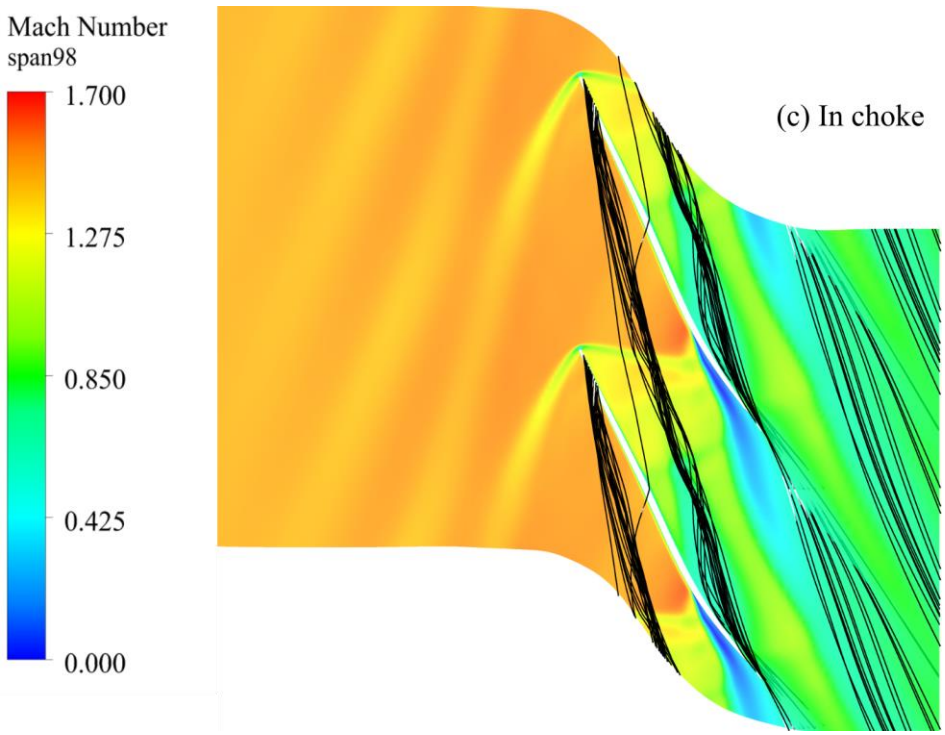

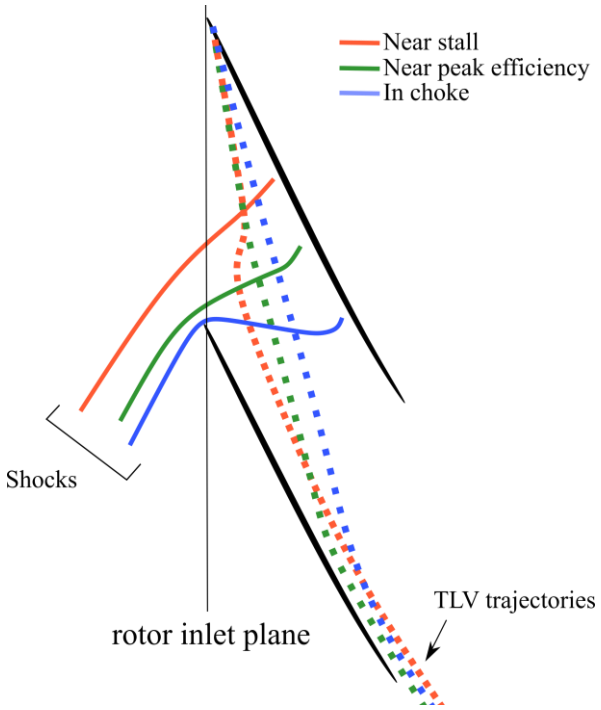

Figure 3.22 Shock locations and TLV trajectories traced from Figure 3.21 for comparison

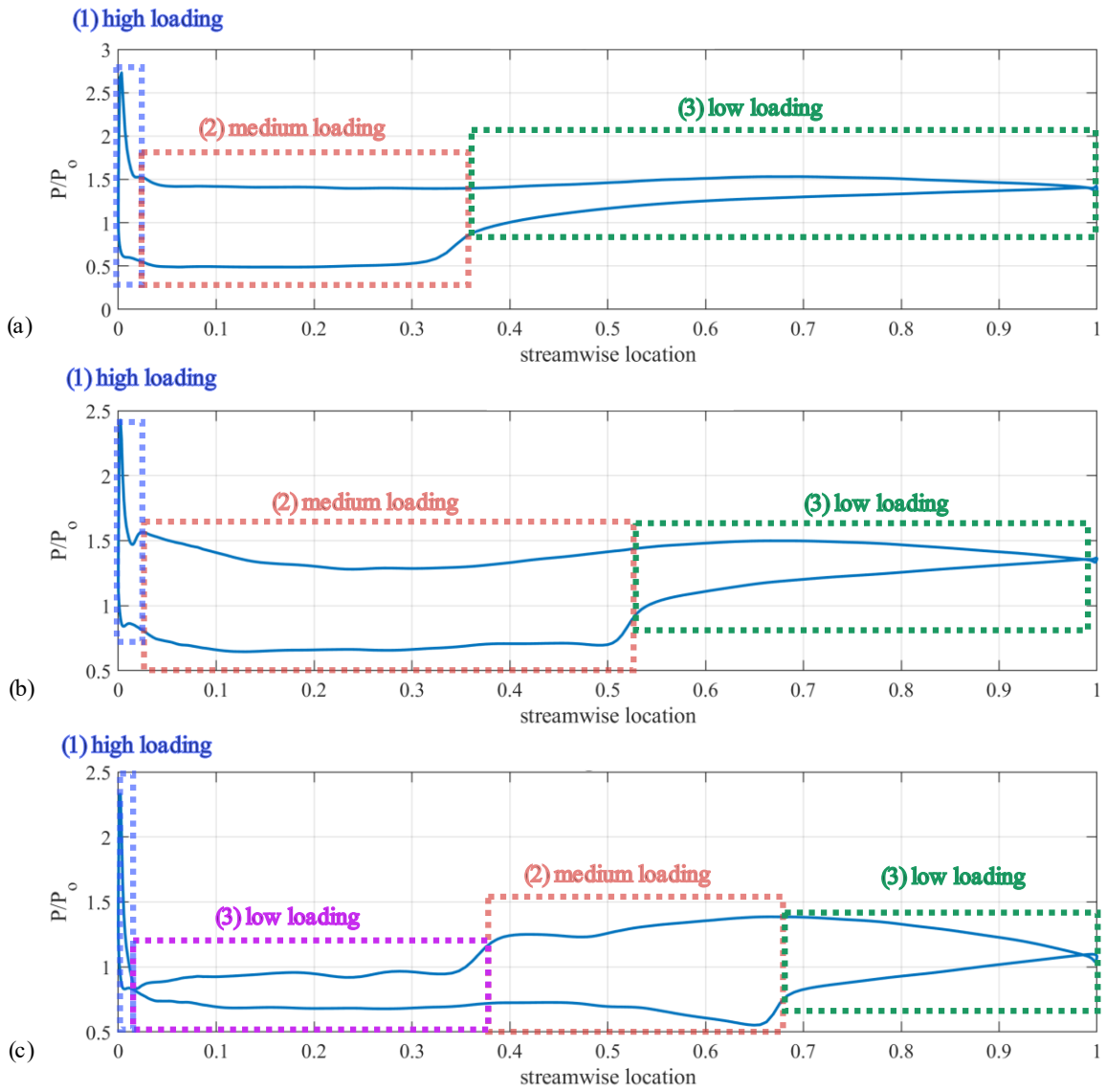

Figure 3.23 Division of tip leakage flow using blade surface loading. For operating conditions (a) near stall, (b) near peak efficiency, and (c) in choke. Static pressure distribution at 95% span for different operation conditions.

In Figure 3.23, the static pressure distribution at 95% span is divided into regions of high, medium, and low blade surface loading following Chima's categorization of the tip leakage flow [19] described in Chapter 1. Note that the loading at the choke condition is very different from that near peak efficiency and stall; there is an extra low loading region right behind the highly loaded leading edge. In choke, there are two weak oblique shocks in the rotor passage; one that starts at

the leading edge and one that starts at around 35% span from the pressure side. This extra low loading region corresponds to the region in-between these two oblique shocks.

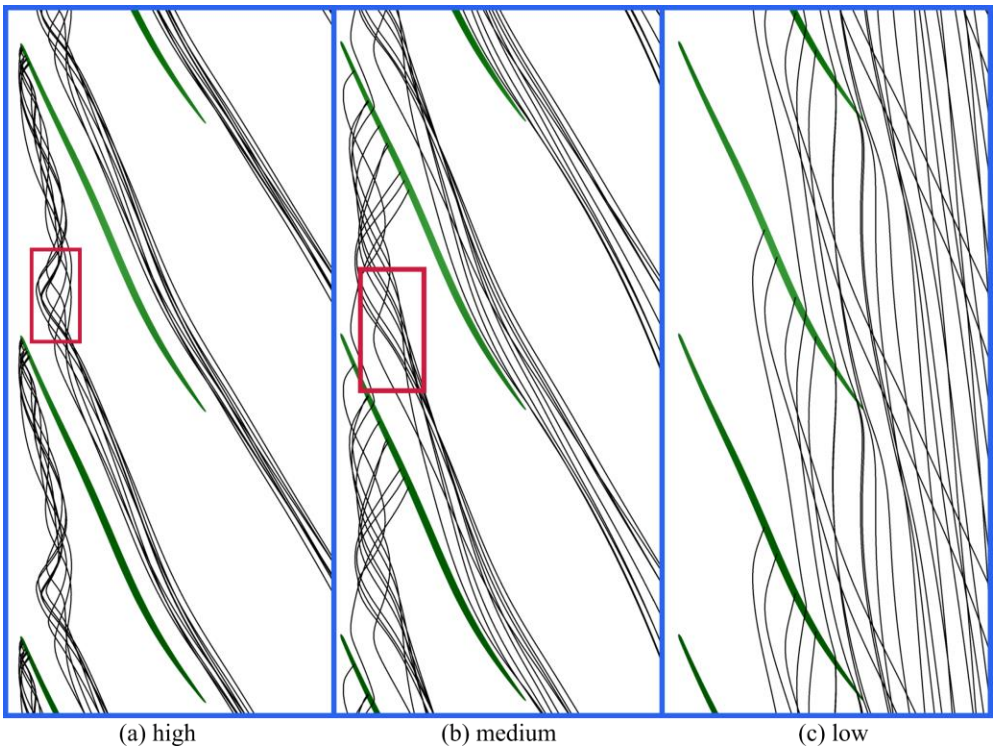

Figure 3.24 Near stall operating condition. Tip leakage flow divided by blade surface loading in Figure 3.23. Effect of shock on tip leakage flow highlighted in red.

As previously observed, the shock does not cause the strong tip leakage vortex core to break down for the near stall operation point. However, in Figure 3.24, the strong tip leakage vortex has lost most of its concentrated vorticity after passing through the shock. The shock-vortex interaction region has been highlighted in red. Note that this interaction region is very close to the rotor shroud; the low momentum region behind this interaction may cause the casing boundary layer to grow significantly or separate. Next, the tip leakage flow corresponding to the medium blade surface loading exits the rotor gap near orthogonal to the rotor chord and almost reaches the rotor inlet plane before being turned half a turn around the strong tip leakage vortex. The negative axial velocity carried by this section of the tip leakage flow will create also some displacement on the casing boundary layer. When this section of the flow passes through the shock, it is easily diffused. This section of the flow has more spanwise influence than the strong tip leakage vortex,

as it is turned and sent downwards into the blade passage by the strong tip leakage vortex. The last section of tip leakage flow, corresponding to the low blade surface loading, sometimes passes from the tip gap of one blade to the next. Note that all parts of the tip leakage flow appear to carry low momentum fluid to the pressure side of the adjacent blade.

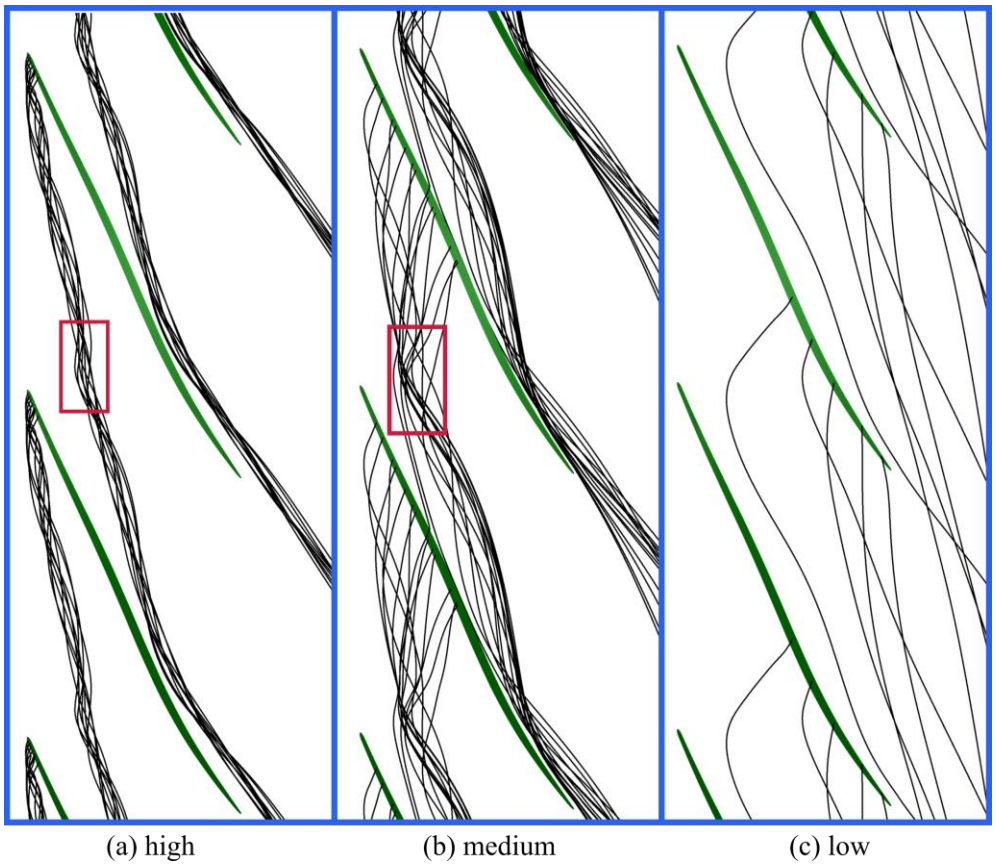

Figure 3.25 Near peak efficiency operating condition. Tip leakage flow divided by blade surface loading in Figure 3.23. Effect of shock on tip leakage flow highlighted in red.

Compared to the near stall operating condition, Figure 3.25 shows that the strong tip leakage vortex at peak efficiency does not lose vorticity after passing through the shock. Again, the tip leakage flow corresponding to the medium blade loading is turned by the strong tip leakage vortex, and its trajectory has been bent by the shock. The flow angle of this tip leakage flow leaving the tip gap is not as aggressive as in the near stall case, and the component of negative axial velocity is smaller. Additionally, the flow corresponding to the low blade loading region appears to be more

aligned with the rotor passage and, thus, likely creates less low momentum buildup at near the rotor tip trailing edge.

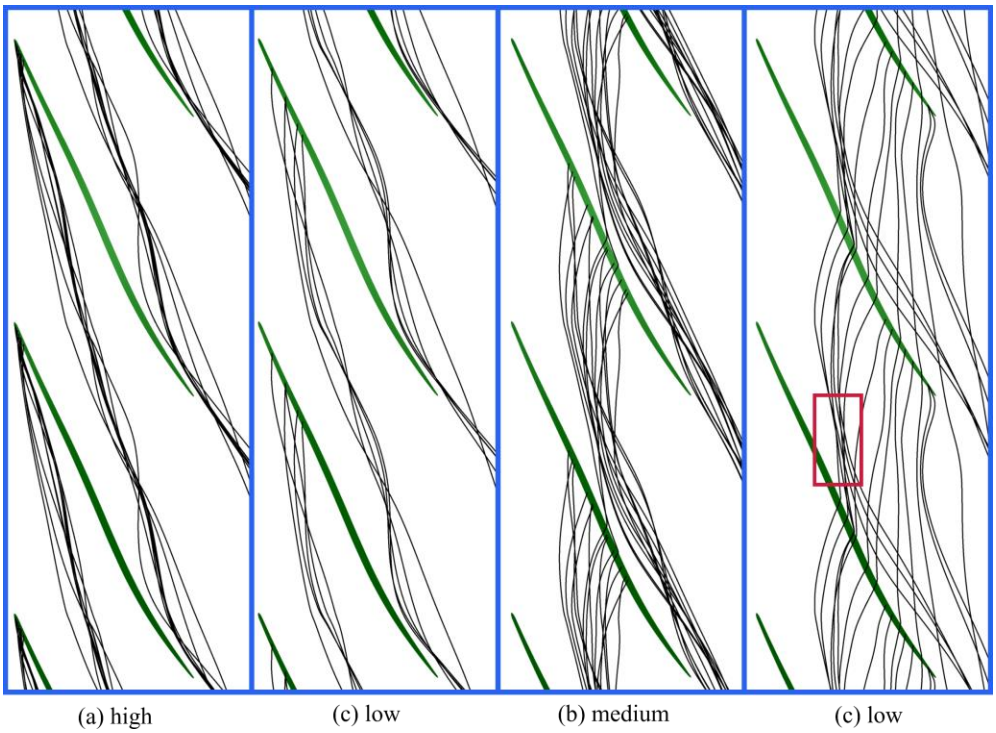

Figure 3.26 In choke operating condition. Tip leakage flow divided by blade surface loading in Figure 3.23. Effect of shock on tip leakage flow highlighted in red.

The flow leaving the strong blade loading region at choke is more similar to a jet than a vortex. From Figure 3.26, no influence of either of the passage shocks on the tip leakage flow can be observed. A region of possible interaction was highlighted in the low blade loading region, however, although the turning of the flow corresponds with the foot of the second oblique shock, it is unclear if the flow turning here is due to interaction with the shock or simply because it is close to the pressure side of the adjacent blade. Note that flow leaving the tip gap here barely has any negative axial component, but flow at the rotor exit is not as parallel as that at peak efficiency, and there must be some increased shear between the low blade loading tip leakage flow and the primary flow.

3.3.3 Effect of Exit Conditions on Stability

Courtesy of previous experimental testing by Honeywell, at 100% speed there is a good indication of where the stall mass flow rate is. As the loading is increased on the speedline towards to near stall, the stability of the CFD solution becomes worse. The solution does not diverge, however, an unconverged solution will jump from the intended mass flow rate to one much lower than the stall mass flow rate; this solution will settle at the lower mass flow rate and will correspond to some level of circumferentially uniform blockage.

To overcome this problem, several approaches were attempted and the following was found (and implemented in the simulations previously presented):

(1) Near stall, the unsteadiness of the flow field increases, and less rigid boundary conditions can make the solution more stable.

(2) Extending the exit domain and creating an area contraction (such as a nozzle) also improves the stability of the problem. Some transient stall simulations use choked nozzles with static pressure boundary conditions for this purpose [48]. A converging nozzle is often used with a static pressure exit boundary condition, and the static pressure is slowly incremented to approach stall.

(3) Combining points (1) and (2), a mesh moving method was attempted. Converging-diverging nozzles are created to choke the flow at the exits of the computational domain. The mesh at the nozzle throat is moved to slowly decrease the throat size as the steady solution iterates. The exit conditions behind the nozzle were either supersonic, such that no reflections should occur from any mismatch in boundary conditions, or the conditions were exit corrected mass flows that force a shock to occur inside the nozzle. The flaws of this approach are not yet known, but for this fan, the mesh moving method has worked better than a converging nozzle with a static pressure exit for getting closer to stall.

(4) It is easier for single passage steady models to get to the stall mass flow rate, compared to part annulus models and full annulus models. Generally, the difficulty of getting a steady state solution close to stall increases when the number of passages used in the model increases. This may be purely due to increased numerical errors from a larger mesh, or it may indicate that several passages are needed for stall cells to properly develop and the stability of the single passage steady model is artificial.

(5) Since this is a tip critical fan, perhaps it would be sufficient to only improve the stability of the bypass exit boundary condition. This is not the case, however, and improvements also had to be made to the core exit boundary condition.

The near stall operating point in this speedline was obtained with the mesh moving method, and the mass flow rate is within 0.5% of the stalling mass flow rate from experiment.

3.4 Turbulence Study

A brief comparison of the influence of turbulence modelling on mixing, dissipation, and flow separation is made. A small section of the 100% speedline has been run with different turbulence models to find an adequate point of comparison. Figure 3.27 and 3.25 show the total pressure ratios and the adiabatic efficiencies of the solutions of different turbulence models at 100% speed. The inlet corrected mass flow for all turbulence models were normalized by the choked mass flow rate of the SST model. With the exception of the BSL-RSM model, which does not have enough points on the speedline for the choke to be well defined, all other turbulence models appear to find similar choke mass flow rates, indicating general agreement of predicted blockage at choke. The k-epsilon and k-omega models predict notably higher efficiencies for the bypass flow, while the k-epsilon model also predicts a higher efficiency for the core flow.

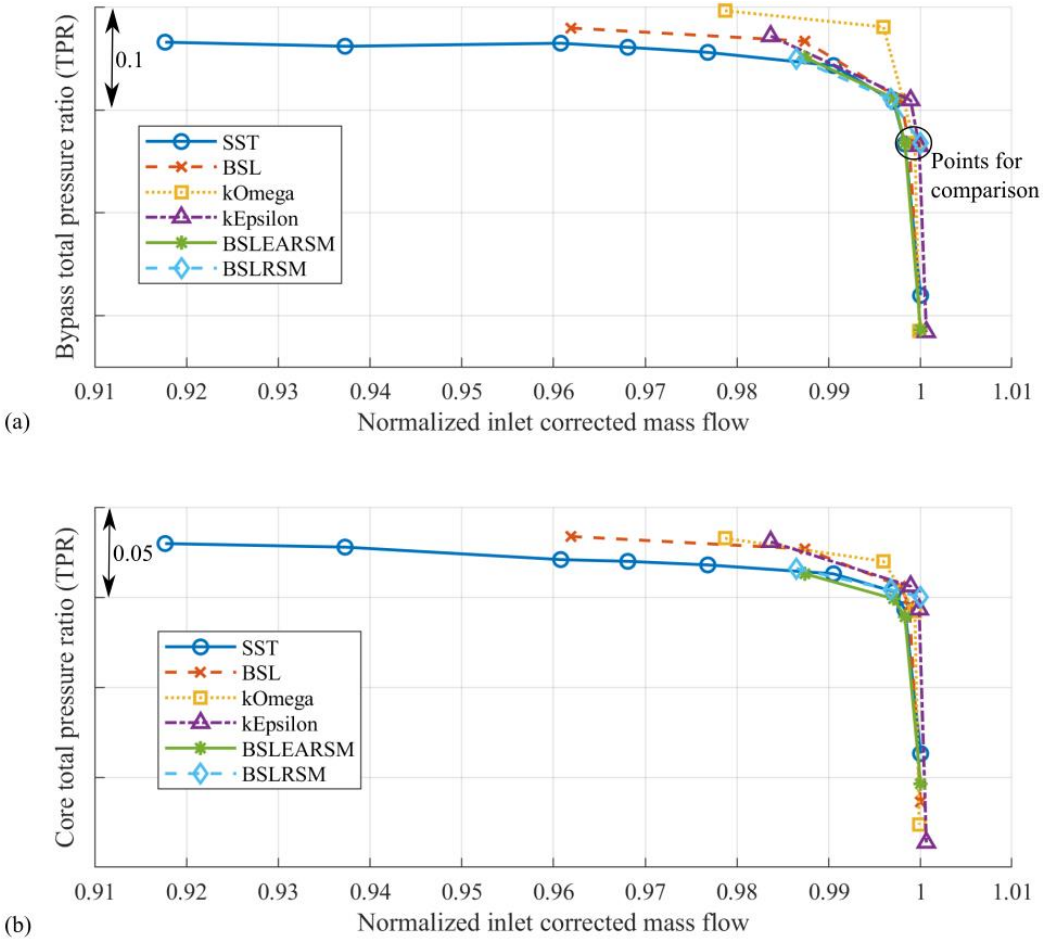

Figure 3.27 Comparison of different turbulence models with at 100% design speed; total pressure ratios for (a) bypass flow and (b) core flow. Inlet corrected mass flow normalized by choke mass flow of SST model.

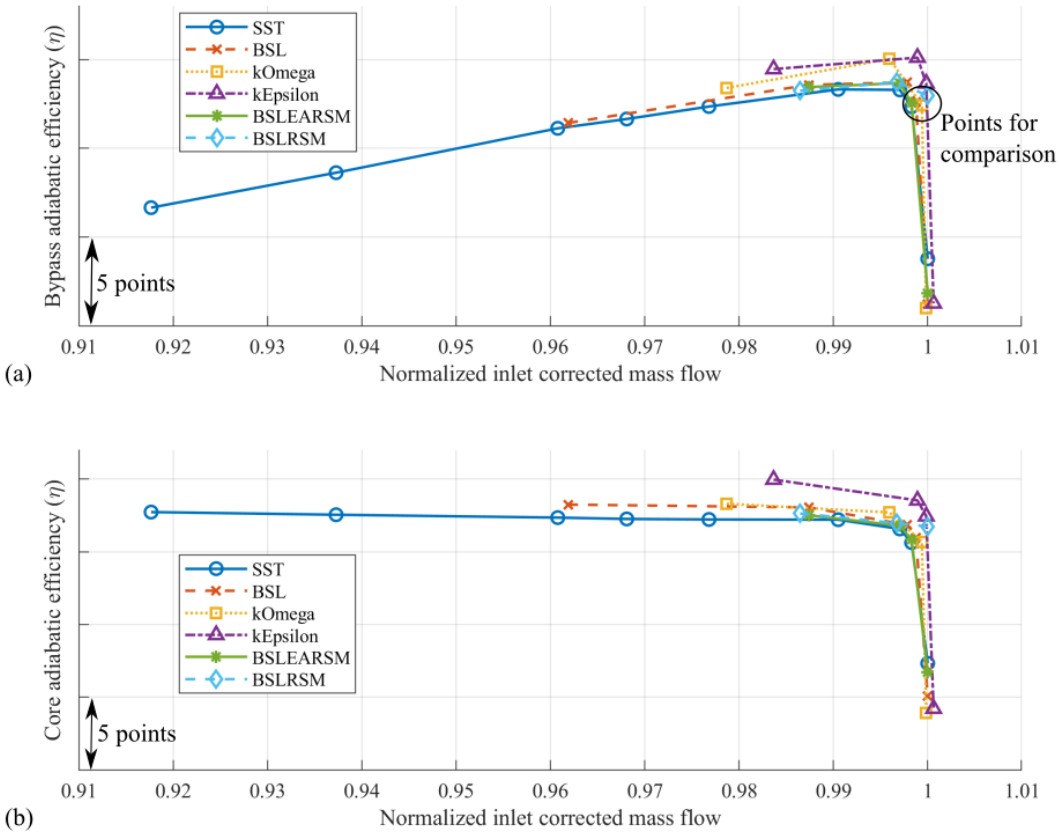

Figure 3.28 Comparison of different turbulence models with at 100% design speed; adiabatic efficiencies for (a) bypass flow and (b) core flow. Inlet corrected mass flow normalized by choke mass flow of SST model.

3.4.1 Points of Comparison

To pick points of comparison between the models, firstly the shape of the characteristic is considered – although the speedlines do not align, the shape of the speedlines should be similar and will correspond to similar loading conditions. The points labeled on in Figure 3.27 and Figure 3.28 roughly correspond to the top of choke operating condition. Secondly, the inlet corrected mass flow is considered; at a constant speed, maintaining the same inlet mass flow roughly maintains a constant incidence angle [49]. There is little difference in inlet corrected mass flow for the comparison points chosen. Thirdly, a comparison of total pressure ratio and total temperature ratio can indicate operation points with similar amounts of loss and work. As shown in Figure 3.29, the operation points are similar in overall work and loss for the bypass, with the exception of the k-epsilon point which is close but does less work. Lastly, the spanwise work distribution varies greatly depending on the loading condition, and Figure 3.30 shows that all comparison points have similar distributions of work. Note that the spanwise work distribution is a strong function of blade design and loading (flow angles), and differences in turbulence modelling is likely not a dominant driver of changes. On the other hand, the turbulence modelling is much more important for the prediction of loss – the total pressure distribution at the leading edge of the stator is much more likely to vary depending on the turbulence model, as shown in Figure 3.31.

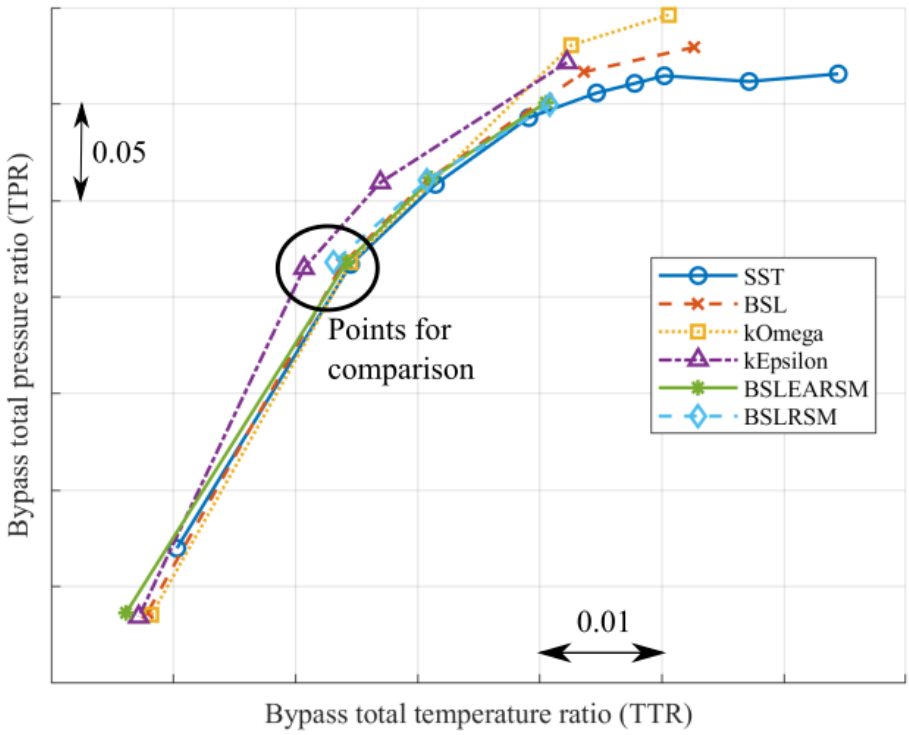

Figure 3.29 Total temperature ratio vs. total pressure ratio for the bypass flow at 100% speed.

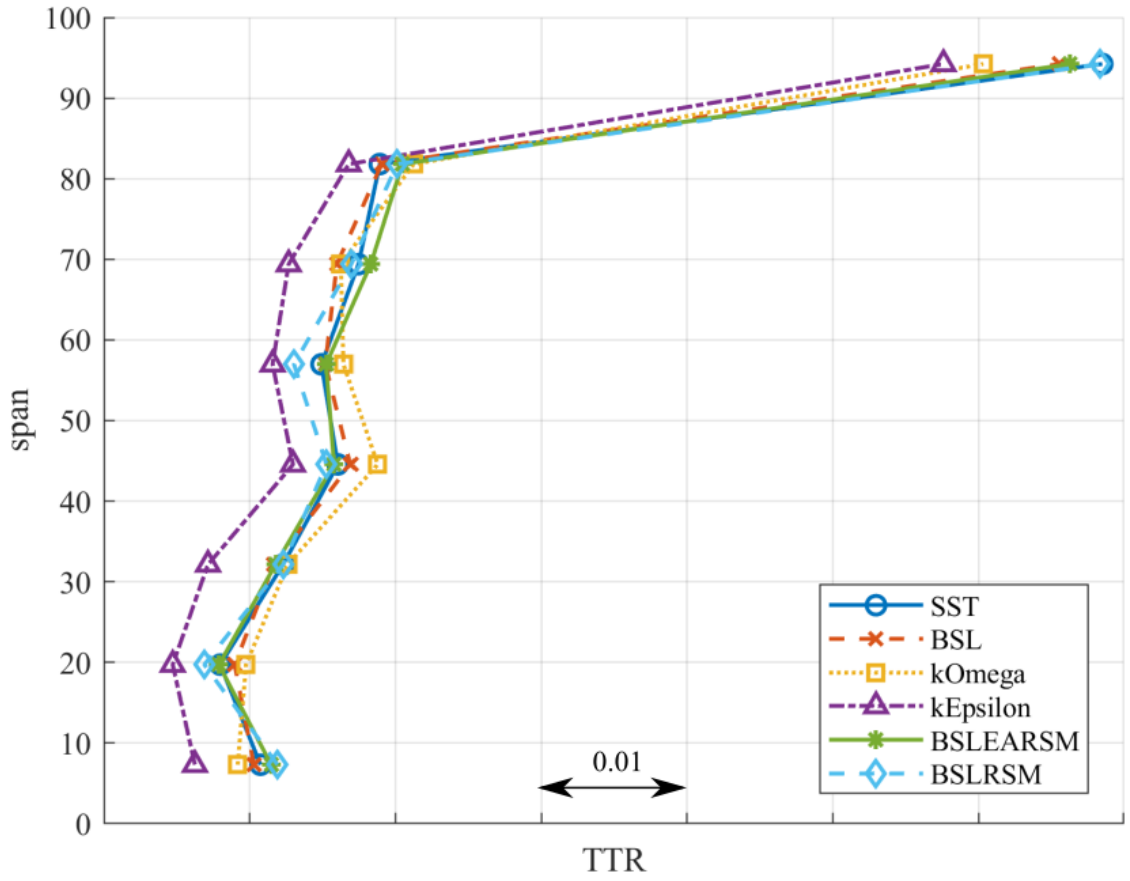

Figure 3.30 Total temperature ratio distribution at leading edge of stator, for different turbulence models at approximately the same loading.

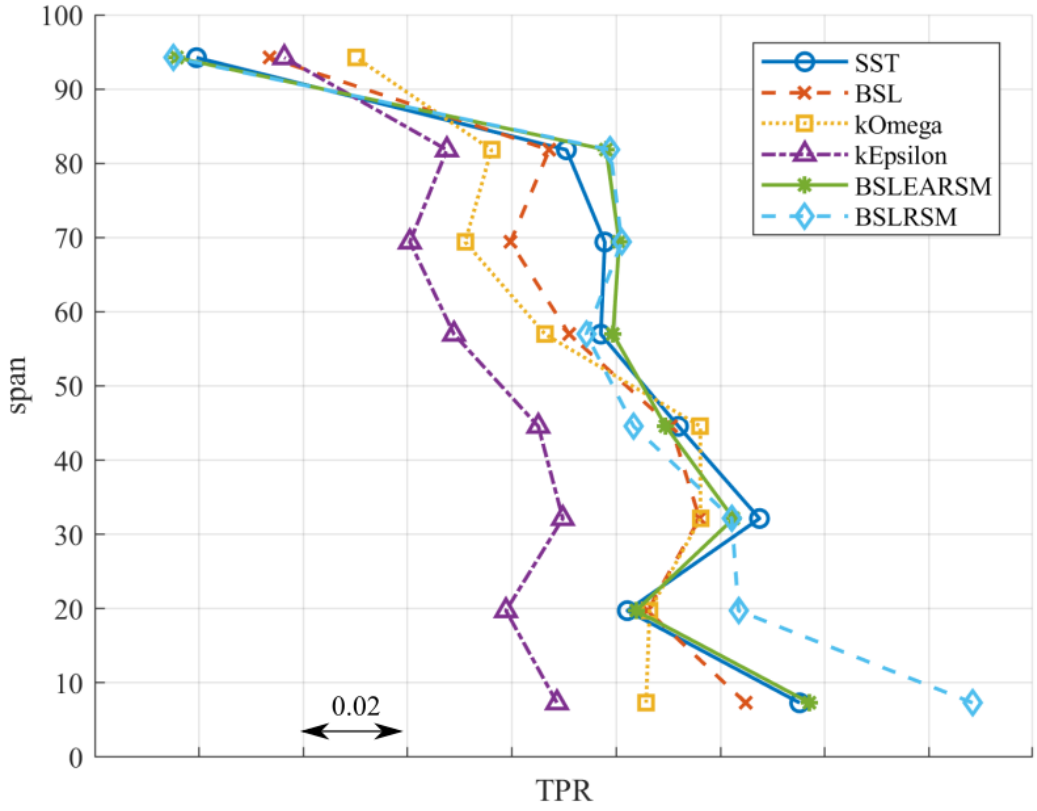

Figure 3.31 Total pressure ratio distribution at leading edge of stator, for different turbulence models at approximately the same loading.

The variation in total pressure ratio profile in Figure 3.31 is quite significant, and as it turns out, this is not only a result of turbulence modeling but also a result of slightly different loading conditions. The BSL, k-omega, and k-epsilon operation points here appear to be slightly deeper in choke than the other models; this is shown in Figure 3.32 in the next section.

3.4.2 Shock Location

A comparison of the streamwise positions of the passage shock in Figure 3.32 show that the points chosen for BSL, k-omega, and k-epsilon are not at the same loading as the other models. Judging by how the passage shock is further into the rotor passage for these points, they are slightly deeper into choke than the other three models. However, the SST, BSL-EARSM, and BSL-RSM models appear to match very well in both shock location, sweep, and strength; these three points

will be used for the rest of the comparisons. From Figure 3.32, the relative Mach number in front of the passage shock matches extremely well regardless of turbulence model; this is expected since this part of the solution is mostly driven by inviscid effects.

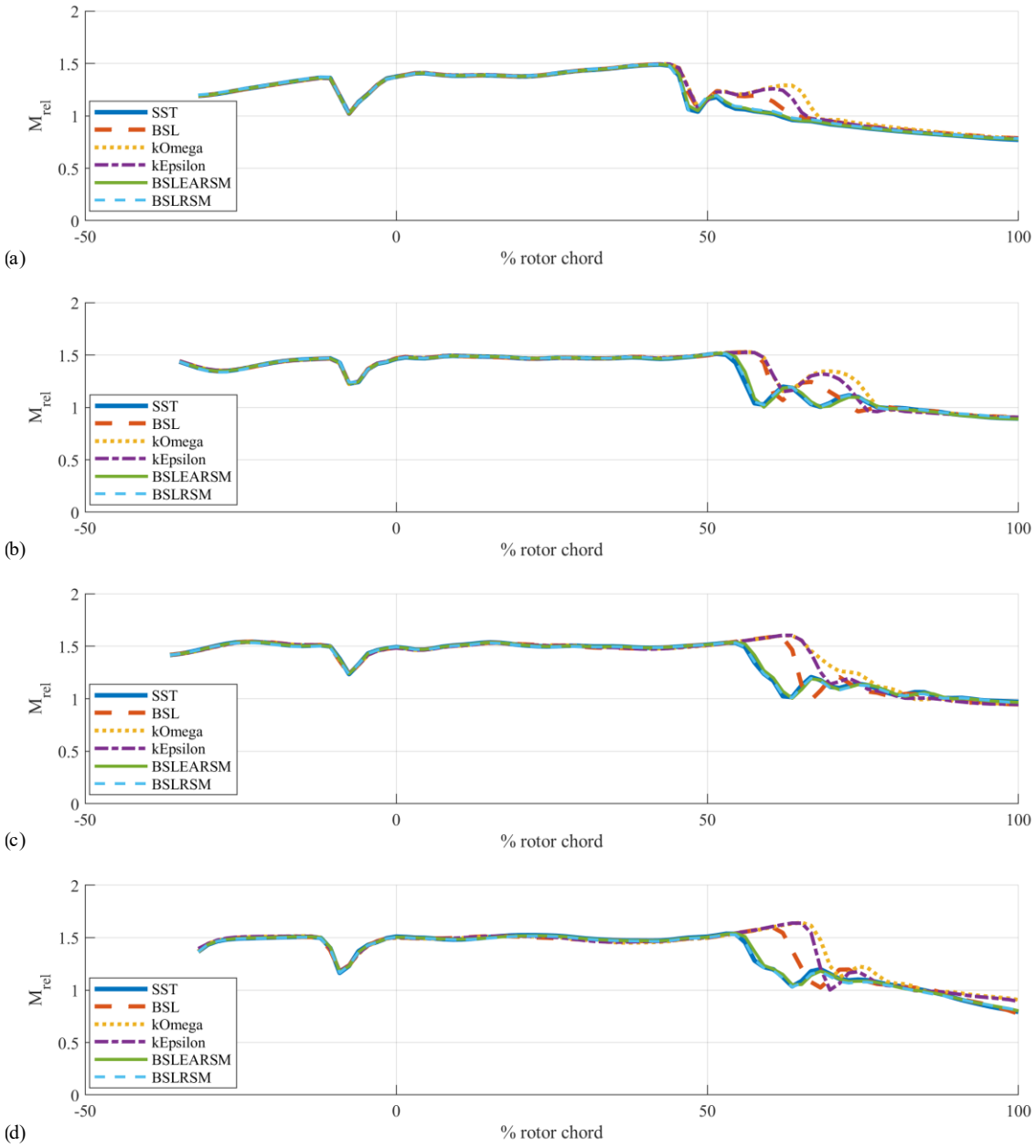

Figure 3.32 Relative Mach number in streamwise direction, at 20% pitch from suction side for (a) 60% span, (b) 80% span, (c) 90% span, and (d) 95% span. For different turbulence models.

The blade-to-blade relative Mach number at different chordwise locations is not shown here, as the solution also matches quite well between the SST, BSL-EARSM, and BSL-RSM models. The method of using the shock location to set a comparison point is not necessarily correct. Perhaps due to different levels boundary layer growth, the passage shock is simply further into the passage at the start of choke for different turbulence models. But this is a decent starting point for this brief study, as the interest in turbulence modelling here is primarily in turbulent effects on the mixing of the tip leakage vortex/shear layer with the primary flow and the influence of turbulence modelling on suction surface boundary layer separation. Hence, the comparison of separation and reattachment behind the passage shock is easier to make when the passage shock is similar in both strength and location.

3.4.3 Boundary Layer Separation

Figure 3.33 shows the limiting streamlines on the suction surface of the rotor, for a loading near the top of choke (figure has been skewed due to proprietary geometry). The pressure rise across the passage shock creates boundary layer separation along the suction surface, indicated by the long separation line (1) from below midspan to the shroud. The passage shock terminates a bit below midspan, and there is a strong radial flow behind the passage shock that convects low momentum fluid towards the rotor shroud. All three turbulence models agree on the sweep and termination of the passage shock, but behavior of the separated flow behind the shock is very different. The shape of the reattachment line for the EARSM and RSM models are more swept back towards the shroud compared to the SST model, and the curvature of the reattachment line near the rotor tip suggests that the SST model has more backflow/ a greater momentum deficit near the tip. The SST model also predicts stronger radial flows, and limiting streamlines at the rotor exit are near parallel to the trailing edge. There are still strong radial flows in the BSL-EARSM and BSL-RSM models, however, the streamlines indicating radial flow end on the trailing edge near the rotor tip, instead of at the rotor tip like in the SST model. Between the EARSM and RSM cases, the radial flow of the EARSM case is stronger.

Below midspan, there is another separation line (2). This separation line is caused by another shock. Near the hub, the rotor inlet Mach number is low enough that there is no longer a bow shock at the leading edge. However, the inflow may still be transonic, and may be accelerated locally to the supersonic regime. The increased camber near the hub helps the flow accelerate

along the suction surface. This second shock may then occur because the rotor is choked, or to meet a downstream boundary condition. There is a small region of radial/separated flow behind this shock; the pressure rise through a normal shock may be enough to cause boundary layer separation if the relative Mach number is above 1.4 [50]. This small shock increases the migration of fluid from hub to tip and is a contributor to the hub corner separation at the trailing edge.

Recalling that the RSM model best accounts for the effects of streamline curvature and system rotation, it is likely that the BSL-RSM model is giving the most accurate result for flow separation and reattachment. Despite the SST model having been modified for curvature correction (through promoting turbulence production and thus reattachment of separated flow), the prediction of the SST model is quite far from the RSM result. This difference might be reduced by tweaking the curvature correction term, as currently it looks like the SST model is reattaching too early near the rotor tip and too late near mid-span. If the RSM model is assumed to give the most accurate result, this also means that the prediction of exit flow angle may be poor at the trailing edge for the SST model, as the streamlines do not follow the shape of the blade, and there is potentially a little bit of flow spilling over from the pressure side to the suction side.

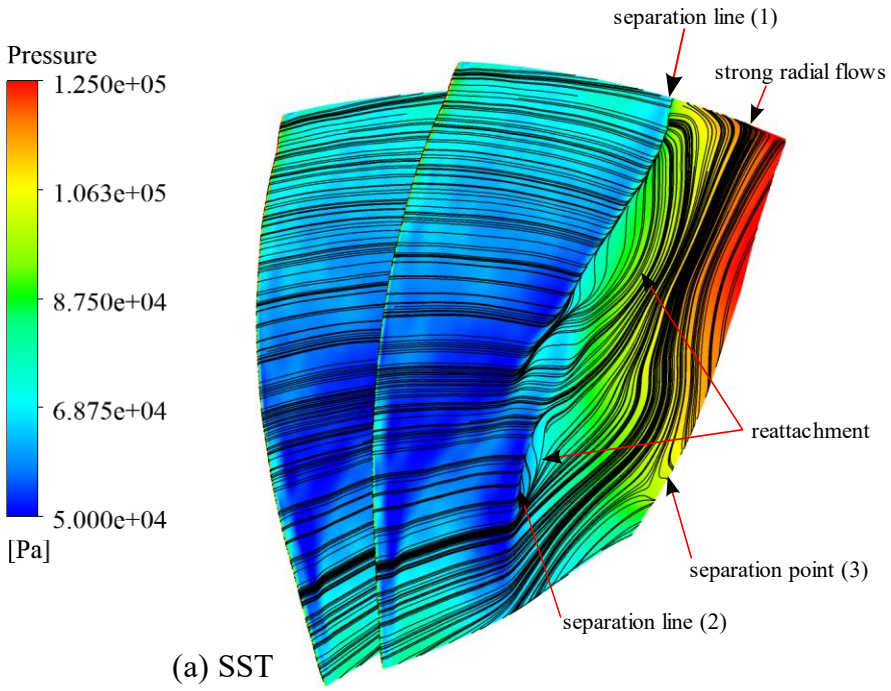

Figure 3.33 Limiting streamlines on suction surface of rotor. Operating point near peak of choke, for turbulence models (a) SST, (b) BSL-EARSM, and (c) BSL-RSM.

Figure 3.33 continued.

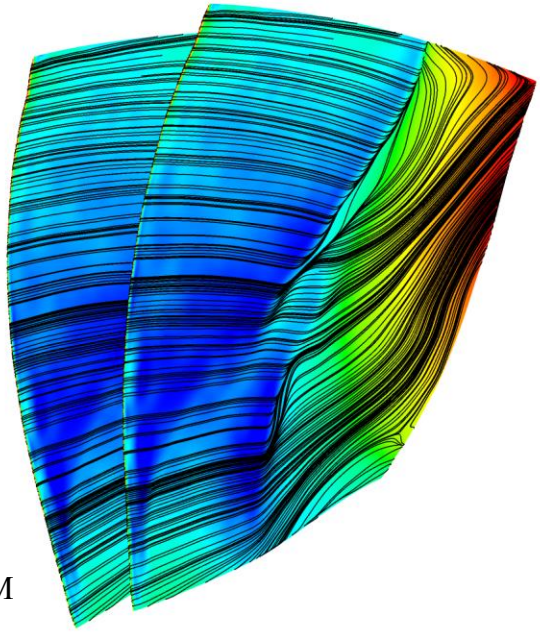

(b) BSL-EARSM

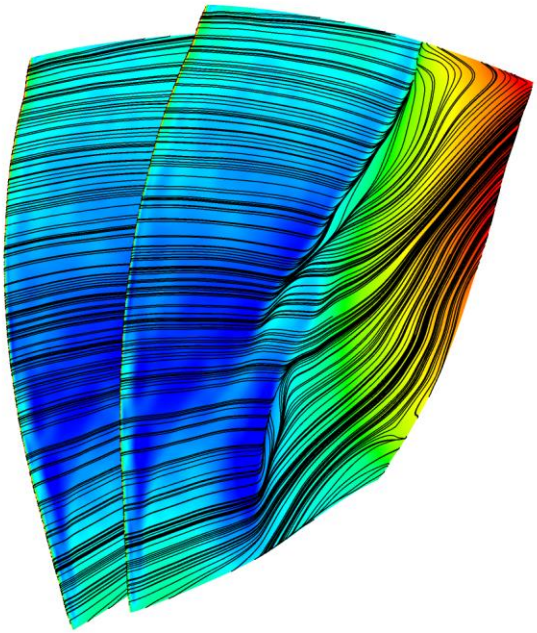

(c) BSL-RSM

3.4.4 Tip Leakage Flow

The mass flow distribution through the tip gap is not shown here, as they are nearly the same across the different turbulence models; the trajectory of the strong tip leakage vortex across the passage is also not shown, as it is also the same. These similarities are expected as the tip leakage flow is primarily driven by the pressure gradient, an inviscid effect. However, the mixing of the tip leakage flow and the primary flow is affected by turbulence. The tip leakage flow at 10% rotor chord is plotted in terms of relative Mach number in Figure 3.34. From the pressure side to the suction side, there is a Prandtl-Meyer expansion past the corner of the blade, and the flow is accelerated through the tip gap, exiting as a jet into the suction side. The shear layer between the tip leakage flow and primary flow is attached to the suction surface and is roughly represented through the Mach 1.2 contour. Comparing between the different turbulence models, the SST model predicts the least spanwise intrusion into the primary flow, while the EARSM and RSM models predict a similar level of spanwise influence.

The tip leakage vortex crosses the rotor passage and impinges on the pressure side of the adjacent blade. The vortices from the three models have visually indistinguishable trajectories, and the impingement on the pressure side is shown in Figure 3.35 at 80% rotor chord. Here the vorticial structure has merged with the pressure side boundary layer in the SST model, but it is still somewhat distinguishable in the EARSM and RSM cases. Observing the Mach 1 contour, it seems like all three models have a similar degree of influence on the primary flow, with SST having a slightly smaller influence. On the suction side of the blade, the back flow region behind the passage shock near the rotor tip appears have the smallest radial extent for the SST model.

Here the blade tip is modelled with sharp corners, which doesn't reflect the actual geometry that is likely slightly rounded. Denton [28] noted that even slight rounds on the edge of the rotor tip may significantly increase the tip leakage flow (by almost 30% in Denton's comparison). An increase in the tip leakage flow increases its spanwise influence. In the rotor 37 blind study, the radial extent of the tip leakage flow was underpredicted, and this was likely a contributor to the overprediction of total pressure ratio near the tip [46]. If it is found that the radial influence of the tip leakage flow is underpredicted in experiment, small adjustments to the rotor tip geometry and turbulence model may alleviate some of the difference.

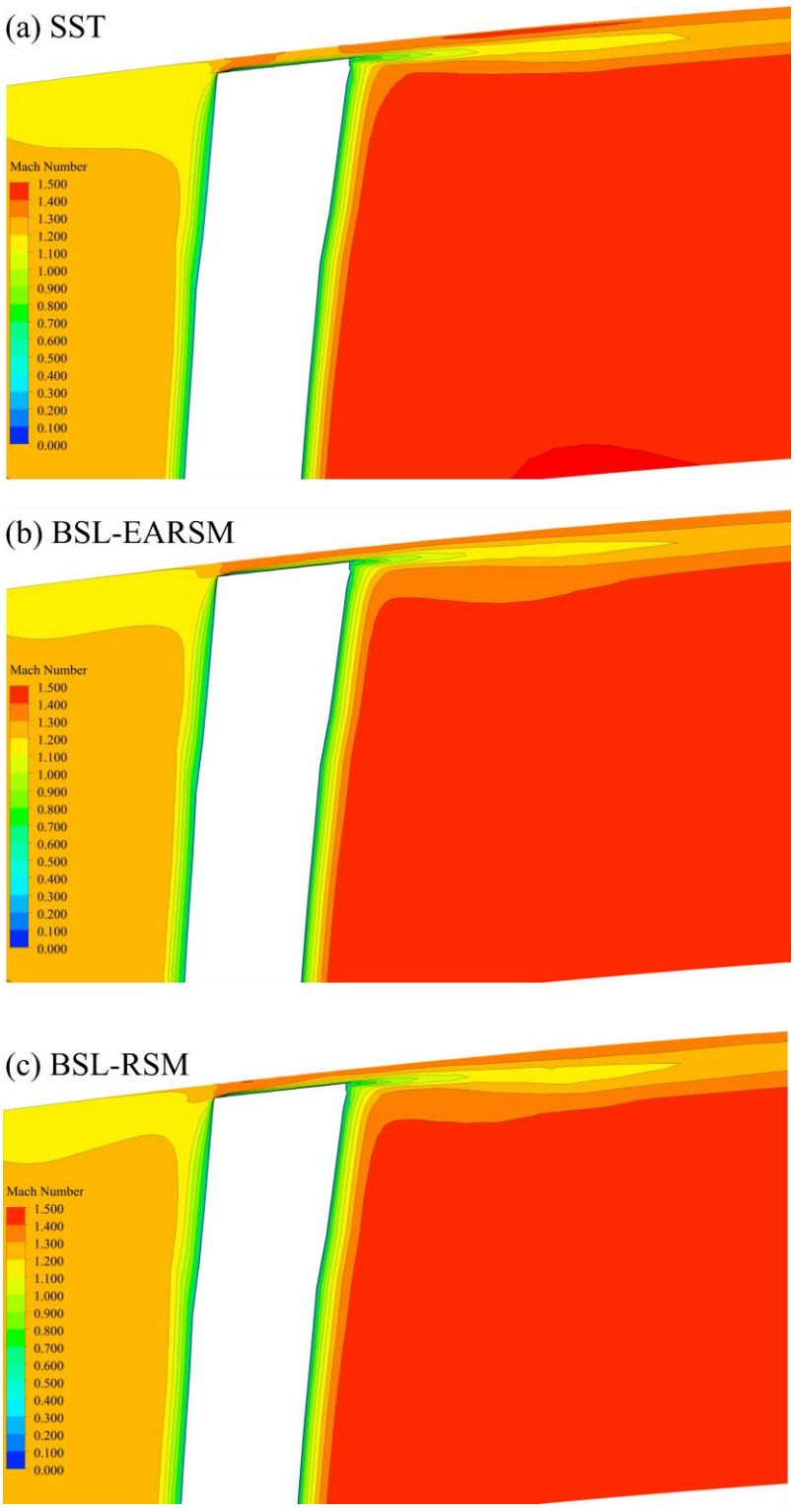

Figure 3.34 Relative Mach number of tip gap at 10% rotor chord, with different turbulence models: (a) SST, (b) BSL-EARSM, (c) BSL-RSM. The left side is the pressure surface, the right side is the suction surface.

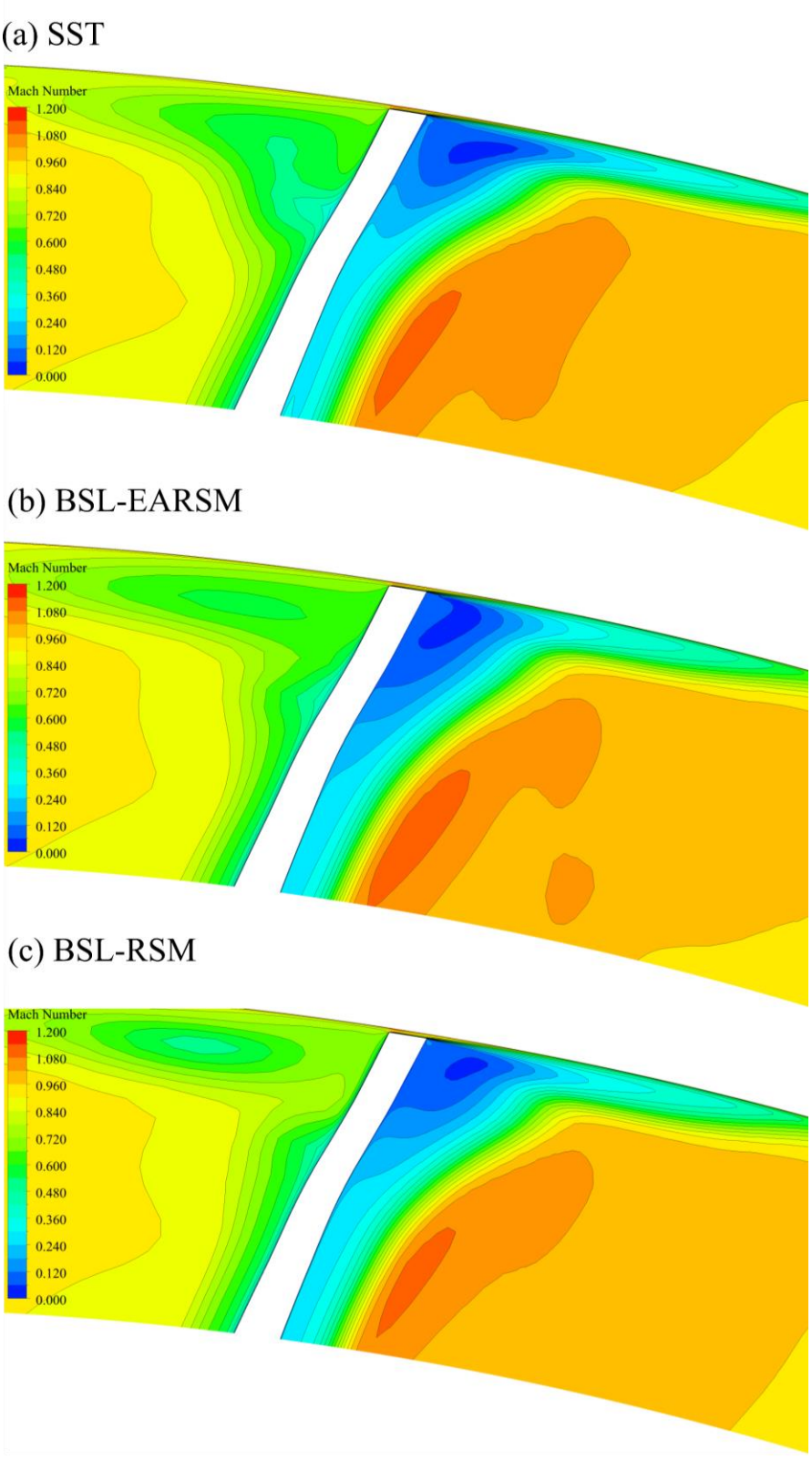

Figure 3.35 Relative Mach number of tip gap at 80% rotor chord, with different turbulence models: (a) SST, (b) BSL-EARSM, (c) BSL-RSM. The left side is the pressure surface, the right side is the suction surface.

3.4.5 Rotor Wake

A last comparison is made for the mixing and dissipation of different turbulence models with the wake 30% chord downstream of the rotor. At lower spans, the shape of the depth and width of the wake is similar for all three turbulence models, although RSM predicts a slightly deeper wake than EARSM and SST. At 95% span, the EARSM and RSM models have more distinct features, likely due to the tip leakage flow not being as mixed as in the SST case. Note that there is a slight shift in the location of the SST wake at 95% span; recalling the limiting streamlines on the suction surface of the SST model in Figure 3.33, this slight offset is possibly due to a difference in exit flow angle prediction.

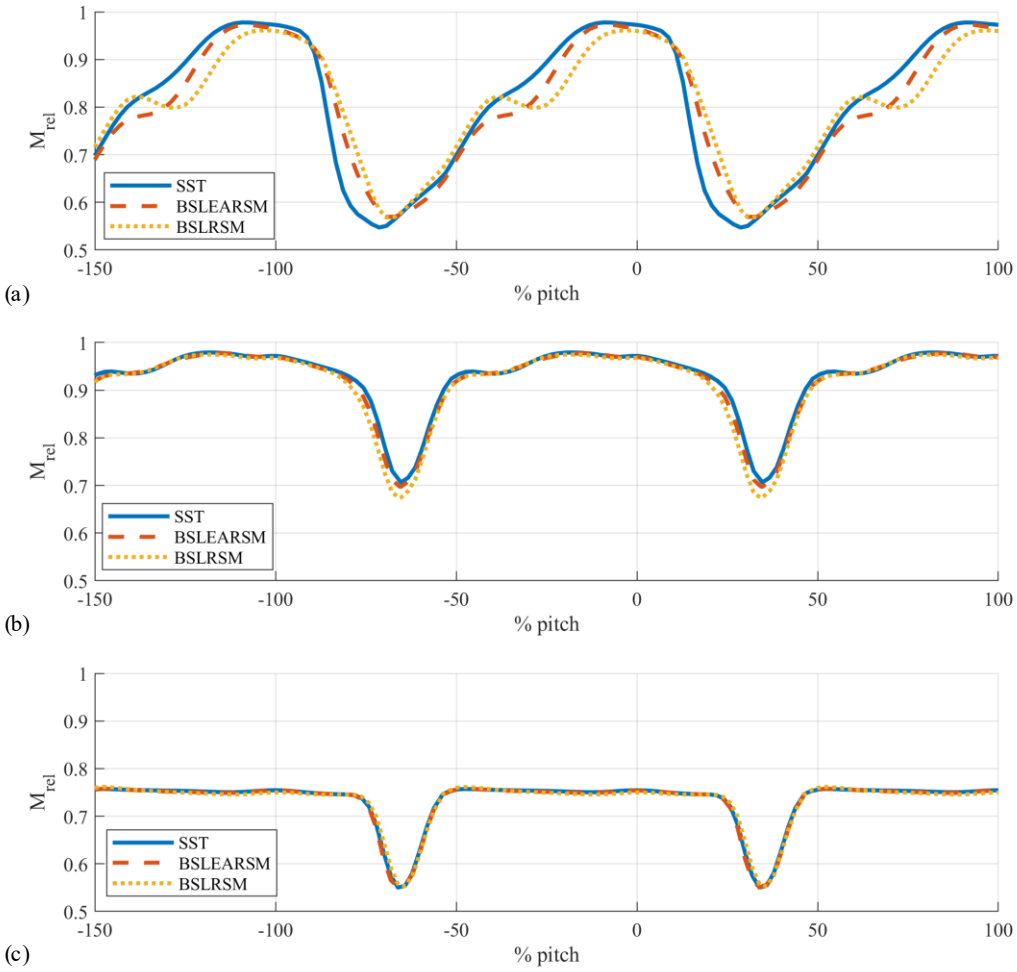

Figure 3.36 Rotor wake 30% chord behind rotor, for operation near top of choke. Comparison at (a) 95% span, (b) 90% span, and (c) 50% span. Comparison of mixing and dissipation for different turbulence models.

3.4.6 Consideration of Computational Time

The difference in time it takes for the different turbulence models to complete one iteration is slightly more from SST to BSL-EARSM (1.3 times), and the same order from BSL-EARSM to BSL-RSM. The challenge with using more complex turbulence models is that it may be much more difficult for the simulation to reach convergence; for example, for one of the speedline runs, the BSL-RSM model took more than 10000 iterations past how many the BSL-EARSM model needed to reach an acceptable level of convergence. Similarly, with BSL-EARSM compared to SST, the number of iterations required to reach convergence is much greater. Hence, despite the difference in predictions due to turbulence modelling suggesting that at least BSL-EARSM is needed to resolve the radial flow behind the passage shock, it may be in the interest of time to use the SST turbulence model.

3.5 Other Considerations

The following considerations on the modelling of the inlet boundary layer and wall roughness are discussed briefly.

3.5.1 Effect of Inlet Conditions

The casing boundary layer thickness is expected to have an impact on loss and blockage near the rotor tip; there will be boundary layer rakes upstream of the rotor, so this is a quantity that can be calibrated. Previously mentioned in Chapter 2, for most of the simulations the walls were set to be rough no slip walls. In the inlet domain, setting the casing walls to rough no-slip walls will cause the boundary layer thickness to build up quickly, especially in when the inlet has been extended to allow disturbances/reflections to decay before reaching the rotor. A brief comparison of the effects of inlet casing boundary layer thickness is made by considering three configurations of the inlet casing wall: (1) free-slip until three rotor diameters upstream of the rotor leading edge, (2) free-slip until one full tip circumference upstream of the rotor leading edge, and (3) no-slip rough wall.

The point is chosen in the same manner as that for the turbulence model comparison; the operation points chosen are at very similar loadings, the work and total pressure profiles line up, and the shock location matches. Decreasing the length of the no-slip wall appears to have shifted

all characteristics to a higher mass flow rate, but there were negligible changes to the total pressure ratio and temperature ratio. The point of comparison chosen is between peak efficiency and top of choke. The cases were run with SST and a medium mesh.

A decrease in total pressure ratio of the boundary layer in Figure 3.37 shows the thinning of the boundary layer with decreased lengths of no-slip casing wall at the inlet. Assessing the cross-sectional blockage 10% chord behind the rotor (with a ratio of the mass flow rate found with area-averaged values and mass-averaged values), the blockage has increased marginally from 3.71% to 3.83% between configurations (1) to (3). The spanwise distribution of blockage calculated with Suder's method [30] in Figure 3.38 shows that blockage above 85% span is noticeably altered due to the difference in boundary layer thickness. However, the mass flow rate through the tip barely changes; the flow rate through the gap behind the passage shock impingement on the suction side increases slightly for configurations (2) and (1) compared to (3), but this change is negligible (on the order of 10^{-5} kg/s).

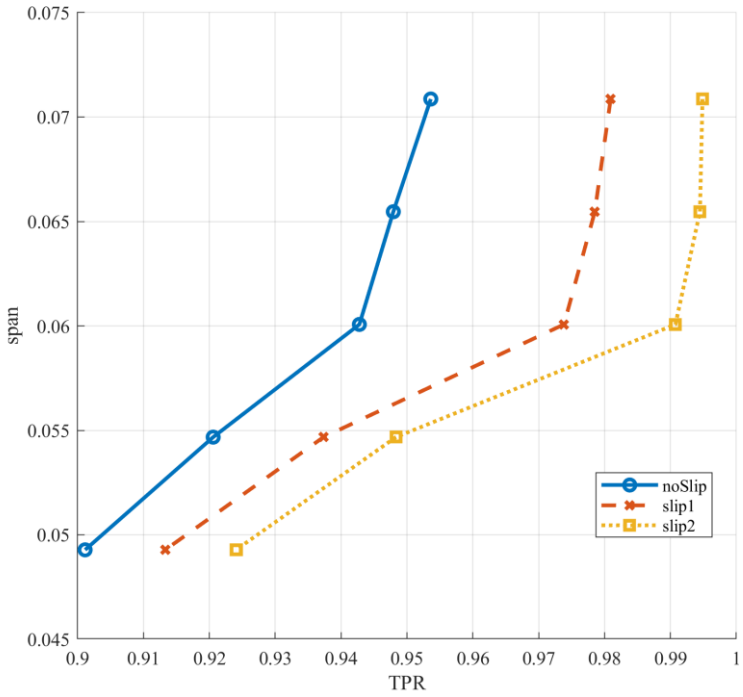

Figure 3.37 Total pressure distribution at inlet boundary layer rake locations, near the aerodynamic interface plane.

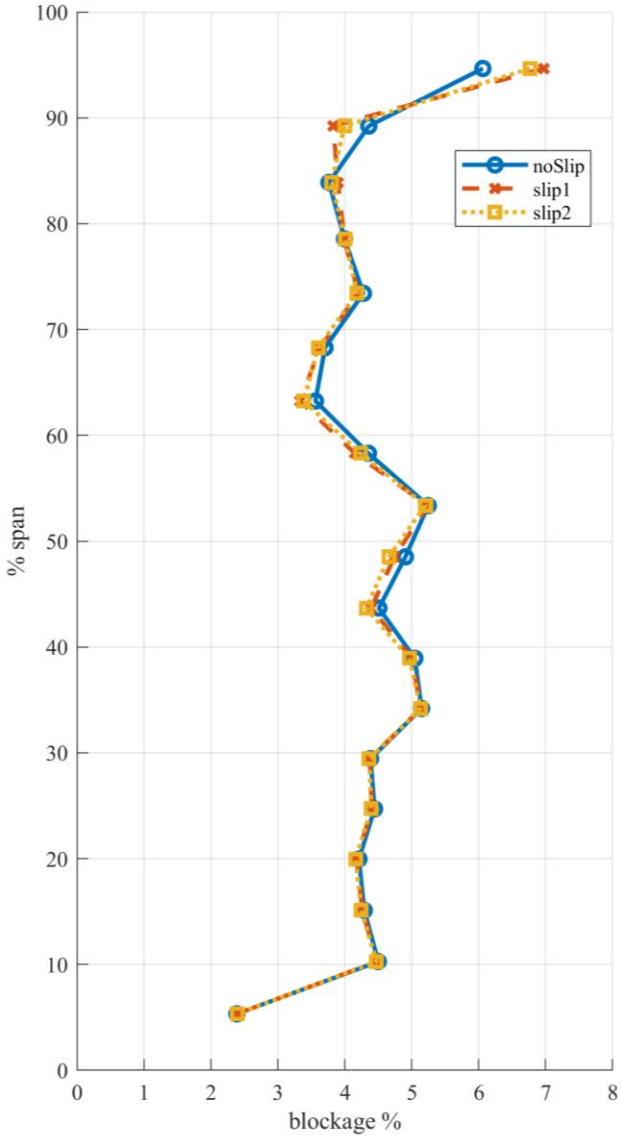

Figure 3.38 Spanwise distribution of blockage 10% chord behind the rotor; comparison of inlet boundary layer.

3.5.2 Rough and Smooth Walls

The necessity of including wall roughness in modelling was briefly considered. This comparison was made with the same inlet and outlet boundary conditions using a medium mesh, for an operating point near the top of choke of a rough wall case. Neglecting the roughness of the wall at this point increased the mass flow rate by ~0.3%, which is past the choked mass flow rate of the rough wall speedline. The distribution of the total temperature ratio in-front of the stator

leading edge showed that this smooth wall case is further into choke than the rough wall case. Additionally, the efficiency of the smooth wall case was 1.5 points of efficiency higher in the bypass and 2.5 points of efficiency higher in the core. Note that the effect of roughness has a large effect in transonic fan performance; although the shock location may not change between comparable smooth and rough walls, adding roughness to the blade causes the blade boundary layers to thicken and thus degrades the performance of the fan (by causing the shock-suction side boundary layer interaction to create greater blockage) [49]. Hence, applying roughness reflective of the experimental geometry is important.

It is important to check the hydraulic smoothness of the walls before assigning a surface roughness. After calculating the Reynolds number, all surfaces are hydraulically rough except the rotor blade, rotor hub, and stator vane; thus, these three surfaces can be modelled as smooth walls. All walls are modelled as rough in the simulations discussed in this thesis; the rotor blade, rotor hub, and stator vane were only modelled as smooth walls in later simulations.

3.6 Summary of Steady Modelling Decisions

The CFD model needs to be adjusted when experimental data is available for comparison; the following modelling choices for steady simulations are based purely on CFD results:

- Using a single passage coarse mesh with 8 million elements is sufficient for qualitatively resolving the passage shock and tip leakage flow. When accuracy on quantitative properties of the flow is important, the medium mesh with 22 million elements should provide a solution with small discretization error.
- The SST model captures flow field features qualitatively, with possible error in the prediction of boundary layer separation and strength of the radial flow behind the passage shock. The EARSM and RSM models are too costly for iterative simulations (i.e. to test different casing treatments). However, if there are large discrepancies in radial flow behind the passage shock observed in experiment and CFD, using BSL-EARSM (or BSL-RSM) may improve agreement.
- To find comparable points between simulations or experiment, it is suggested that an operation point at a similar category of loading (i.e. peak efficiency) is found on their respective speedlines. The shape of the spanwise work distribution behind the rotor may be a good trend to match for finding a point of comparison.

- Changing the start location of the inlet boundary layer on the rotor shroud slightly has a notable effect on choke mass flow rate and blockage near the rotor tip, but a small effect on other performance parameters. The experimental boundary layer thickness should be applied to the CFD model before comparing choke mass flow rates between CFD and experiment.
- Roughness has important effects on both loss and blockage generation. Increasing wall roughness will shift the pressure rise characteristic to both a lower mass flow rate (with decreased flow range) and lower pressure rise. Currently, the roughness is converted from arithmetic roughness (physical) to sandgrain roughness (model) through a coefficient from Koch and Smith [38]. This coefficient is partially based on sandpaper testing and many considerations were made to apply it to compressor blades. There is a wide range of coefficients that can be used to convert from arithmetic roughness to sandgrain roughness, but based on application, this one from Koch and Smith is the most suitable. However, this coefficient is not exact, e.g. there may be differences due to variations in surface finish (surface finish on composite stator and titanium rotor will be different). Hence, it may be beneficial to deviate slightly from the value of 8.9 for the roughness conversion coefficient if it would help the model match the experiment better. It is important to check the hydraulic smoothness of surfaces before modelling a wall as rough.

4. UNSTEADY SIMULATION DEVELOPMENT AND RESULTS

The flow inside a fan is inherently unsteady, and while steady simulations are able to resolve many of the flow features, it is necessary to understand where unsteady effects may become important.

4.1 Set Up

The current model considered is part-annulus and uses a time transformation interface between the rotor and stator interfaces. The number of passages and types of interfaces used between each domain is listed in Table 4.1 and 4.2 below.

Table 4.1 Domain passages of unsteady part-annulus model.

Domain	Total circumferential extent of model	Number of passages used in model	Number of passages in full annulus
Inlet	90°	1	4
Rotor	81.818181°	5	22
Stator	81.509433°	12	53
Bypass and core	45°	1	8

Table 4.2 Interfaces used in unsteady part-annulus model.

Interface location	Type of interface used
Inlet to rotor	Mixing plane
Rotor to stator	Time-transformation
Stator to bypass and core	Mixing plane

The time-transformation interface is briefly described in Chapter 2; this interface requires a pitch ratio close to 1 to give decent results, which is satisfied here as the pitch ratio between the rotor and stator domains is 1.004. Although this model still relies on mixing planes in front of the rotor and behind the stator, the unsteady rotor-stator interactions will still be captured.

The chosen temporal discretization is 50 timesteps per rotor blade passing. A Richardson Extrapolation in time was not completed here due to transient simulations taking a very long time to reach unsteady periodic convergence. However, this temporal resolution is expected to be sufficient to capture shock oscillations.

Due to computational cost, the coarse mesh with the SST (with curvature correction) turbulence model is used for this simulation. From the previous analysis in Chapter 3, some effects of the reduction in mesh refinement and reduction in turbulence model complexity on the flow solution have been considered; both the coarse mesh and SST turbulence model can capture the flow features qualitatively. This simulation was 30.6 million elements and ran for 10 revolutions. A converged steady state solution on the same mesh was used to initialize the unsteady run.

4.2 Unsteady Periodic Convergence Criteria

The convergence of a transient simulation with an unsteady flow field is more complicated to recognize than that of a steady simulation. At a set operation point, the flow field through the fan is expected to have periodic features; by monitoring properties of the flow through the time-accurate simulation and observing the periodicity and overlap of these monitor signals, unsteady periodic convergence may be qualitatively assessed. However, having a quantifiable measure of unsteady convergence is important – relying on qualitative observations may result in excessive extension of the run past convergence to assure convergence, or it may result in the final solution not having reached actual acceptable convergence, since qualitative assessments are experience based.

Clark and Groover [44] proposed a robust method to quantify unsteady periodic convergence. The method is based on signal processing and processes a monitored flow property at a location of interest using time-mean quantities, phase and magnitudes from DFT, cross correlation for checking signal shape, and integrated signal power to check power distribution. The method is as follows [44]:

1) Select a location of interest and a flow property to monitor throughout the transient simulation.
2) Define the expected periodicity; in the case of turbomachinery, this would likely be the blade passing period or a revolution.
3) For each period, find the time mean of the flow property for each period, and apply DFT to the fluctuating component of the flow property. Using pressure (P) as an example, equation 4.1 gives the mean over a single period, and equation 4.2 gives the DFT of the fluctuating pressure (P') found at an integer multiple (k+1) of the sampling frequency:

$$P_{mean} = \frac{1}{N}\sum_{n=0}^{N-1} P(n+1) \tag{4.1}$$

$$P_{DFT}(k+1) = \sum_{n=0}^{N-1} P'(n+1) e^{-i\left(\frac{2\pi k n}{N}\right)} \tag{4.2}$$

4) Find the PSD of the signal.
5) Find the cross-correlation coefficient at lag L = 0, from equation 4.3:

$$CCF(L) = \frac{\frac{1}{N}\sum_{n=0}^{N-1} P'\big((n+1)+L\big)P'((n+1)+N)}{\frac{1}{N}\left[\sum_{n=0}^{N-1} P'^{2}(n+1)P'^{2}\big((n+1)+N\big)\right]^{1/2}} \tag{4.3}$$

From the above calculations, the convergence of the selected signal can be assessed for several properties. The level of convergence can be defined as a fuzzy set, where 0 indicates not converged and 1 indicates complete convergence. For a comparison between two periods indicated by subscripts 1 and 2:

1) The mean level of the signal can be assessed for convergence:

$$f_M = 1 - \left|1 - \frac{P_{2,mean}}{P_{1,mean}}\right| \tag{4.4}$$

2) The cross-correlation at zero lag can be calculated to compare the shape of the signal from period to period. If the simulation is completely converged, the signals will have the same shape, and this value would be equal to 1:

$$f_S = |CCF(0)| \tag{4.5}$$

3) Important frequencies that are expected to carry most of the power of the signal can be selected a priori. The PSD of these frequencies can be summed to see if power is distributed as expected, or if there is inherent unsteadiness in the flow:

$$f_P = \frac{\sum_{k_{expected}} PSD(k+1)}{\sum_{k=0}^{N-1} PSD(k+1)} \tag{4.6}$$

4) Using the magnitude and phase from the DFT, the convergence of the amplitude (A) and phase (ϕ) of the frequencies of interest may also be assessed:

$$f_A = 1 - \left|1 - \frac{A_2}{A_1}\right| \tag{4.7}$$

$$f_\phi = 1 - \left|\frac{\phi_2 - \phi_1}{\pi}\right| \tag{4.8}$$

The overall level of convergence may then be found also as a fuzzy set:

$$f_c = f_M \cap f_A \cap f_\phi \cap f_S \cap f_P = \min\left(f_M, f_A, f_\phi, f_S, f_P\right) \tag{4.9}$$

Note that the location of interest chosen to assess convergence is dependent upon the purpose of the simulation, and flow properties may have different convergence rates due to the

propagation rate of finite pressure waves and viscous disturbances being different [44]. For this simulation, the pressure and total pressure behind the rotor and stator were used to assess convergence. Figure 4.1 shows an example of fuzzy convergence of the individual signal properties for a pressure signal at the stator leading edge, near the shroud. The dominant frequencies of unsteadiness corresponded to the first and second harmonics of the rotor blade passing frequency. Curiously, for this signal, as well as most of the other ones checked behind the rotor or the stator, it seems that the overall convergence of the signal is limited by the convergence of the CCL.

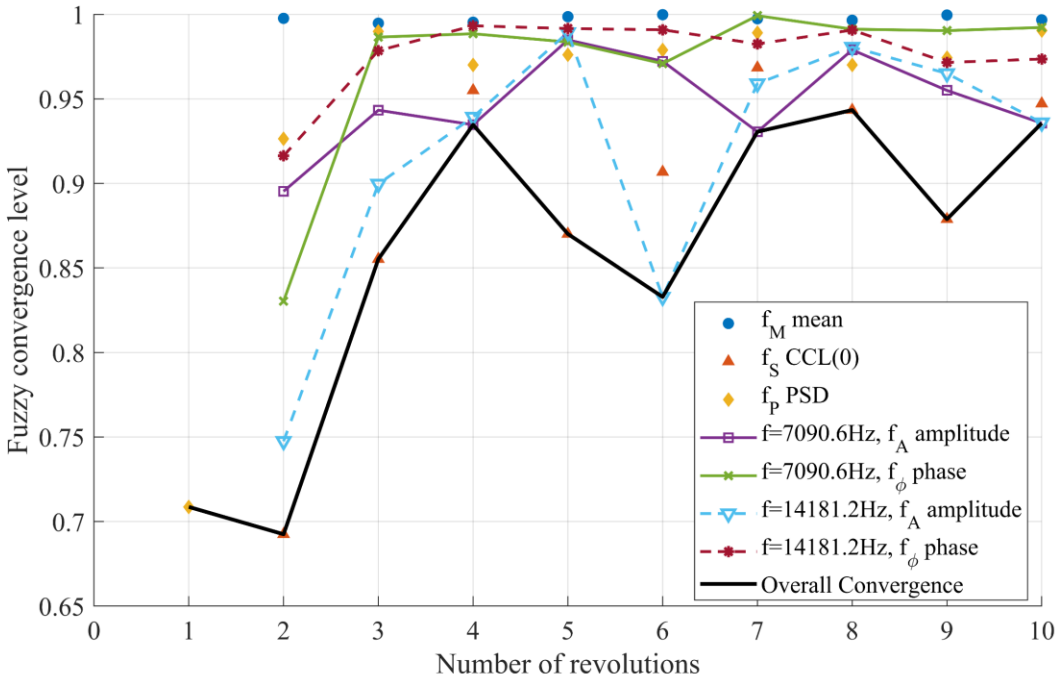

Figure 4.1 Fuzzy convergence of pressure at the stator leading edge, near the shroud; individual signal properties overall convergence.

The overall fuzzy convergence level was checked at several points behind the rotor and the stator; the overall convergence for pressure and total pressure at a point behind the rotor and a point behind the stator is shown as an example in Figure 4.2. Generally, if a convergence level of around 0.8 for pressure and total pressure is considered adequate, then data past the fifth revolution

may be used; if higher levels of convergence are desired (i.e. above 0.9), then 10 revolutions or more may be necessary.

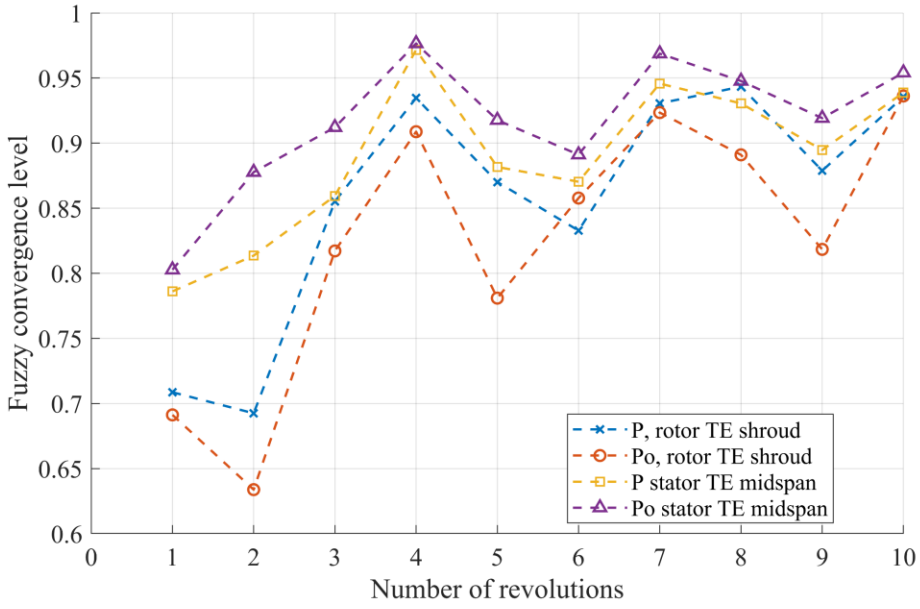

Figure 4.2 Overall fuzzy convergence of pressure and total pressure at two locations.

4.3 Oscillations

To observe the unsteadiness in the flow, the mean and RMS of the pressure at the rotor shroud over the last revolution of the unsteady run is shown in Figure 4.3. The peak unsteadiness of the flow field occurs at the shock location, with a maximum RMS of about 16 Pa near the rotor leading edge. There is a small region of unsteadiness that corresponds to the location of the tip leakage vortex, but the RMS of this region is very small. There is also a large region of unsteadiness behind the shock, likely due to casing boundary layer separation from the shock, with minor contributions from the shock-vortex interaction, since the unsteadiness behind the shock does not follow the trajectory of the shock-vortex interaction (which is shown in a later section).

The unsteadiness of the shock and the tip leakage vortex near this condition is very small near peak efficiency. The oscillation of the shock location may be observed through looking at the chordwise velocity distributions, however, the oscillation of shock impingement location on the suction surface is very small at all spans (for example, under 1% at 80% span). DFTs were applied

to the rotor shroud shock region to observe the oscillation of the pressure; unfortunately, a dominant frequency corresponding to the oscillation of the shock was unclear. Since the shock oscillation amplitude is small, the difference in shock loss between a steady and unsteady shock will be small. This may be a reasonable result near peak efficiency, as unsteadiness may be minor when the shock is confined to the blade passage [12]. This unsteadiness is expected to be large for near stall operation, when the shock is unstarted.

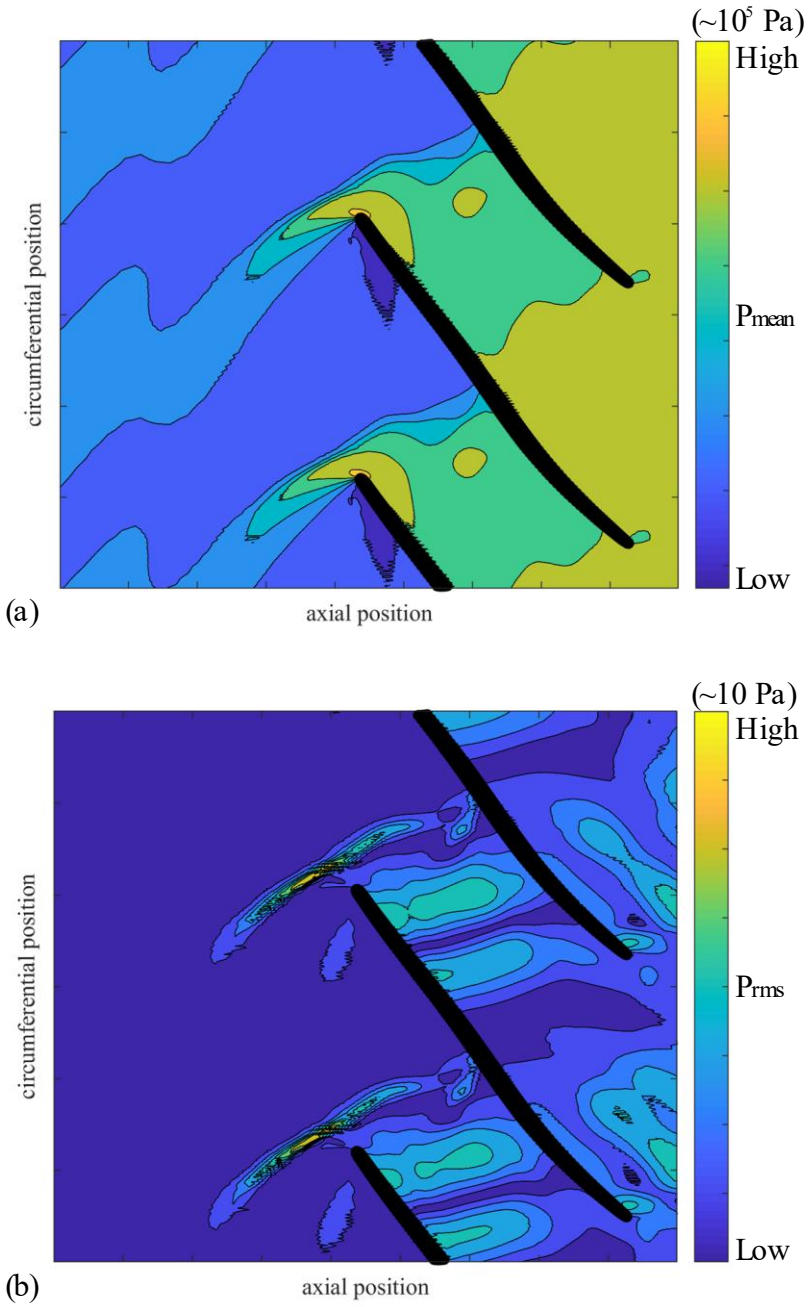

Figure 4.3 Pressure at the rotor shroud, from last revolution of unsteady simulation. (a) Mean component of pressure is in the order of 1 bar; (b) RMS component of pressure is in the order of 10 Pa.

4.4 Comparison with Steady Simulation

A comparison is made between the time-averaged results of last period of the unsteady run, and the converged steady solution on the same mesh. In contrast to the comparisons made in Chapter 3, the two solutions compared here have the same boundary conditions.

Table 4.3 gives a comparison of the overall performance parameters to the steady results. The inlet corrected mass flow rate is the same, and bypass overall performance properties are similar between steady and unsteady runs; however, the core performance drops noticeably when unsteadiness of the flow is included. This is due to the extent of horseshoe vortex at the hub not being captured in the steady simulation (discussed later).

Table 4.3 Comparison of overall performance between time-averaged unsteady results and steady results, normalized by steady results.

Overall performance	Steady	Time-averaged unsteady
Bypass TPR	1	1.000
Core TPR	1	0.978
Bypass efficiency	1	0.995
Core efficiency	1	0.965
Bypass ratio	1	0.998
Inlet corrected mass flow	1	1.000

4.4.1 Stator Leading Edge Profiles

The following comparisons between steady and unsteady solutions will be made with the unsteady solution at an instantaneous point in time. The previous comparisons of oscillation show that the position of the shock and tip leakage vortex near the rotor tip does not change very much; additionally, the variation of local profiles have been compared for a continuous blade passing, and the differences are small enough that using an instantaneous point will still yield a valid qualitative comparison. Figure 4.4 and Figure 4.5 show the total pressure ratio and total temperature ratio profiles at the stator leading edge for the steady run and an instantaneous step in time. Overall, the profiles are similar at midspan; but there is an overprediction of work and efficiency at the hub for the steady case, and a difference in prediction of loss at the tip region. Part of this difference may be attributed to the additional mixing introduced by the mixing plane between the rotor and the stator in the steady case; although the mixing plane conserves momentum, energy, and mass, the entropy will increase similar to a real mixing process [28]. The

differences in tip loss prediction may be particularly affected by this mixing due to distinct flow features being smeared. There is also a difference in shock location that affects this prediction (discussed later). The difference at the hub in both loss and work is significant enough to suggest that there may be different flow structures or significant amounts of vortex shedding in the unsteady case. To attempt to observe this difference, the limiting streamlines on the blade suction surface were investigated for the steady and unsteady cases in Figure 4.6.

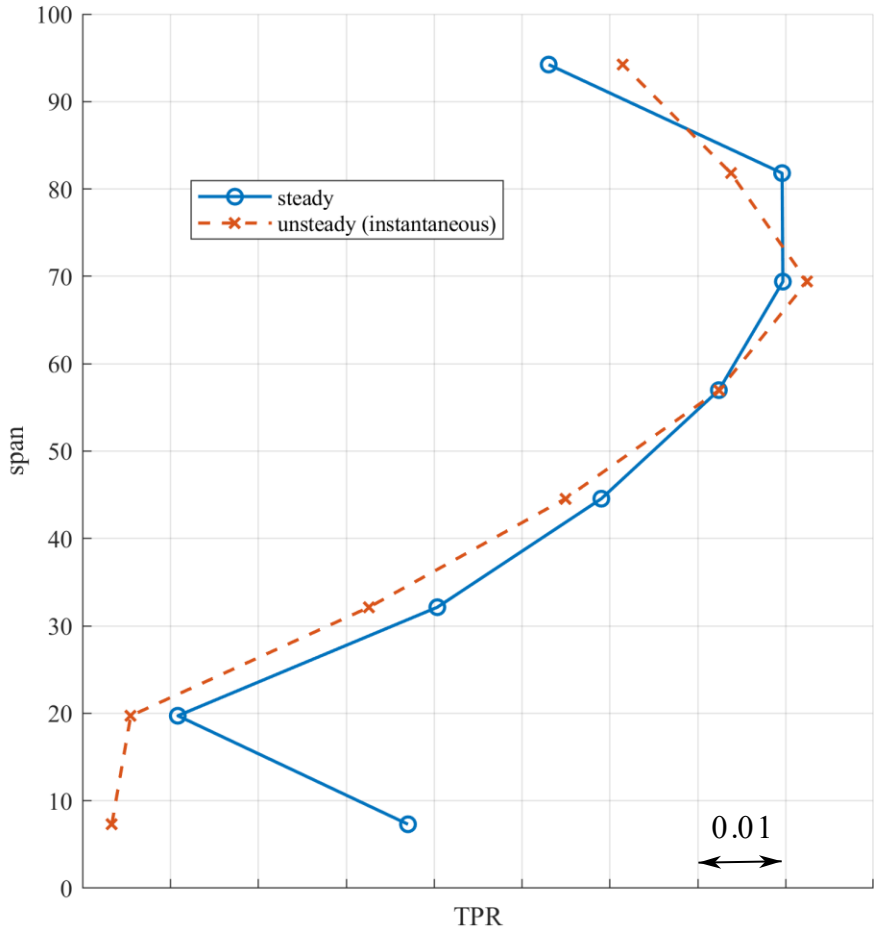

Figure 4.4 Total pressure ratio at leading edge of stator; steady comparison with unsteady instance in time.

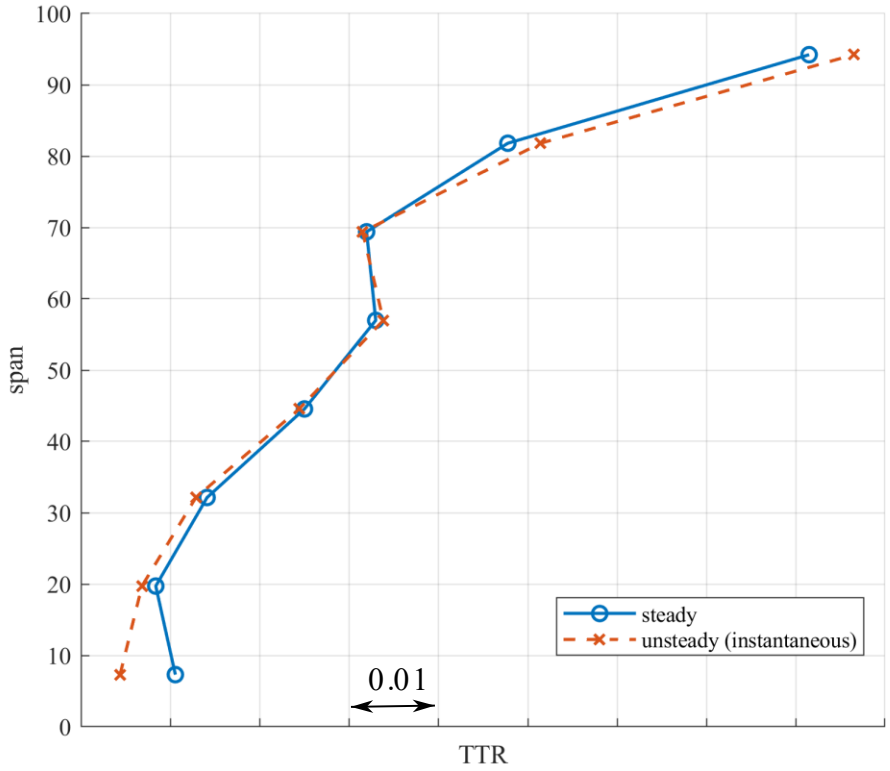

Figure 4.5 Total temperature ratio at leading edge of stator (rake location); steady comparison with unsteady instance in time.

The limiting streamlines in Figure 4.6 show that the separation caused by the horseshoe vortex at the hub is further down the flow path with a larger radial extent in the unsteady case. In combination with unsteady vortex shedding in this region, this likely accounts for the difference in predictions of work and loss at the hub. Note that the earlier separation caused by the horseshoe vortex in the steady case has forced the flow exiting the rotor to be more radial.

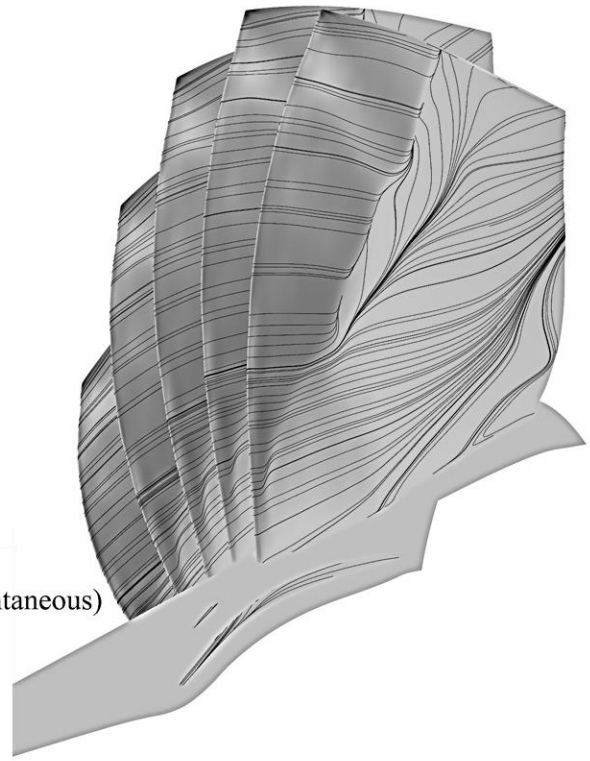

(a) Unsteady (instantaneous)

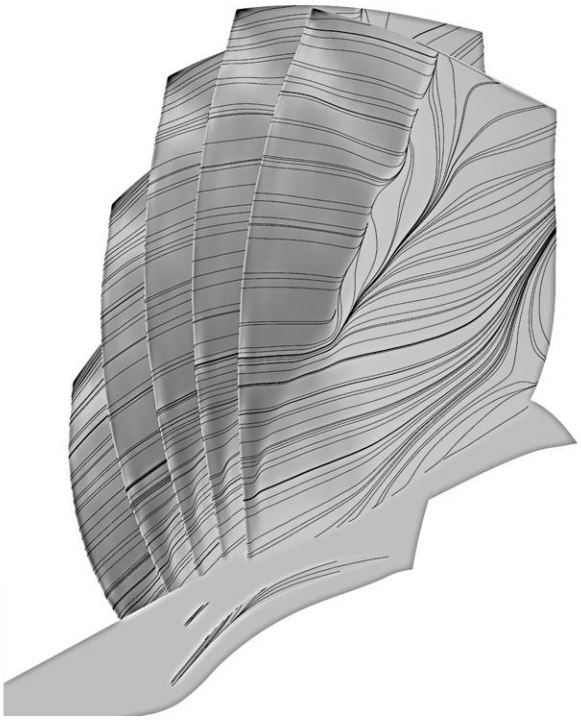

(b) Steady

Figure 4.6 Comparison between steady and unsteady limiting streamlines.

4.4.2 Shock Location

A notable difference between the steady and unsteady simulation is that the unsteady simulation predicts the passage shock to occur earlier than the steady simulation; at 90% span, this is a difference of about 1.5% rotor chords upstream. In Figure 4.7, the unsteady shock location has been plotted for one instance in time (the oscillation in shock location is very small so this is representative of the difference between the steady and unsteady simulations). The shock in the unsteady simulation is slightly stronger than that of the steady simulation; this may account for some of the difference in the total pressure prediction near the tip.

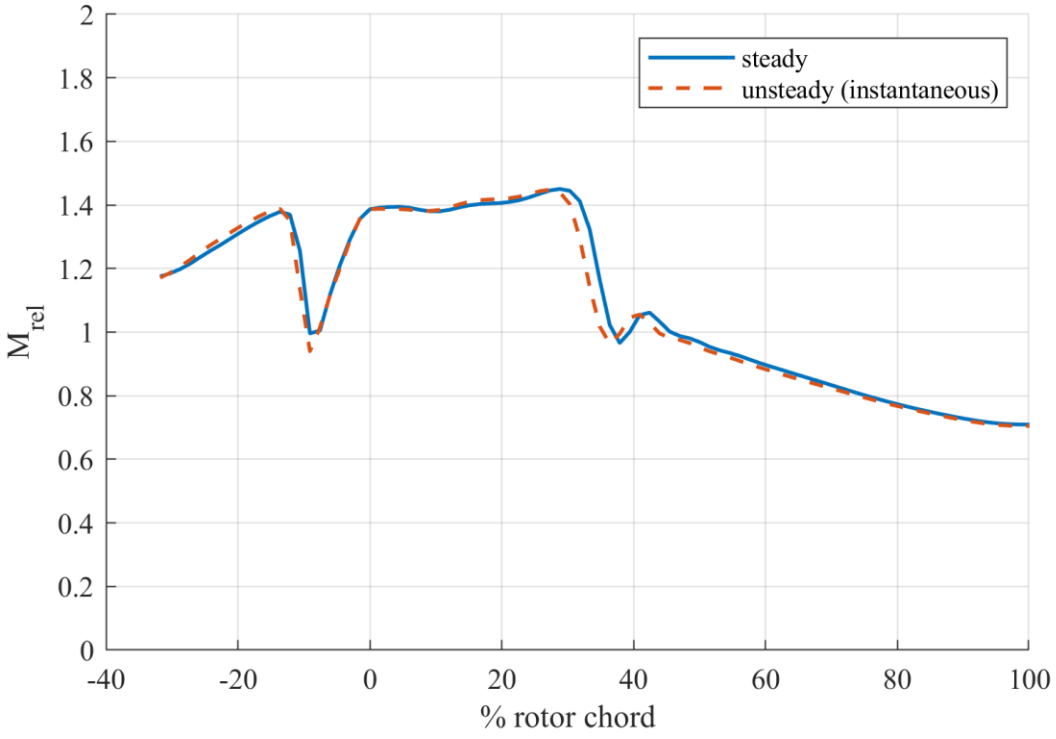

Figure 4.7 Relative Mach number comparison at 20% pitch and 90% span; comparison between steady and unsteady simulations.

4.4.3 Shock-Vortex Interaction Region

The location of the lower momentum region near the casing behind the shock and vortex interaction is circled in black in Figure 4.8. There is not much difference in the interaction location

here, although the contour of axial velocity shows a slightly greater decrease in velocity in this region for the unsteady case. Note that although the shock in the unsteady case stands slightly more forward than the steady case, the difference is hardly noticeable.

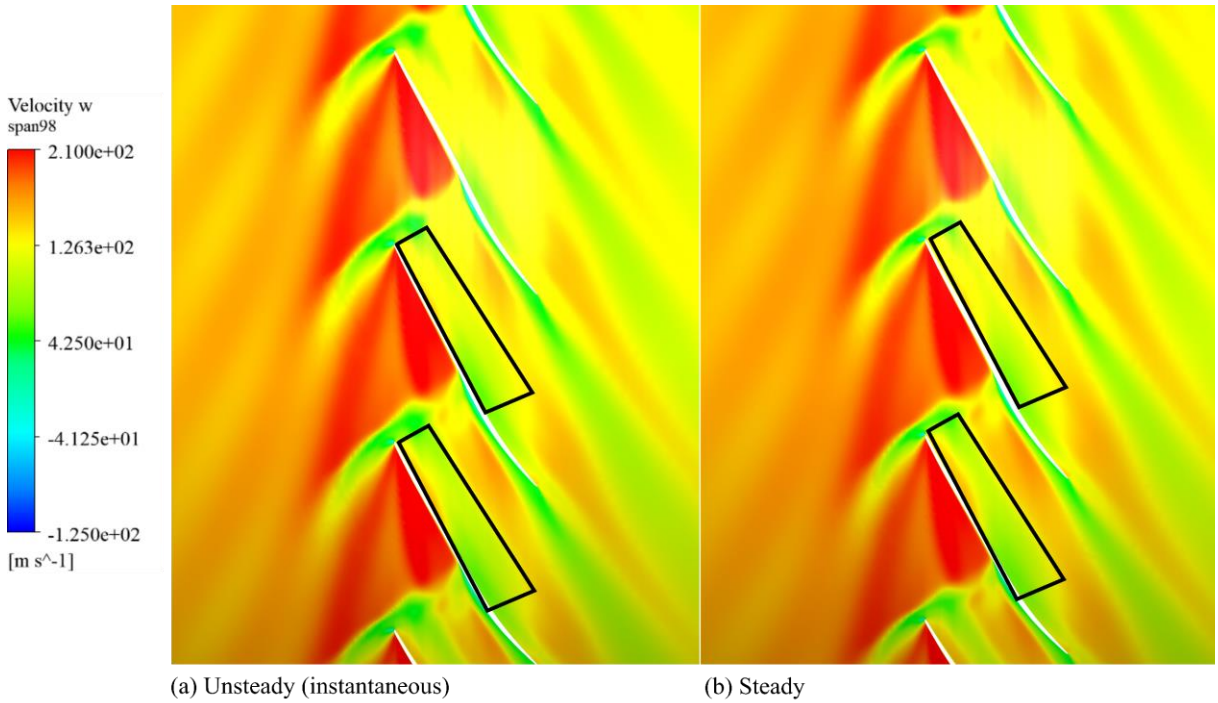

(a) Unsteady (instantaneous) (b) Steady

Figure 4.8 Axial velocity at 98% span; comparison between steady and unsteady simulations.

4.4.4 Blockage

Since blockage in the rotor passage is an important measure of proximity to stall, comparisons between the blockage in the steady and unsteady cases were made through the entire rotor passage. The spanwise blockage is calculated with Suder's method [30], described in Chapter 1. Although the blockage near the tip does not always agree between the different cases, they are very close. An example is shown at 10% and 90% chordwise locations in Figure 4.9. Note that the blockage at the hub at 10% chord mostly appears high because this method for assessing blockage is based on radial and circumferential gradients of the axial component of velocity, and at the rotor inlet, the hub curvature accelerates the flow radially.

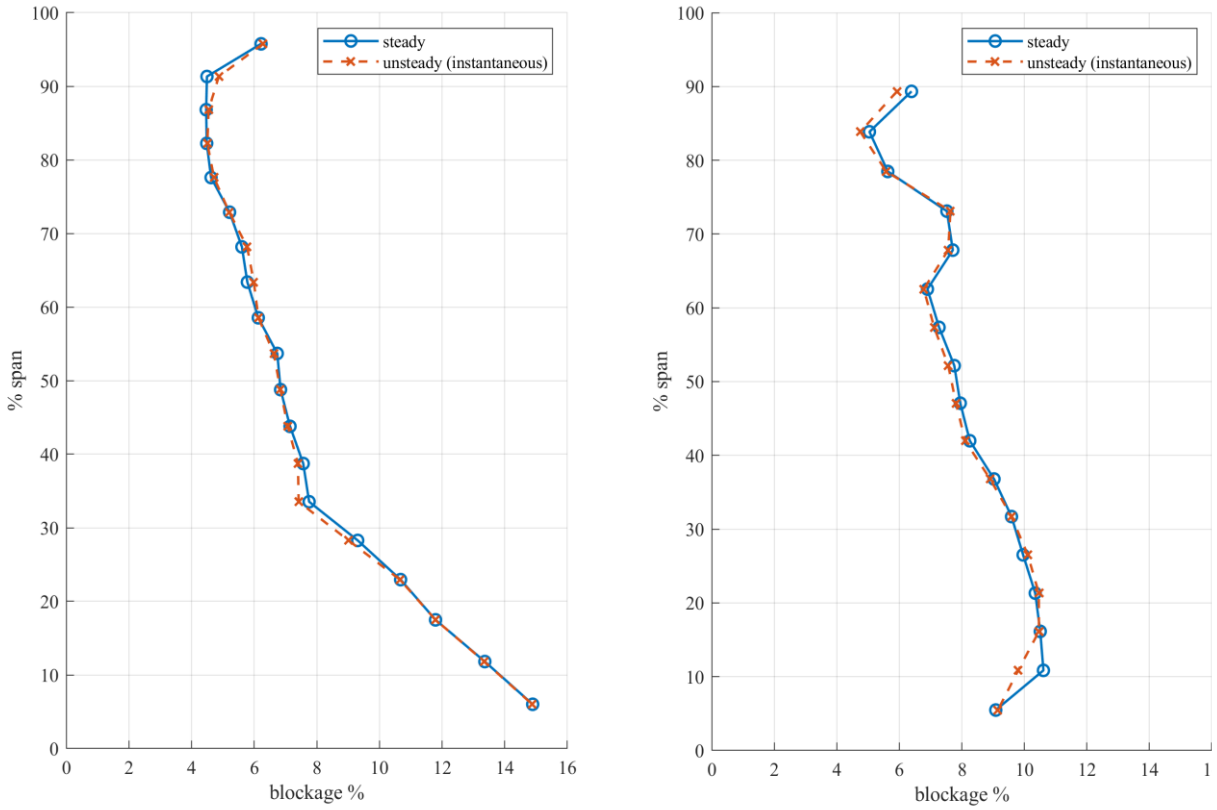

(a) at 10% chord (b) at 90% chord

Figure 4.9 Spanwise distribution of blockage at 10% and 90% chord; comparison between steady and unsteady simulations.

5. CONCLUSIONS

The goal of this research is to use CFD to obtain a better understanding of the flow physics in this transonic fan and to consider the impact of various modelling assumptions and simplifications on the flow field. The current modelling decisions are based on a comparison of simulation solutions; the model can be adjusted to better satisfy realistic results when more information on boundary layer thickness, inlet and outlet flow conditions, work and loss distribution, freestream turbulence levels, etc. is obtained via experiment.

5.1 Current Modelling Decisions

The current conclusions on modelling decisions are:

- To obtain a qualitative resolution of the flow features, a single passage coarse mesh with 8 million elements is sufficient for resolving the passage shock and tip leakage flow. If accuracy on quantitative properties of the flow is important, the medium mesh with 22 million elements should provide a solution with small discretization error.
- The BSL-EARSM turbulence model gives a good balance between computational cost and flow field resolution. The SST model captures flow field features qualitatively, however, there may be error in the prediction of boundary layer separation and strength of the radial flow behind the passage shock.
- To find comparable points between simulations (or experiment), it is suggested that an operation point at a similar category of loading (i.e. peak efficiency) is found on their respective speedlines. The shape of the spanwise work distribution behind the rotor may be a good trend to match for finding a point of comparison.
- For unsteady simulations, iterative convergence at each timestep is an important factor to consider for both computational cost and solution accuracy. The coarse mesh with SST turbulence model is chosen for unsteady runs, due to their advantage in iterative convergence speed.
- The unsteadiness of the flow field should be assessed before assuming a steady simulation to be representative of the physical flow. Near peak efficiency, the unsteadiness of the rotor tip flow field may be small; however, if loading is increased, oscillations in flow feature

locations should be considered. The increased oscillatory behavior of the passage shock, tip leakage vortex trajectory, and the shock-vortex interaction region, will increase loss and will likely cause fluctuations in flow blockage.

5.2 Recommendations for Future Work

Future work on the CFD for this fan consists of testing casing treatment ideas, simulating the instability that leads to stall or surge, and testing the effects of inlet distortion. However, the baseline computational model should first be validated with experimental results. Some further considerations in improving modelling may be:

- The turbulence modelling may be improved by adjusting the turbulence production and dissipation to match mixing of the flow in the rotor wake; this may be verified with a rotor trailing edge traverse.
- The temporal resolution of the unsteady flow field may be assessed with a Richardson Extrapolation in time, if computational resources allow; otherwise, experimentally observed unsteadiness (i.e. with Kulites on the rotor casing) will be able to provide a good indication of the sampling frequency needed to capture relevant oscillations.
- Full annulus unsteady flow should be simulated for comparison with the part-span unsteady model with a time-transformation interface. It is possible that a part-span model does not have enough passages to allow stall cells to develop as they would experimentally.
- If flow through the tip gap is measured, it would be worth calibrating the CFD model to match this flow rate, either through changing the size of the tip clearance or through adding slight rounds to the blade tip edge. The momentum and mass flow through the tip gap is important to the extent and behavior of the tip leakage flow.
- The flow field near the rotor tip at part speed at or near subsonic speeds should be compared to flow features at design speed before designing a casing treatment.
- If a flow visualization technique is used to observe the boundary layer separation on the suction surface, it would be interesting to see the effects of including a calibrated transition model.

REFERENCES

[1] A. J. Wennerstrom, Design of Highly Loaded Axial-Flow Fans and Compressors. 2000.

[2] N. A. Cumpsty, Compressor Aerodynamics. Harlow, Essex, England: Longman Scientific & Technical, 1989.

[3] C. Freeman and N. A. Cumpsty, "Method for the prediction of supersonic compressor blade performance," Journal of Propulsion and Power, vol. 8, no. 1, pp. 199–208, Jan. 1992, doi: 10.2514/3.23461.

[4] Y. Lu, B. Lad, J. Green, S. Stapelfeldt, and M. Vahdati, "Effect of Geometry Variability on Transonic Fan Blade Untwist †," IJTPP, vol. 4, no. 3, p. 24, Aug. 2019, doi: 10.3390/ijtpp4030024.

[5] M. Hoeger, G. Fritsch, and D. Bauer, "Numerical Simulation of the Shock-Tip Leakage Vortex Interaction in a HPC Front Stage," Journal of Turbomachinery, vol. 121, no. 3, pp. 456–468, Jul. 1999, doi: 10.1115/1.2841338.

[6] G. R. Miller, G. W. Lewis Jr, and M. J. Hartmann, "Shock losses in transonic compressor blade rows," Journal of Engineering for Power, vol. 83, no. 3, pp. 235–241, Jul. 1961, doi: 10.1115/1.3673182.

[7] D. C. Prince, "Three-Dimensional Shock Structures for Transonic/Supersonic Compressor Rotors," Journal of Aircraft, vol. 17, no. 1, pp. 28–37, Jan. 1980, doi: 10.2514/3.57871.

[8] A. J. Strazisar, "Investigation of Flow Phenomena in a Transonic Fan Rotor Using Laser Anemometry," Journal of Engineering for Gas Turbines and Power, vol. 107, no. 2, pp. 427–435, Apr. 1985, doi: 10.1115/1.3239743.

[9] A. H. Epstein, J. L. Kerrebrock, and W. T. Thompkins, "Shock Structure in Transonic Compressor Rotors," AIAA Journal, vol. 17, no. 4, pp. 375–379, Apr. 1979, doi: 10.2514/3.61134.

[10] M. D. Hathaway, J. B. Gertz, A. H. Epstein, and A. J. Strazisar, "Rotor wake characteristics of a transonic axial-flow fan," AIAA Journal, vol. 24, no. 11, pp. 1802–1810, Nov. 1986, doi: 10.2514/3.9527.

[11] B. H. K. Lee, "Oscillatory shock motion caused by transonic shock boundary-layer interaction," AIAA Journal, vol. 28, no. 5, pp. 942–944, May 1990, doi: 10.2514/3.25144.

[12] W. W. Copenhaver, S. L. Puterbaugh, and C. Hah, "Unsteady Flow and Shock Motion in a Transonic Compressor Rotor," Journal of Propulsion and Power, vol. 13, no. 1, pp. 17–23, Jan. 1997, doi: 10.2514/2.5145.

[13] W. B. Harvey, D. E. Hobbs, D. Lee, M. C. Williams, and K. F. Williams, “Rotor redesign for a highly loaded 1800 ft/sec tip speed fan. 3: Laser Doppler velocimeter report,” NASA-CR-167954, Apr. 1982. Accessed: Nov. 04, 2021. [Online]. Available: https://ntrs.nasa.gov/citations/19830005857

[14] J. J. Adamczyk, M. L. Celestina, and E. M. Greitzer, “The Role of Tip Clearance in High-Speed Fan Stall,” Journal of Turbomachinery, vol. 115, no. 1, pp. 28–38, Jan. 1993, doi: 10.1115/1.2929212.

[15] J. Schmücker and A. Schäffler, “Performance deterioration of axial compressors due to blade defects,” in AGARD CONFERENCE PROCEEDINGS AGARD CP, 1994, pp. 16–16.

[16] W. W. Copenhaver, E. R. Mayhew, C. Hah, and A. R. Wadia, “The Effect of Tip Clearance on a Swept Transonic Compressor Rotor,” Journal of Turbomachinery, vol. 118, no. 2, pp. 230–239, Apr. 1996, doi: 10.1115/1.2836630.

[17] J. A. Storer and N. A. Cumpsty, “Tip Leakage Flow in Axial Compressors,” Journal of Turbomachinery, vol. 113, no. 2, pp. 252–259, Apr. 1991, doi: 10.1115/1.2929095.

[18] M. Hewkin-Smith, G. Pullan, S. D. Grimshaw, E. M. Greitzer, and Z. S. Spakovszky, “The Role of Tip Leakage Flow in Spike-Type Rotating Stall Inception,” Journal of Turbomachinery, vol. 141, no. 6, p. 10, Jun. 2019, doi: 10.1115/1.4042250.

[19] R. V. Chima, “Calculation of Tip Clearance Effects in a Transonic Compressor Rotor,” Journal of Turbomachinery, vol. 120, no. 1, pp. 131–140, Jan. 1998, doi: 10.1115/1.2841374.

[20] G. T. Chen, E. M. Greitzer, C. S. Tan, and F. E. Marble, “Similarity Analysis of Compressor Tip Clearance Flow Structure,” Journal of Turbomachinery, vol. 113, no. 2, pp. 260–269, Apr. 1991, doi: 10.1115/1.2929098.

[21] K. L. Suder and M. L. Celestina, “Experimental and Computational Investigation of the Tip Clearance Flow in a Transonic Axial Compressor Rotor,” Journal of Turbomachinery, vol. 118, no. 2, pp. 218–229, Apr. 1996, doi: 10.1115/1.2836629.

[22] M. Inoue and M. Kuroumaru, “Structure of Tip Clearance Flow in an Isolated Axial Compressor Rotor,” Journal of Turbomachinery, vol. 111, no. 3, pp. 250–256, Jul. 1989, doi: 10.1115/1.3262263.

[23] D. A. Rains, “Tip clearance flows in axial flow compressors and pumps,” CALIFORNIA INST OF TECH PASADENA MECHANICAL ENGINEERING LAB, 1954.

[24] C. Hah, D. C. Rabe, and A. R. Wadia, “Role of Tip-Leakage Vortices and Passage Shock in Stall Inception in a Swept Transonic Compressor Rotor,” in Volume 5: Turbo Expo 2004, Parts A and B, Vienna, Austria, Jan. 2004, pp. 545–555. doi: 10.1115/GT2004-53867.

[25] M. Furukawa, M. Inoue, K. Saiki, and K. Yamada, “The Role of Tip Leakage Vortex Breakdown in Compressor Rotor Aerodynamics,” Journal of Turbomachinery, vol. 121, no. 3, pp. 469–480, Jul. 1999, doi: 10.1115/1.2841339.

[26] O. Thomer, E. Krause, and W. Schröder, “Interaction between Longitudinal Vortices and Normal and Oblique Shocks,” in Vortex Dominated Flows, WORLD SCIENTIFIC, 2005, pp. 199–227. doi: 10.1142/9789812703439_0012.

[27] W. J. Calvert and R. B. Ginder, “Transonic fan and compressor design,” Proceedings of the Institution of Mechanical Engineers, Part C: Journal of Mechanical Engineering Science, vol. 213, no. 5, pp. 419–436, May 1999, doi: 10.1243/0954406991522671.

[28] J. D. Denton, “Some Limitations of Turbomachinery CFD,” in Volume 7: Turbomachinery, Parts A, B, and C, Glasgow, UK, Oct. 2010, pp. 735–745. doi: 10.1115/GT2010-22540.

[29] R. E. Mayle, “The Role of Laminar-Turbulent Transition in Gas Turbine Engines,” in Volume 5: Manufacturing Materials and Metallurgy; Ceramics; Structures and Dynamics; Controls, Diagnostics and Instrumentation; Education; IGTI Scholar Award; General, Orlando, Florida, USA, Jun. 1991, p. V005T17A001. doi: 10.1115/91-GT-261.

[30] K. L. Suder, “Blockage development in a transonic, axial compressor rotor,” Journal of Turbomachinery, vol. 120, no. 3, pp. 465–476, Jul. 1998, doi: 10.1115/1.2841741.

[31] J. Dunham, Ed., CFD validation for propulsion system components. Neuilly-sur-Seine, France: AGARD, 1998.

[32] M. J. Wilson, M. Imregun, and A. I. Sayma, “The Effect of Stagger Variability in Gas Turbine Fan Assemblies,” Sep. 2008, pp. 1059–1069. doi: 10.1115/GT2006-90434.

[33] “ANSYS CFX-Solver Theory Guide.” ANSYS, Inc., 2019.

[34] “ANSYS CFX-Solver Modelling Guide.” ANSYS, Inc., 2019.

[35] T. R. Mueller, D. M. Vogt, M. Fischer, and B. A. Phillipsen, “On the far-field boundary condition treatment in the framework of aeromechanical computations using ANSYS CFX,” Proceedings of the Institution of Mechanical Engineers, Part A: Journal of Power and Energy, vol. 235, no. 5, pp. 1103–1118, Aug. 2021, doi: 10.1177/0957650920962698.

[36] S. B. Pope, Turbulent flows. Cambridge university press, 2000.

[37] A. Shabbir and M. G. Turner, “A Wall Function for Calculating the Skin Friction With Surface Roughness,” in Volume 5: Turbo Expo 2004, Parts A and B, Vienna, Austria, Jan. 2004, pp. 1661–1671. doi: 10.1115/GT2004-53908.

[38] C. C. Koch and L. H. Smith, “Loss Sources and Magnitudes in Axial-Flow Compressors,” Journal of Engineering for Power, vol. 98, no. 3, pp. 411–424, Jul. 1976, doi: 10.1115/1.3446202.

[39] J. D. Denton, “The Calculation of Three-Dimensional Viscous Flow Through Multistage Turbomachines,” Journal of Turbomachinery, vol. 114, no. 1, pp. 18–26, Jan. 1992, doi: 10.1115/1.2927983.

[40] F. R. Menter, “Two-equation eddy-viscosity turbulence models for engineering applications,” AIAA Journal, vol. 32, no. 8, pp. 1598–1605, Aug. 1994, doi: 10.2514/3.12149.

[41] P. R. Spalart and M. Shur, “On the sensitization of turbulence models to rotation and curvature,” Aerospace Science and Technology, vol. 1, no. 5, pp. 297–302, Jul. 1997, doi: 10.1016/S1270-9638(97)90051-1.

[42] P. J. Roache, “QUANTIFICATION OF UNCERTAINTY IN COMPUTATIONAL FLUID DYNAMICS,” Annu. Rev. Fluid Mech., vol. 29, no. 1, pp. 123–160, Jan. 1997, doi: 10.1146/annurev.fluid.29.1.123.

[43] I. B. Celik, U. Ghea, P. J. Roache, C. J. Freitas, H. Coleman, and P. E. Raad, “Procedure for Estimation and Reporting of Uncertainty Due to Discretization in CFD Applications,” Journal of Fluids Engineering, vol. 130, no. 078001, Jul. 2008, doi: 10.1115/1.2960953.

[44] J. P. Clark and E. A. Grover, “Assessing Convergence in Predictions of Periodic-Unsteady Flowfields,” Journal of Turbomachinery, vol. 129, no. 4, pp. 740–749, Aug. 2006, doi: 10.1115/1.2720504.

[45] N. A. Cumpsty and J. H. Horlock, “Averaging Nonuniform Flow for a Purpose,” Journal of Turbomachinery, vol. 128, no. 1, pp. 120–129, Feb. 2005, doi: 10.1115/1.2098807.

[46] J. D. Denton, “Lessons from rotor 37,” J. of Therm. Sci., vol. 6, no. 1, pp. 1–13, Mar. 1997, doi: 10.1007/s11630-997-0010-9.

[47] M. Furukawa, K. Saiki, K. Nagayoshi, M. Kuroumaru, and M. Inoue, “Effects of Stream Surface Inclination on Tip Leakage Flow Fields in Compressor Rotors,” Journal of Turbomachinery, vol. 120, no. 4, pp. 683–692, Oct. 1998, doi: 10.1115/1.2841777.

[48] M. Vahdati, A. I. Sayma, C. Freeman, and M. Imregun, “On the Use of Atmospheric Boundary Conditions for Axial-Flow Compressor Stall Simulations,” Journal of Turbomachinery, vol. 127, no. 2, pp. 349–351, Apr. 2005, doi: 10.1115/1.1861912.

[49] K. L. Suder, R. V. Chima, A. J. Strazisar, and W. B. Roberts, “The Effect of Adding Roughness and Thickness to a Transonic Axial Compressor Rotor,” Journal of Turbomachinery, vol. 117, no. 4, pp. 491–505, Oct. 1995, doi: 10.1115/1.2836561.

[50] I. E. Alber, J. W. Bacon, B. S. Masson, and D. J. Collins, “An Experimental Investigation of Turbulent Transonic Viscous-Inviscid Interactions,” AIAA Journal, vol. 11, no. 5, pp. 620–627, May 1973, doi: 10.2514/3.50501.